# Measurement of Longitudinal Single Spin Asymmetry in the Production of Muons from W/Z Boson Decays in Polarized p+p Collisions at $\sqrt{s} = 510$ GeV with the PHENIX Detector at RHIC

BY

ABRAHAM MELES, B.Sc., M.Sc.

A dissertation submitted to the Graduate School

in partial fulfillment of the requirements

for the degree

Doctor of Philosophy

Major Subject: Physics

New Mexico State University

Las Cruces New Mexico

May 2015

"Measurement of Longitudinal Single Spin Asymmetry in the Production of Muons from W/Z Boson Decays in Polarized p+p Collisions at $\sqrt{s} = 510$ GeV with the PHENIX Detector at RHIC" a dissertation prepared by Abraham Meles in partial fulfillment of the requirements for the degree, Doctor of Philosophy, has been approved and accepted by the following:

---

Loui Reyes
Interim Dean of the Graduate School

---

Xiaorong Wang
Chair of the Examining Committee

---

Date

Committee in charge:

Dr. Xiaorong Wang, Chair

Dr. Stephen Pate

Dr. Matthias Burkardt

Dr. Graciela Unguez

# DEDICATION

I dedicate this work to my father Gidey Meles who couldn't have access to elementary school in his childhood, but did all he can do to maintain the best education for me.

ACKNOWLEDGMENTS

I would like to express my special appreciation and thanks to my advisor, Dr. Xiaorong Wang and our beloved NMSU Experimental Nuclear Physics Group leader Dr. Stephen Pate, for your encouragement, guidance, and patience. Your advice and funding to my research as well as the support you provided me to travel, learn and present my works at several conferences have been priceless. I would also like to thank my committee members, Dr. Xiaorong Wang, Dr. Stephen Pate, Dr. Matthias Burkardt, Dr. Graciela Unguez for serving as my committee members even at hardship.

A special thanks to my family and my wife Muna Yohanes. Words cannot express how grateful I am to my mother Almaz Tewolde and father Gidey Meles for all of the sacrifices that you have made on my behalf. Your prayer for me was what sustained me thus far.

# ABSTRACT

Measurement of Longitudinal Single Spin Asymmetry in the Production of Muons from W/Z Boson Decays in Polarized p+p Collisions at $\sqrt{s} = 510$ GeV with the PHENIX Detector at RHIC

BY

ABRAHAM MELES, B.Sc., M.Sc.

New Mexico State University

Las Cruces, New Mexico, 2015

Dr. Xiaorong Wang, Chair

The contribution from the sea quarks to the proton spin have been poorly constrained mainly because of the limited knowledge we have on the fragmentation function in polarized Semi Inclusive Deep Inelastic Scattering (SIDIS) experments. The parity-violating longitudinal single spin asymmetry $A_L$ in the production of $W$ bosons in $p + p$ collisions does not involve fragmentation function and is an alternative better way of exploring the polarization of sea quarks in the proton. The measurment will be useful especially in constraining $\bar{u}$ and $\bar{d}$ in the very backward and forward rapidities respectively. However, identifying the muons

from the decay of the $W$ is challenging due to a great background of hadronic in flight decays and other muon producing processes such as heavy flavor decays. In the forward and backward hemispheres of PHENIX at RHIC, the muon spectrometers have been recently upgraded in order to provide additional trigger and tracking information to suppress those backgrounds. One of those upgrades is the Forward Vertex (FVTX) detector, a silicon-strip tracker. In 2013, PHENIX accumulated the largest amount of polarized $p+p$ collision data ever collected in the world ($\sim 240 pb^{-1}$) at $\sqrt{s} = 510$ GeV with a beam polarization of 56%. The analysis techniques used to extract the signal from the data and the longitudinal single spin asymmetries $A_L$ in RHIC 2013 run will be discussed.

## CONTENTS


LIST OF TABLES . . . . . xi

LIST OF FIGURES . . . . . xvi

1 Introduction . . . . . 1

2 Physics Background . . . . . 8

2.1 Parton model . . . . . 8

2.2 Spin structure of the nucleon . . . . . 16

2.2.1 Polarized DIS . . . . . 16

2.2.2 Experiments in determination of polarized quark and anti-quark PDFs . . . . . 21

2.3 $W/Z$ bosons Production and decay from proton-proton collisions . 22

2.3.1 Hadronic production and decays of $W$ bosons . . . . . 27

2.3.2 Hadronic production and decays of $Z$ bosons . . . . . 34

2.4 Probing sea quark polarization via $W/Z$ bosons . . . . . 35

2.4.1 Longitudinal single spin asymmetry $A_L^{\ell\pm}$ . . . . . 35

2.5 $A_L^{\ell\pm}$ at mid and forward rapidities . . . . . 38

2.5.1 Measurement of $W^{\pm}/Z \to \mu^{\pm}$ at forward rapidity . . . . . 41

3 Apparatus and Data Taking . . . . . 46

3.1 Polarized proton at RHIC . . . . . 46

3.1.1 Polarized beam source . . . . . 47
3.1.2 Accelerator complex . . . . . 47
3.1.3 Maintain and measure the polarization at RHIC . . . . . 49
3.2 The PHENIX detector . . . . . 55
3.2.1 PHENIX magnets and hadron absorber . . . . . 59
3.2.2 Global detectors, BBC and ZDC . . . . . 62
3.2.3 Muon Tracker (MuTr)[66] . . . . . 66
3.2.4 Muon Identifier (MuID)[66] . . . . . 67
3.2.5 PHENIX muon arm upgrade . . . . . 71
3.2.6 Resistive Plate Chambers(RPC) . . . . . 75
3.2.7 Forward Vertex Detector (FVTX) . . . . . 76
3.3 Data taking and Triggers . . . . . 82
4 Data Set . . . . . 90
4.1 Overview . . . . . 90
4.2 Luminosity Monitor . . . . . 91
4.3 Beam polarization . . . . . 96
4.4 Types of background . . . . . 100
4.5 Pythia related signal and muonic background simulations . . . . . 104
4.6 Single hadron background simulations . . . . . 107
4.7 Reliability of the simulations and comparison to data . . . . . 109
5 Signal Extraction . . . . . 111

5.1 Kinematic variables and basic selection criteria . . . . . 113
5.2 W likelihood ratio extraction and background estimation . . . . . 116
5.3 W likelihood ratio of valid FVTX events . . . . . 125
5.4 Signal to background ratio extraction . . . . . 132
5.5 Fit consistency check . . . . . 143
5.6 Possible future improvements of the hadronic distribution in signal region . . . . . 145
6 Measurement of Longitudinal Single Spin Asymmetry of $W^{\pm}/Z \to \mu^{\pm}$ 148
6.1 Asymmetry calculation . . . . . 148
6.2 Crossing information and spin patterns . . . . . 150
6.3 Results and discussions . . . . . 152
6.3.1 Signal to Background ratio results with uncertainity . . . . 152
6.3.2 Final longitudinal single spin asymmetry results . . . . . 153
6.4 Future prospects . . . . . 162
REFERENCES . . . . . 166

## LIST OF TABLES


3.1 The key parameters of the PHENIX Central Magnet and the Muon Magnets. . . . . 60

3.2 Parameters of hadron absorbers in the PHENIX detector. . . . . 62

3.3 Key parameters related to the three stations of the MuTr. . . . . 70

3.4 Key parameters of MuID. . . . . 72

3.5 Summary of FVTX design parameters. . . . . 79

3.6 Muon triggers employed in RHIC run 2013 . . . . . 89

4.1 Spin patterns in RHIC run 2013 . . . . . 99

4.2 Spin patterns in RHIC run 2013 . . . . . 100

4.3 Reference runs selected for simulations . . . . . 105

4.4 Simulated sub-processes in Run 2013 . . . . . 106

4.5 Single hadron simulated events and weights . . . . . 108

5.1 Definition of the MuTr and MuID related kinematic variables. . . 114

5.2 Definition of the RPC and FVTX related kinematic variables. . . 115

5.3 Muon background scaling factors used in the analysis . . . . . 136

5.4 The fit results with $n_{sig}$, $n_{\mu}$, $n_{had}$, and the signal over background ratio in the three $\eta$ bins. . . . . 147

6.1 Signal to Background results including uncertainties from various contributions . . . . . 154

6.2 The final longitudinal single spin asymmetries $A_L$ for the whole $\eta$ range. . . . . 156

6.3 The final longitudinal single spin asymmetries $A_L$ in the $1.1 < \eta <$ 1.4 range. . . . . 159

6.4 The final longitudinal single spin asymmetries $A_L$ in the $1.4 < \eta <$ 1.8 range. . . . . 160

6.5 The final longitudinal single spin asymmetries $A_L$ in the $1.8 < \eta <$ 2.6 range. . . . . 161

## LIST OF FIGURES


1.1 Polarized Parton Distributions. . . . . 5

2.1 Deep inelastic scattering in electron-proton scattering. . . . . 11

2.2 $Q^2$ dependence of $F_2(x, Q^2)$ . . . . . 17

2.3 Summary of various $g_1(x)$ measurements . . . . . 23

2.4 Leptonic decay mode $W^+ \to e^+\nu_e$. . . . . 24

2.5 Hadronic production subprocess of $W^+$. . . . . 28

2.6 Measurements of production cross section of $W^\pm \to \ell^\pm\bar{\nu}$ and $Z \to \ell^+\ell^-$ . . . . . 30

2.7 Helicity conservation in production and decay of $W^\pm$ boson. . . . 32

2.8 The rapidity distribution of the charged lepton from $W$ decays . . 33

2.9 The convention of the coordinate system for spin asymmetry. . . . 36

2.10 Estimation of $A_L$ of $W^\pm \to \ell^\pm\nu_\ell$ at $\sqrt{s} = 500$ GeV with the CHE NLO generator[11]. . . . . 38

2.11 Estimation of $A_L$ of $Z \to \ell^+\ell^-$ at $\sqrt{s} = 500$ GeV with the CHE NLO generator[11]. . . . . 39

2.12 $A_L$ for $e^\pm$ from $W^\pm/Z^0$ boson decays for $|\eta| < 0.35$, $30 < p_T < 50$ GeV/$c$ from PHENIX Run 2009[45]. . . . . 40

2.13 $A_L$ for $e^{\pm}$ from $W^{\pm}$ boson decays for $|\eta| < 1,\ 25 < p_T < 50$ GeV/$c$ from STAR Run 2009[46]. . . . . 41
2.14 $p_T$ distribution of $\mu^{\pm}$ from $W^{\pm}$ in $1.4 < \eta < 2.4$. . . . . 42
2.15 Simulated $W^+ \to \mu^+$ process and muon background processes at $1.4 < |\eta| < 2.4$ with PYTHIA. . . . . 44
2.16 Simulated $W^- \to \mu^-$ process and muon background processes at $1.4 < |\eta| < 2.4$ with PYTHIA. . . . . 45
3.1 RHIC accelerator complex. . . . . 50
3.2 Geometric location of the Local polarimeter (ZDC,SMD) of the PHENIX detector. . . . . 54
3.3 Pseudorapidity($\eta$) and azimuthal angle ($\phi$) coverage for the PHENIX detector subsystems. . . . . 56
3.4 Definition of the global coordinate system used in the PHENIX experiment. . . . . 57
3.5 Detector subsystems of the PHENIX detector in year 2012 run setup. 58
3.6 The PHENIX Central Arm and Muon Arm magnets. . . . . 60
3.7 A layout of extended hadron absorbers. . . . . 63
3.8 Beam Beam Counters (BBC) . . . . . 64
3.9 Arrangement of PMTs in the BBC . . . . . 65
3.10 Drawing of a ZDC module. . . . . 66
3.11 The South Muon ARM tracking spectrometer. . . . . 68

3.12 Picture of Muon Tracker Station 1 . . . . . 69

3.13 A drawing of Iarocci streamer tubes in the MuID. . . . . 73

3.14 A drawing of one gap of the MuID. . . . . 74

3.15 A side view drawing of the MuID gaps. . . . . 75

3.16 PHENIX muon arms upgrades . . . . . 76

3.17 Geometry of the RPC3 strips. . . . . 77

3.18 Layers of the RPCs. . . . . 77

3.19 RPC3 seen from the RHIC beam tunnel. . . . . 78

3.20 FVTX assembled wedge. . . . . 80

3.21 FVTX efficiency. . . . . 81

3.22 Illustration of the PHENIX DAQ system[78]. . . . . 83

3.23 MuID symset logics. . . . . 86

3.24 Schematic illustration of the physics trigger . . . . . 88

4.1 Polarization and total integrated luminosity achieved for the polarized pp runs at RHIC. . . . . 92

4.2 Integrated figure of merit metric vs. day for the Run 2013 running period at RHIC. . . . . 93

4.3 Examples of pileup . . . . . 95

4.4 Collision parameter and BBC vertex distributions . . . . . 97

4.5 Fill-by-fill beam polarizations. . . . . 98

4.6 Simulated muonic subprocesses and hadronic background cross sections. . . . . 103
5.1 Run 2013 $W \rightarrow \mu$ analysis strategy . . . . . 112
5.2 Correlation coefficient between kinematic variables. . . . . 117
5.3 Wness distribution of different sub processes . . . . . 118
5.4 Wness distribution of different sub processes. Data was taken after including efficiencies in the simulations . . . . . 120
5.5 Efficiencies as function of the minimum $W$ likelihood ratio . . . . 121
5.6 Wness comparison among analyzers: Data . . . . . 123
5.7 Wness comparison among analyzers: Signal simulation . . . . . 124
5.8 $Wness$ distributions of valid FVTX events: Data . . . . . 125
5.9 $Wness$ distributions of valid FVTX events: Signal simulation . . 126
5.10 Efficiencies as function of the minimum $W$ likelihood ratio for FVTX valid . . . . . 127
5.11 Successive cuts study for FVTX valid events . . . . . 129
5.12 Relative background rejection versus signal efficiency for FVTX valid events . . . . . 130
5.13 Distributions and PDFs for $W/Z \rightarrow \mu$ events extracted from simulation . . . . . 134
5.14 Distributions and PDFs for hadron background events extracted from data . . . . . 135

5.15 Techniques in $dw_{23}$ extrapolation . . . . . 137
5.16 The fit results used for the signal to background ratio of negative charge muon in south arm. . . . . 139
5.17 The fit results used for the signal to background ratio of positive charge muon in south arm. . . . . 140
5.18 The fit results used for the signal to background ratio of negative charge muon in north arm. . . . . 141
5.19 The fit results used for the signal to background ratio of positive charge muon in north arm. . . . . 142
5.20 Fit results for the PEPSI challenge. . . . . 145
6.1 Raw spin yields including background-dominated region . . . . . 157
6.2 Raw spin yields for signal-dominated region . . . . . 158
6.3 Preliminary single spin asymmetries for Run 2013 for the whole $\eta$ range. . . . . 164
6.4 Preliminary single spin asymmetries for Run 2013 for the 3 $\eta$ bins 165

## 1 Introduction

In modern-day physics, the phenomena ranging from the small scale of subatomic particles ($10^{-18}$ cm) to the large scale of the whole present-day Universe ($10^{28}$ cm) can be described using the four fundamental forces: gravity, electromagnetism, strong and weak interactions. While gravity is governed by Einstein's general relativity, the other three forces can be described to an excellent degree by a quantum field theory of quarks and leptons based on a framework consistent with Einstein's special theory of relativity and quantum mechanics: the so-called the Standard Model (SM)[1]. In the standard model, there are seventeen named elementary particles. The last particles discovered were the Higgs boson in 2012. Elementary particles are either the building blocks of matter, called fermions, or the carriers of forces, called bosons.

The search for elementary particles begun 100 years ago with the discovery of electron. It was followed by 50 years of discovery of many more elementary particles, mostly from cosmic ray experiments, the only source of high energy particles available at that time. This stimulated the development of high energy accelerators, providing intense and controlled beams of known energy that helped scientists to reveal the quark substructure of matter. High energy accelerators such as the Relativistic Heavy Ion Collider (RHIC) at Brookhaven National Laboratory in Long island, NY are fundamental tool to study elementary particles. According

to the de Broglie equation, higher energy probes (or higher momentum transfer from the probes) provide better resolution of the target substructure. For example, a momentum transfer of 1 GeV/$c$ gives a spacial resolution of $10^{-15}$ m which is comparable to size of proton. The other reason for the need for high energy accelerators is that many of elementary particles such as W bosons or top-quark are extremely massive and the energy ($mc^2$) required to create them is large. For example the top quark, which has to be created in pair with its anti-particle, has $mc^2 \simeq 175\ GeV$ which is nearly 200 times mass-energy of proton.

In the early decades of twentieth century, particle-beam energies from accelerators reached only a few MeV and their resolutions were so poor that protons and neutrons could themselves be regarded as point-like. The proton and the neutron was considered to be the spin-1/2 fundamental particle described by the Dirac equation. Later in the 1930s, the magnetic moment of the proton and the neutron was independently measured and the existence of the anomalous magnetic moment of the nucleons turned out[2]. Particularly the finite magnetic moment of the neutron had been a long-standing problem, since the electric charge of the neutron is zero so that the existence of the magnetic moment should imply the substructural "electric current" inside the nucleons.

In the 1960s, a model to describe nucleons with constituent spin-1/2 Dirac particles ("quarks") which have fractional number electric charges as well as the degree of freedom of color charges was proposed by M.Gell-Mann and K.Nishijima[3,

4]. The model was later confirmed by development of high energy accelerator technologies which were capable of probings the substructure of the nucleons by injecting high energy electrons into fixed targets, called as Deep Inelastic Scattering (DIS) experiments ($e + p \rightarrow e + X$, where $X$ can be anything). Measurements from DIS experiments agreed with the model that there are point-like, spin-1/2 charged particles (called quarks) in the proton (Sec. 2.1).

The other important result from polarized DIS experiments was that the polarized parton distribution function (PDF) of quarks, which is the spin dependent distribution of the momentum fraction carried by quarks ($x$) was also measured. The result was striking; the sum of the quark and antiquark polarized PDFs $\frac{1}{2}\Delta\Sigma$ contribute only about 20 to 35 % of the total proton spin $S_p$.

$$S_p = \frac{1}{2} \quad = \quad \frac{1}{2}\Delta\Sigma + \Delta G + L_q + L_g \tag{1.1}$$

The remaining pieces contributing to proton spin are considered to come from gluon polarization $\Delta G$ and orbital angular momenta of quarks $L_q$ and gluons $L_g$ [18, 19, 20, 21, 22, 23, 24, 25, 26, 27, 28, 29, 30, 31]. Generally, polarized DIS experiments have determined the polarization of (quark+antiquark) PDFs with fairly small uncertainties. However, the spin contribution from antiquarks only is much more difficult to probe in DIS experiments.

In the extended method of DIS called semi-inclusive DIS (SIDIS) a scattered charged hadron is measured in addition to the scattered charged lepton, $e +$

$p \rightarrow e + h^{\pm} + X$, where $h^{\pm}$ denotes the scattered $\pi^{\pm}$ or $K^{\pm}$. Polarized SIDIS experiment has been the common technique to probe antiquark polarized PDFs. The SIDIS however has limitations that one needs to know the fragmentation functions to interpret the final-state hadrons. Because of the uncertainity in the fragmentation function, the polarized PDF measurement from SIDIS has large relative uncertainity as compared to the uncertainities in the sum of quark and anti-quark in DIS. Figure 1.1 shows the polarized PDF of quarks, anti-quarks and gluons as extracted from many experiments in the global analysis. In these plots, the valance quark ($u$, $d$) polarizations and the sum of quark and anti-quark polarizations are much better constrained compared to the sea quarks ($\bar{u}$,$\bar{d}$,$s$).

**Production of W bosons in proton-proton collisions** SIDIS experiments give us important information about quark and antiquark polarized PDFs. However, the antiquark polarized PDFs have large uncertainties because of our limited knowledge of fragmentation functions of hadrons. An alternative way of measuring polarized PDFs which doesn't need knowledge of fragmentation function is the production of $W/Z$ bosons from polarized proton-proton collision. $W/Z$ measurement has vital role for determining sea quark polarized PDFs due to the nature of the parity violation of weak interaction and no fragmentation function is involved. If we neglect the small contribution from $s$ quarks, for $W$s produced in pp reactions the $W$ electric charge can be directly related with the parent quark

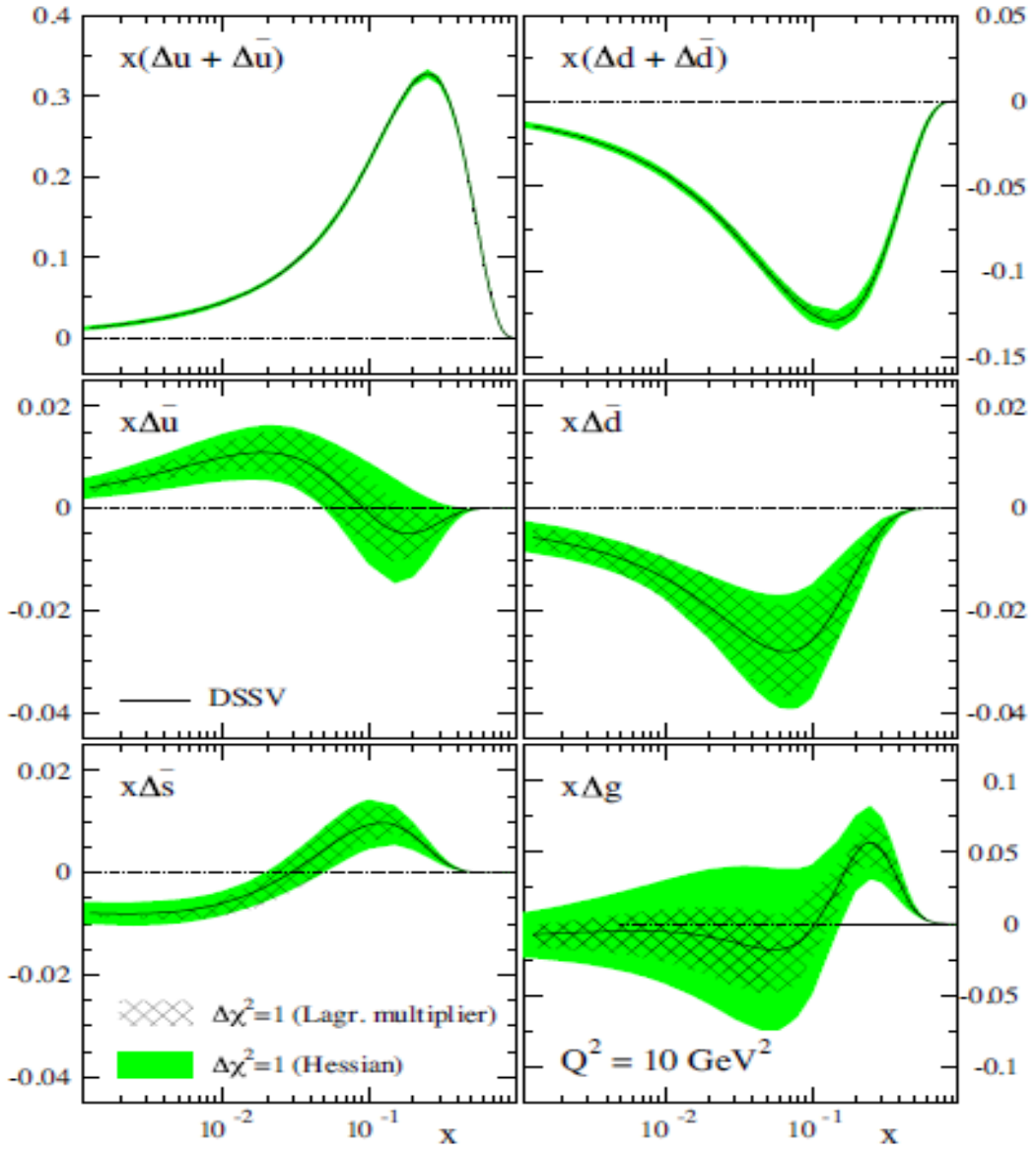



Figure 1.1: Polarized Parton distributions of light quarks and gluons as extracted from the global analysis "DSSV" [9].

flavor: $W^+$ is are produced by $(u\,\bar{d})$, and $W^-$ by $(\bar{u}\,d)$. Moreover, being maximally parity violating, the $W$s can be produced only from left-handed quarks and right-handed antiquarks, therefore knowing the polarization of the proton beam we can determine the parent-quark helicities with respect to the proton spin.

As will be discussed in chapter 5, even though the background processes are supposed to decrease quickly with the muon $p_T$, the low muon tracker momentum resolution smears the background track candidates to much higher momenta. The dominant backgrounds come from hadrons decaying in muon tracker and misreconstructed as high momentum tracks (fake muons). Signal extraction is very challenging especially in the forward rapidities in the range $1.2 < \eta < 2.4$ of PHENIX. There is no Jacobian peak (which is unique property of the signal as discussed in Sec. 2.3.1)unlike to central rapidities in the range $|\eta| < 0.35$. Different techniques of identifying and reducing backgrounds including a new data-driven likelihood procedure have been developed in the PHENIX forward arms.

The RHIC accelerator is the unique facility to collide polarized protons in the world up to the center of mass energy ($\sqrt{s}$) of 510 GeV. RHIC run 13 has been mostly dedicated to spin physics, and in particular the main priority was the forward $W \to \mu$ measurements described in this thesis. The PHENIX detector was used to take the data in this thesis. During the run, proton beams have been collided at a $\sqrt{s} = 510$ GeV, and the final average beam longitudinal polarizations have been 54% for the blue beam, and 55% for the yellow beam. PHENIX

collected a luminosity of 277 $pb^{-1}$, more than three times the total luminosity previously collected during run 2011 (25 $pb^{-1}$) and run 2012 (50 $pb^{-1}$). Most of the discussions and results in this chapter are extracted from the PHENIX Working Group analysis note (an1195) which is approved and internally published in PHENIX archive [54]. The physics background and experimental setup have been similar and are extracted from earlier forward group analysis notes and theses. [54, 82, 89]

**Organization of the thesis** The main goals of this thesis are

- to minimize backgrounds while keeping the signal efficiencies high and determine the signal to background ratio
- use the signal to background ratio to determine final single spin asymmetry of $W/Z \to \mu$ events

The physics of (un) polarized PDFs and the kinematics of $W^{\pm}/Z \to \mu^{\pm}$ in proton-proton collisions are described in chapter 2. Next, the RHIC accelerator and the PHENIX detector systems are described in Chapter 3. In chapter 4 the analyzed real data as well as simulations relevant to the analysis are discussed. Chapter 5 describes each phase of the W analysis strategy used to extract the signal to background ratio. Finally in chapter 6, the results in signal to background ratio and the final spin asymmetries are presented.

# 2 Physics Background

## 2.1 Parton model

Our present knowledge about the high-energy spin structure of the nucleon comes from polarized deep inelastic scattering experiments at CERN, DESY, JLab and SLAC, and high-energy polarized proton-proton collisions at RHIC. In a laboratory, electrons can be accelerated and accurately detected using magnetic spectrometers and standard particle detection techniques. This technique provides superior control over the kinematics quantities of the incident electron and the exchanged virtual photon that probes the nucleon.

In the past few decades many laboratories around the world have discovered a great deal about the internal structure of nucleon using electron-proton scattering processes. There are two types of electron-proton scatterings (elastic and inelastic) which are useful in studying the internal structure of nucleon. The first is, electron-proton elastic scattering in which an electron interacts with proton through a photon exchange. The proton remains intact but with finite recoil. The cross section of this process provides us information about the charge and spatial density distributions. In this discussion we will focus on the second type of scattering called Deep Inelastic Scattering (DIS). In DIS process a constituent of proton called quark in the proton gets knocked out by the virtual photon and the proton gets disintegrated into fragments. This process is useful to extract quark and gluon

distributions in a proton. There is also an extended method of DIS called semi-inclusive DIS (SIDIS), where a scattered charged hadron is measured in addition to the scattered charged lepton. SIDIS is useful to extract quark and gluon spin distributions in a proton.

In electron-proton DIS, consider the momentum transfer from electron of mass $m$ to the target proton of mass $M$ via virtual photon $Q^2$. Also consider a case in which the center of mass of a system ($\sqrt{s}$) is sufficiently higher than proton rest mass ($M$). For convenience, choose a reference frame that the incident electron and proton collide head-on so that the momenta of constituents of the proton are almost collinear with that of the proton itself. With this condition, the constituent of the proton receives a sizable transverse momentum only with the hard scattering process with the probing electron. Interaction scale in the hard process is larger than roughly $\mathcal{O}(1\text{ GeV})$, such that, the perturbative QCD (pQCD) provides reliable calculations. A constituent of a proton carries a momentum fraction $x$ of the the proton itself. During every scattering process, this momentum fraction of the constituent varies from 0 to 1, and we can think of the probability to find the constituent $f$ has the momentum fraction $x$ as $\phi_f(x, Q^2)dx$. The probability functions $\phi_f(x, Q^2)$ are called parton distribution functions (PDFs). If we add all of the momentum fractions carried by partons, we should be able to get the total

momentum $p$ of the proton. Thus PDFs satisfy the condition

$$\sum_f \int_0^1 x\phi_f(x, Q^2)dx = 1 \tag{2.1}$$

where the summation index $f$ refers to the constituents (partons) contributing to the total momentum of the proton. The PDFs are determined by soft QCD quark and gluon processes in the proton. Soft processes refer to the limit where the binding of two quarks become large when $Q^2$ is small, roughly lower than $\mathcal{O}(1\text{ GeV})$. These PDFs are not calculatable with the pQCD. However, the PDFs can be determined by experiments. The parton model is a heuristic picture of hadron structures, but it is fairly effective to describe hard hadronic processes. By using above notations, the electron-proton DIS process cross section to leading order in $\alpha_s$ (the strong coupling constant) is given as

$$\begin{aligned}&\sigma(e(k) + p(P) \to e(k') + X) = \\ &\int_0^1 dx \sum_f \phi_f(x, Q^2) \cdot \sigma\left(e(k) + f(xP) \to e(k') + f(p')\right).\end{aligned} \tag{2.2}$$

The above equation separates ("factors") the cross section to contributions from

- PDF's, Soft partonic structure to be determined from experiments, and
- pQCD, "hard" elastic process of $e + f \to e + f$ , calculable from theory

This separation is called *factorization*. Note that Eq. (2.2) is only the first term of an expansion in $\alpha_s$. If we include the higher order QCD corrections to Eq. (2.2), not only the "hard" contribution but also PDFs need to be corrected.

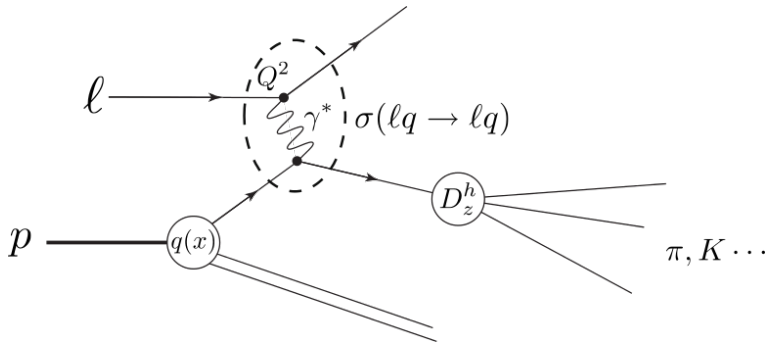



Figure 2.1: Deep inelastic scattering in electron-proton scattering.

There is also an extended method of DIS called semi-inclusive DIS (SIDIS), where a scattered charged hadron is measured in addition to the scattered charged lepton. In the inclusive un-polarized and longitudinally polarized electron-proton DIS scattering $e^{(\rightarrow)} + p^{(\Rightarrow)} \rightarrow e + X$ via virtual photon exchange where $X$ can be anything, it is phenomenologically possible to describe the cross section with a general formula of electromagnetic current-current interaction. In the rest frame of the proton, let the initial and final electron momenta and spins be $(k^\mu, s) = (E, k, s)$ and $(k'^\mu, s') = (E', k', s')$, respectively. Similarly, let the momentum and spin of the proton be $(P^\mu, \mathcal{S}) = (M, 0, \mathcal{S})$, then the differential cross section of the process is given as

$$\frac{d\sigma}{d\Omega dE'} = \frac{\alpha^2}{2Mq^4}\frac{E'}{E}L_{\mu\nu}W^{\mu\nu} \tag{2.3}$$

where $L_{\mu\nu}$ and $W^{\mu\nu}$ are the lepton and proton tensors respectively. $\alpha$ is the electromagnetic coupling constant, and $q^2 \equiv (k - k')^2$ is the momentum transfer.

The lepton tensor is given as

$$L_{\mu\nu} = \left[\bar{u}(k', s')\gamma_\mu u(k, s)\right]^* \left[\bar{u}(k', s')\gamma_\nu u(k, s)\right] \tag{2.4}$$

If not interested on the spin of final state electrons, one can take the sum over the spin of the final state electron. The lepton tensor becomes

$$L_{\mu\nu}(k, s; k') = 2\left[L^S_{\mu\nu}(k; k') + iL^A_{\mu\nu}(k, s; k')\right] \tag{2.5}$$

Where, in the above equation we separated the electron tensor to the initial electron spin-independent symmetric term $L^S_{\mu\nu}$ and the asymmetric spin dependent term $L^A_{\mu\nu}$ as

$$L^S_{\mu\nu} = k_\mu k'_\nu + k'_\mu k_\nu - g_{\mu\nu}(k \cdot k' - m^2) \tag{2.6}$$

$$L^A_{\mu\nu} = m\epsilon_{\mu\nu\rho\sigma}s^\rho(k - k')^\sigma \ . \tag{2.7}$$

Similarly, the hadron tensor $W^{\mu\nu}$ can generally be described (under the parity conservation) with four structure functions $W_1(P{\cdot}q, q^2)$, $W_2(P{\cdot}q, q^2)$, $G_1(P{\cdot}q, q^2)$, $G_2(P \cdot q, q^2)$ as

$$W_{\mu\nu}(q, P) = W^S_{\mu\nu}(q; P) + iW^A_{\mu\nu}(q; P, \mathcal{S}) \tag{2.8}$$

with

$$\begin{aligned}\frac{1}{2}W^S_{\mu\nu}(q; P) &= \left(-g_{\mu\nu} + \frac{q_\mu q_\nu}{q^2}\right) W_1(P \cdot q, q^2) \\ &+ \left[\left(P_\mu - \frac{P \cdot q}{q^2}q_\mu\right)\left(P_\nu - \frac{P \cdot q}{q^2}q_\nu\right)\right]\left[\frac{W_2(P \cdot q, q^2)}{M^2}\right]\end{aligned} \tag{2.9}$$

$$\frac{1}{2}W^A_{\mu\nu}(q;P,\mathcal{S}) = \epsilon_{\mu\nu\rho\sigma}q^\rho$$
$$* \left\{ M\mathcal{S}^\sigma G_1(P\cdot q, q^2) + [(P\cdot q)\mathcal{S}^\sigma - (\mathcal{S}\cdot q)P^\sigma]\,\frac{G_2(P\cdot q, q^2)}{M} \right\} \quad (2.10)$$

$L^S_{\mu\nu},\ W^S_{\mu\nu}$ are both spin-independent symmetric terms where as the asymmetric $L^A_{\mu\nu},\ W^A_{\mu\nu}$ terms depend on spin of the electron and the proton, respectively. Then the differential cross section becomes

$$\frac{d\sigma}{d\Omega dE'} = \frac{\alpha^2}{Mq^4}\frac{E'}{E}\left[L^S_{\mu\nu}W^{S\mu\nu} - L^A_{\mu\nu}W^{A\mu\nu}\right] \quad . \quad (2.11)$$

It is of the convention to use the following notations:

$$F_1 \equiv MW_1(P\cdot q, q^2) \quad (2.12)$$

$$F_2 \equiv \nu W_2(P\cdot q, q^2) \quad (2.13)$$

and

$$g_1(x,Q^2) \equiv \frac{(P\cdot q)^2}{\nu}G_1(P\cdot q, q^2) \quad (2.14)$$

$$g_2(x,Q^2) \equiv \nu(P\cdot q)G_2(P\cdot q, q^2)\ . \quad (2.15)$$

where $\nu \equiv E - E'$. $F_{1,2},\ g_{1,2}$ are functions of $P\cdot q$ and $q^2$, but one can also describe them as functions of $x_B$ and $Q^2$, where

$$x_B \equiv -\frac{q^2}{2P\cdot q} = -\frac{q^2}{2M\nu},\ Q^2 \equiv -q^2 \quad (2.16)$$

$x_B$ is called Bjorken-$x$, and this is identical to the momentum fraction of the parton $x$. If we assume the electron-parton scattering is elastic and the parton

mass is negligible:

$$0 \approx (xP+q)^2 = 2x(P\cdot q) + q^2, \quad x = -\frac{q^2}{2P\cdot q} = x_B \tag{2.17}$$

In this elastic limit, spin-dependent terms vanish and only two spin-independent hadron structure functions $W_1(P\cdot q, q^2)$ and $W_2(P\cdot q, q^2)$ remain. Also, in the case of unpolarized inelastic scattering, the differential cross section given in Eq. (2.11) becomes

$$\frac{d\sigma}{d\Omega dE'} = \frac{4\alpha^2}{q^4}E'^2\left[\frac{F_2(P\cdot q, q^2)}{\nu}\cos^2\frac{\theta}{2} + 2\frac{F_1(P\cdot q, q^2)}{M}\sin^2\frac{\theta}{2}\right] . \tag{2.18}$$

Furthermore, one can identify the patron $f$ as spin-1/2 Dirac particle with fractional electric charge $e_f$, the elastic scattering cross section of unpolarized electron-parton scattering for a given $x$ is

$$\frac{d\sigma^{\text{point}}}{d\Omega dE'}(x, Q^2) = \frac{4\alpha^2 e_f^2}{Q^4}E'^2\left[\frac{x}{\nu}\cos^2\frac{\theta}{2} + \frac{1}{M}\sin^2\frac{\theta}{2}\right]\delta\left(x - \frac{Q^2}{2M\nu}\right) \tag{2.19}$$

Integrating over all the possibilities of a parton momentum $x$ ranging from 0 to 1, and assuming the *factorization* (2.2), the total electron-proton cross section becomes

$$\begin{aligned}
\frac{d\sigma}{d\Omega dE'} &= \int_0^1 dx \sum_f \phi_f(x, Q^2)\frac{d\sigma^{\text{point}}}{d\Omega dE'}(x, Q^2) \\
&= \frac{4\alpha^2}{Q^4}E'^2\int_0^1 dx \sum_f \phi_f(x, Q^2)e_f^2\left[\frac{x}{\nu}\cos^2\frac{\theta}{2} + \frac{1}{M}\sin^2\frac{\theta}{2}\right]\delta\left(x - \frac{Q^2}{2M\nu}\right) \\
&= \frac{4\alpha^2}{Q^4}E'^2\sum_f \phi_f(x, Q^2)e_f^2\left[\frac{x}{\nu}\cos^2\frac{\theta}{2} + \frac{1}{M}\sin^2\frac{\theta}{2}\right]
\end{aligned} \tag{2.20}$$

where,

$$x = \frac{Q^2}{2M\nu} \ .$$

Then comparing the above equation with Eq. (2.18) one finds the structure functions $F_1$ and $F_2$ as

$$F_1(x, Q^2) = \frac{1}{2x} \sum_f \phi_f(x, Q^2) e_f^2 \tag{2.21}$$

$$F_2(x, Q^2) = \sum_f \phi_f(x, Q^2) e_f^2 \tag{2.22}$$

Note that $F_1$ and $F_2$ are not independent of each other anymore and both essentially indicate the same parton distribution functions, although it is allowed to be independent at the first formalism (2.9). This parton model has been verified independently by measuring $F_1$ and $F_2$ experimentally. Generally, important results from DIS experiments are

- the scattered electron interacts with spin-1/2 Dirac particles in the proton;
- $F_1$ and $F_2$ are approximately independent of $Q^2$ at $x \simeq 0.25$. This experimental fact is called Bjorken scaling. Bjorken scaling means the structure of the parton which interacts with the scattering electron does not change no matter how strongl the force used.

These facts from DIS experiments lead to the conclusion that there are point-like, spin-1/2 charged particles (called quarks) in the proton, and the factorization picture is valid.

Even though, DIS experiment supports approximate Bjorken scaling, the PDFs and the structure functions are both functions of $x$ and $Q^2$. However, there is one remarkable result of pQCD. Once we determined PDFs for some values of $Q^2$ as a function of $x$, we can accurately calculate the structure functions at all $Q^2$ as a function of $x$. This evolution of $Q^2$ is well described interms of integral and differential equations known as DGLAP (Dockshitzer-Gribov-Lipatov-Altarelli-Parisi) equations,

$$\frac{d}{d\log Q^2}\phi_i(x,Q^2) \;=\; \sum_j \int_x^1 \frac{d\xi}{\xi} P_{ij}\left(\frac{x}{\xi}, \alpha_s(Q^2)\right)\phi_j(\xi,Q^2) \qquad (2.23)$$

Where $j$ refers to all the constituent partons and $P_{ij}$ are called splitting functions, or evolution kernels. They describe how a quark splits into a quark and a gluon, or how a gluon splits into a pair of quarks or gluons, and so forth. The splitting functions can be calculated within framework of pQCD. At higher $Q^2$ scale, the length-scale of DIS probing becomes smaller. As a result the probability to observe quarks and gluons as "free" or separated "partons" especially in small $x$ region is higher.

## 2.2 Spin structure of the nucleon

### 2.2.1 Polarized DIS

One can also consider DIS experiments with both the electron and the proton polarized. In this experiment, it is possible to measure the two spin dependent

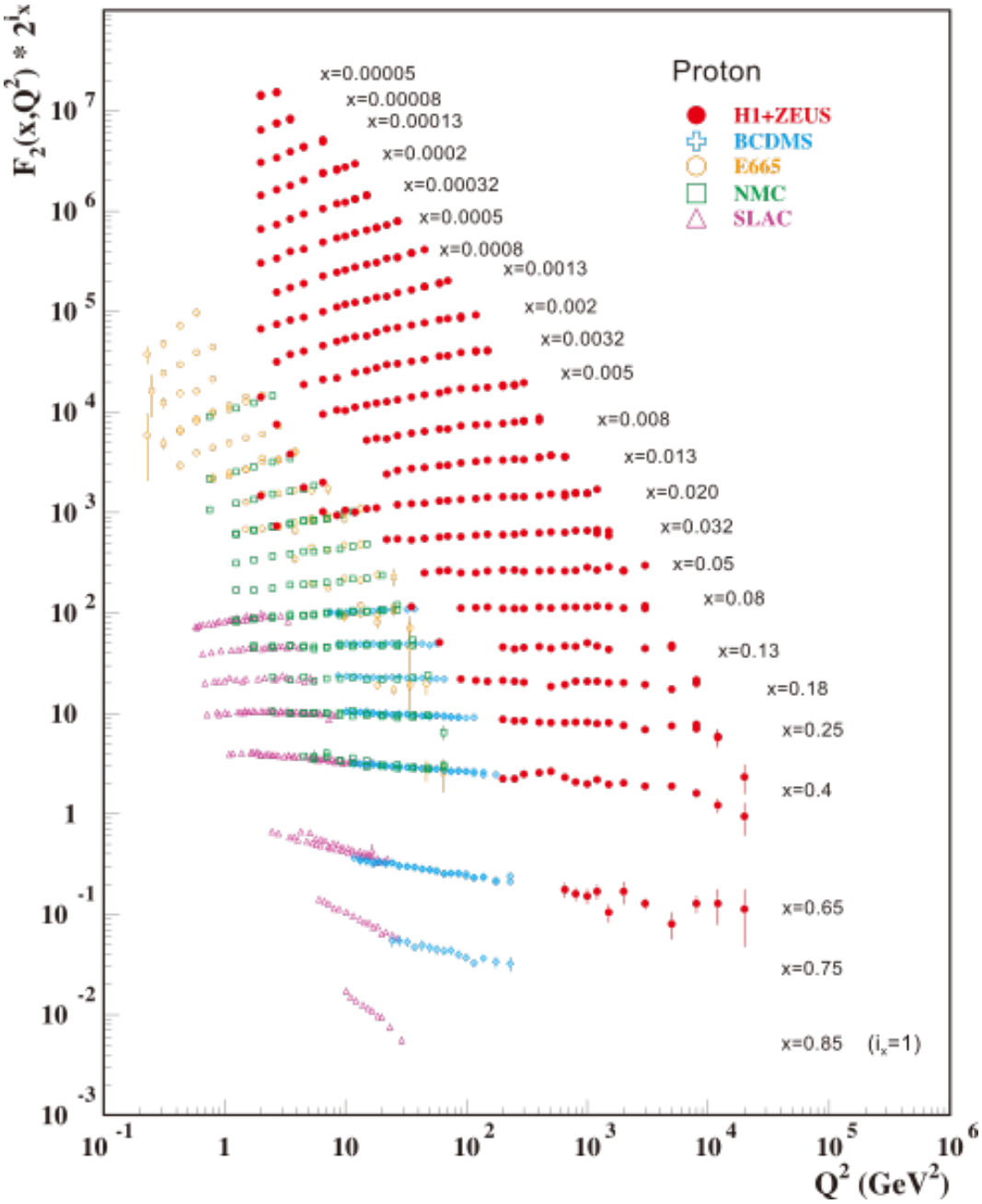



Figure 2.2: $Q^2$ dependence of $F_2(x, Q^2)$ at various $x$ obtained by many experiments[10].

hadron structure functions, $G_1(P\cdot q, q^2)$ and $G_2(P\cdot q, q^2)$ in Eq. (2.10). Let us consider the longitudinally polarized electron-proton collisions first. We discriminate the spin dependent cross sections by putting arrows like $d\sigma^{(\rightarrow\Rightarrow)}$, where the single arrow ($\rightarrow$) denotes the direction of electron polarization and the double arrow ($\Rightarrow$) denotes the direction of proton polarization. Right arrows denote positive helicities and left arrows denote negative helicities. For transverse polarization we use up or down arrows. Due to parity conservation in electromagnetic interactions, identities $d\sigma^{(\rightarrow\Rightarrow)} = d\sigma^{(\leftarrow\Leftarrow)}$ and $d\sigma^{(\rightarrow\Leftarrow)} = d\sigma^{(\leftarrow\Rightarrow)}$ stand. The difference of the cross section by either flipping the electron polarization or flipping the proton polarization is

$$\begin{aligned}\frac{d\Delta\sigma}{d\Omega dE'} &\equiv \frac{d\sigma^{(\rightarrow\Rightarrow)}}{d\Omega dE'} - \frac{d\sigma^{(\rightarrow\Leftarrow)}}{d\Omega dE'} \\ &= -\frac{4\alpha^2}{Q^2 M\nu}\frac{E'}{E}\left[(E+E'\cos\theta)g_1(x,Q^2) - 2xg_2(x,Q^2)\right] \qquad (2.24)\end{aligned}$$

where

$$g_1(x,Q^2) \equiv \frac{(P\cdot q)^2}{\nu} G_1(P\cdot q, q^2) \qquad (2.25)$$

$$g_2(x,Q^2) \equiv \nu(P\cdot q) G_2(P\cdot q, q^2)\ . \qquad (2.26)$$

For a given quark in a proton, we can think of the two possible components: helicity-positive component ("+") and the helicity-negative component ("−"). For example,

$$q_+^{\Rightarrow}(x,Q^2) \qquad (2.27)$$

refers to the helicity-positive ("+") component of PDF when the proton's helicity ($\Rightarrow$) is positive. Summing up the quarks helicity-positive and negative components (those corresponding to the proton's positive helicity $\Rightarrow$) gives the unpolarized PDF:

$$q_+^{\Rightarrow}(x,Q^2) + q_-^{\Rightarrow}(x,Q^2) = q^{\Rightarrow}(x,Q^2) = q(x,Q^2) \tag{2.28}$$

and the following equations stand,

$$q_-^{\Leftarrow}(x,Q^2) = q_+^{\Rightarrow}(x,Q^2), \quad q_+^{\Leftarrow}(x,Q^2) = q_-^{\Rightarrow}(x,Q^2) \tag{2.29}$$

The polarized PDF is defined as

$$\begin{aligned} \Delta q(x,Q^2) &\equiv q_+^{\Rightarrow}(x,Q^2) - q_+^{\Leftarrow}(x,Q^2) \\ &= q_+^{\Rightarrow}(x,Q^2) - q_-^{\Rightarrow}(x,Q^2) \ . \end{aligned} \tag{2.30}$$

The antiquark polarized PDFs, $\Delta\bar{q}(x,Q^2)$, can also be defined in similar way. The difference in spin-dependent cross sections of polarized electron-parton DIS, from Eq. (2.19) is given as

$$\begin{aligned} \frac{d\Delta\sigma^{\text{point}}}{d\Omega dE'} &= \frac{d\sigma^{(\rightarrow\Rightarrow)}_{\text{point}}}{d\Omega dE'} - \frac{d\sigma^{(\rightarrow\Leftarrow)}_{\text{point}}}{d\Omega dE'} \\ &= -\frac{4\alpha^2}{Q^2 M\nu}\frac{E'}{E}e_f^2(E + E'\cos\theta)\delta\left(x - \frac{Q^2}{2M\nu}\right) \ . \end{aligned} \tag{2.31}$$

Summing up over all partons ($f$) the cross section becomes

$$\frac{d\Delta\sigma}{d\Omega dE'} = \int_0^1 dx \sum_f \left[\Delta q_f(x)\frac{d\Delta\sigma^{\text{point}}}{d\Omega dE'} + \Delta\bar{q}_f(x)\frac{d\Delta\sigma^{\text{point}}}{d\Omega dE'}\right] \ , \tag{2.32}$$

and comparing with Eq. (2.24), one finds the spin dependent hadron structure functions

$$g_1(x,Q^2) = \frac{1}{2}\sum_f e_f^2(\Delta q_f(x,Q^2) + \Delta\bar{q}_f(x,Q^2)) \quad (2.33)$$

$$g_2(x,Q^2) = 0 \ . \quad (2.34)$$

To determine the polarized PDFs, one needs to employ Bjorken sum rule, and the flavor SU(3) symmetry of baryon octets which are explained below

**Bjorken sum rule:** The Bjorken sum rule[5] is the most classical rule which bases on isospin symmetry between the proton and the neutron:

$$\int_0^1 [g_1^p(x) - g_1^n(x)]\, dx = \frac{1}{6}\left|\frac{g_A}{g_V}\right|\left(1 - \frac{\alpha_s(Q^2)}{\pi} + \cdots\right) \quad (2.35)$$

where $g_1^p(x)$ and $g_1^n(x)$ are $g_1(x)$ of the proton and the neutron, respectively, and $g_V$ and $g_A$ are the vector and axial-vector coupling constant of the neutron $\beta$-decay. The factor $(1 - \alpha_s(Q^2)/\pi + \cdots)$ represents the higher order corrections. The Bjorken sum rule has been tested by many experiments[6, 7], and results from the experimental data verified the Bjorken sum rule well.

**flavor SU(3) symmetry:** The flavor SU(3) symmetry of baryon octets can also be assumed. In the framework of the flavor SU(3), the $\beta$-decay of the hyperons

are represented with two parameters $F, D$. And the following relations hold[7]:

$$\int_0^1 \left([\Delta u(x) + \Delta\bar{u}(x)] - [\Delta d(x) + \Delta\bar{d}(x)]\right) dx = F + D = \left|\frac{g_A}{g_V}\right| = 1.269 \pm 0.003. \quad (2.36)$$

$$\int_0^1 [(\Delta u(x) + \Delta\bar{u}(x)) + [\Delta d(x) + \Delta\bar{d}(x)] - 2[\Delta s(x) + \Delta\bar{s}(x)]]dx = 3F - D = 0.586 \pm 0.031 \quad (2.37)$$

### 2.2.2 Experiments in determination of polarized quark and antiquark PDFs

As shown in the discussions Eq. 2.32 to Eq. 2.37 the polarized DIS is sensitive to the sum of the quark and antiquark polarized PDFs. Many polarized DIS Experiments have been performed to determine $g_1(x)$. The $g_1(x)$ in the range of $0.01 < x < 0.7$ was first measured at the SLAC[12, 13, 14, 15]and then at the European Muon Collaboration (EMC) experiment in CERN[16, 17]. The measurement was interpreted with flavor SU(3) symmetry model as; that the sum of quark and antiquark polarization is only about $\sim$ 10 % of the total proton spin. The result was striking (spin puzzle), and it urged to confirm the result of the EMC experiment[18, 19, 20, 21, 22, 23, 24, 25, 26, 27, 28, 29, 30, 31]. The recent results confirmed that the sum of the quark and antiquark polarized PDFs contribute only about 20 to 35 % of the total proton spin. The remaining pieces contributing to proton spin are considered to come from gluon polarization

and orbital angular momenta of quarks and gluons. Figure 2.3 summarizes many measurements of $g_1(x)$.

Generally, the spin contribution from antiquarks only is very difficult to probe in DIS experiments. Polarized semi-inclusive DIS (SIDIS) experiment has been the common technique to probe antiquark polarized PDFs. Detectors in SIDIS are designed to detect not only scattered electrons but also the final state hadron. However the SIDIS has limitations that one needs to know the fragmentation functions to interpret the final-state hadrons. Because of the uncertainity in the fragmentation function, the polarized PDF measurement from SIDIS has large relative uncertainity as compared to the uncertainities in the sum of quark and anti-quark in DIS. The plots shown in chapter 1 Figure 1.1 shows the polarized PDF distributions as extracted from many experiments in the global analysis. In these plots, the valance quark ($u$, $d$) polarizations, sum of quark and anti-quark polarizations are much better constrained compared to the sea quarks ($\bar{u}$,$\bar{d}$,$s$).

## 2.3 $W/Z$ bosons Production and decay from proton-proton collisions

SI(DIS) experiments give us important information about quark and antiquark polarized PDFs. However, the antiquark polarized PDFs have large uncertainties because of our limited knowledge of fragmentation functions of hadrons. An alternative way of measuring polarized PDFs which doesn't need knowledge of fragmentation function is the production of $W/Z$ bosons from polarized proton-

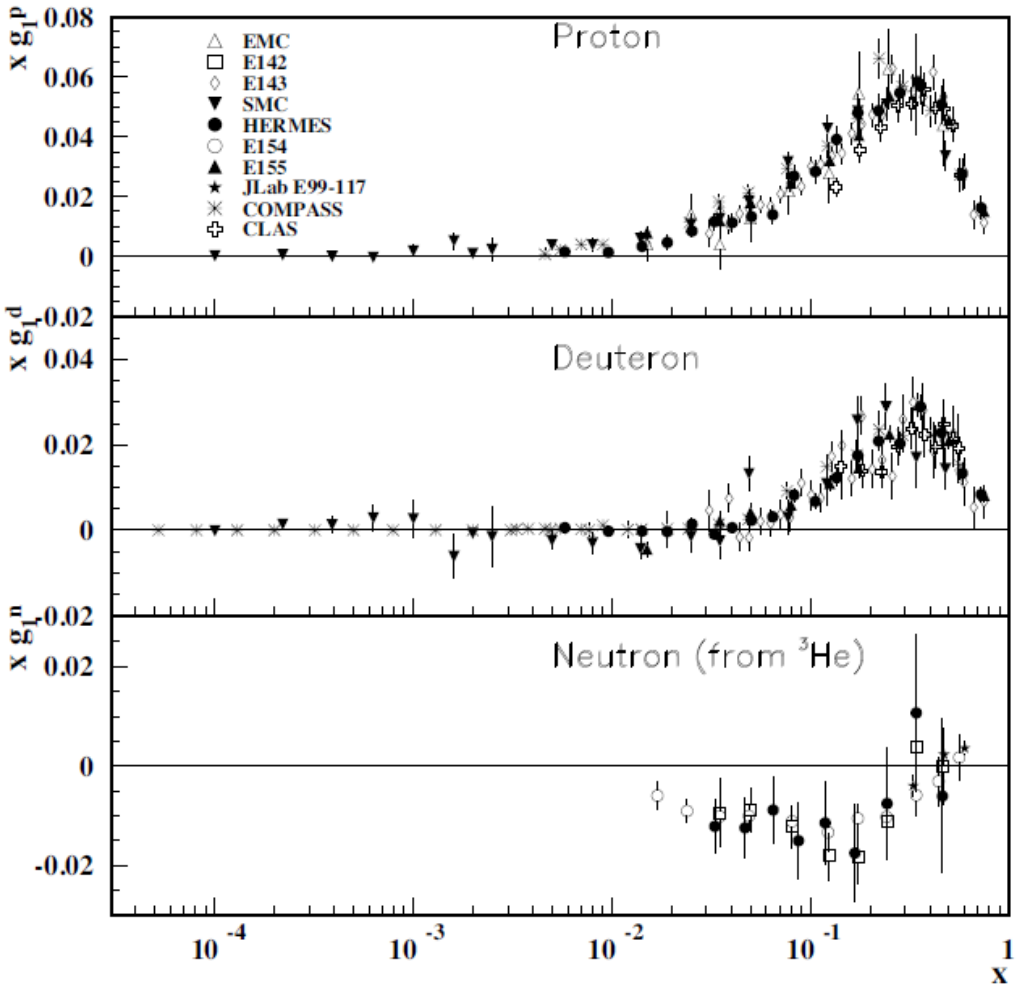



Figure 2.3: Summary of various $g_1(x)$ measurements for proton, deuteron, and neutron[10].

proton collision. $W/Z$ measurement has vital role for determining sea quark polarized PDFs due to the nature of the parity violation of weak interaction and no fragmentation function is involved. The so called $W$ measurement involve two step processes. For $W^+$ for example

$$p + p \rightarrow W^+ \rightarrow \ell^+ \bar{\nu}_\ell$$

The first subprocess is hadronic production of $W$ and the second is $W$ decay to lepton also called leptonic decay. Each process will be discussed in the next sections.

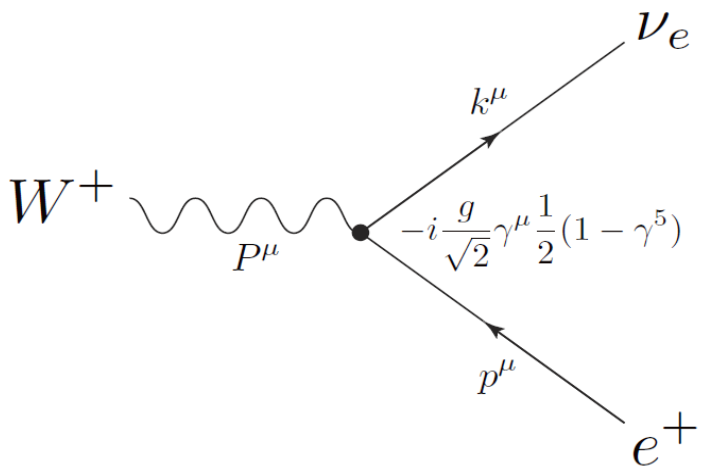



Figure 2.4: Leptonic decay mode $W^+ \rightarrow e^+\nu_e$.

**$W$ bosons:** $W$ bosons $(W^+, W^-)$ are gauge bosons of weak interaction with mass of $80.40 \pm 0.02$ GeV/$c^2$. Unlike to electromagnetic or strong gauge bosons, the coupling of $W$ bosons with fermions is maximally parity-violating. This type

of interaction of $W$ bosons is also called $V-A$ interaction. If we consider the leptonic decay of $W$ bosons, for example for $W^+ \to e^+\nu_e$ the matrix element of the process is given by

$$\mathcal{M} = -i\frac{g}{\sqrt{2}}\epsilon_\mu^\lambda(P)\bar{\nu}(k)\gamma^\mu\frac{1}{2}(1-\gamma^5)e(p) \tag{2.38}$$

where $\epsilon$ is W-boson polarization, $\gamma$'s are gamma matrices, the momenta (4 vectors $P$, $p$ and $k$ for $W$, $e$ and $\nu$ respectively )and the vertex coupling (coupling strength $g$) are as labeled in Figure 2.4. Averaging $|\mathcal{M}|^2$ over the polarization of $W^+$ and summing over the fermion spins, at the massless limit of $e^+$ we obtain

$$\frac{1}{3}\sum_{\text{spin}}|\mathcal{M}|^2 = \frac{1}{3}g^2M_W^2 \ . \tag{2.39}$$

Consequently the partial decay width of the sub-process is

$$\Gamma(W^+ \to e^+\nu_e) = \frac{1}{48\pi}g^2M_W = \frac{G_F}{\sqrt{2}}\frac{M_W^3}{6\pi} \equiv \Gamma_W^0 \tag{2.40}$$

where $G_F$ is the Fermi coupling constant and $g^2 = 8M_W^2G_F/\sqrt{2}$. As long as the mass of leptons are negligible compared to the parent particle, the partial decay width is universal for other families of lepton pairs; $e^+\nu_e, \mu^+\nu_\mu, \tau^+\nu_\tau$. The other $W$ decay channels are hadronic decays. They are similar to leptonic decay but we need to add QCD corrections; such as, the color factor and the flavor mixing factor:

$$\Gamma(W^+ \to q_i\bar{q}_j) = 3|V_{ij}|^2\Gamma_W^0\left(1+\frac{\alpha_s(M_W)}{\pi}+\cdots\right) \tag{2.41}$$

where the factor 3 is the degree of freedom of color, $V_{ij}$ is Cabbibo-Kobayashi-Maskawa (CKM) matrix element in the Wolfenstein's approximation [32]

$$V_{ij} \equiv \begin{pmatrix} V_{ud} & V_{us} & V_{ub} \\ V_{cd} & V_{cs} & V_{cb} \\ V_{td} & V_{ts} & V_{tb} \end{pmatrix} \approx \begin{pmatrix} 1-\lambda^2/2 & \lambda & A\lambda^3(\rho - i\eta) \\ -\lambda & 1-\lambda^2/2 & A\lambda^2 \\ A\lambda^3(1-\rho-i\eta) & -A\lambda^2 & 1 \end{pmatrix} \quad (2.42)$$

$$\lambda = 0.2257^{+0.0009}_{-0.0010},\ A = 0.814^{+0.021}_{-0.022},\ \rho = 0.135^{+0.031}_{-0.016},\ \eta = 0.349^{+0.015}_{-0.017}\ . \quad (2.43)$$

The decay $W^+ \to t\bar{b}, t\bar{s}, t\bar{d}$ is prohibited, because the mass of $t$-quark is heavier than $W$ bosons. Neglecting the QCD correction factor and approximating the sum of hadronic decays by

$$\sum_{(i,j),i\neq t} |V_{ij}|^2 \simeq 2, \quad (2.44)$$

the branching ratio of the leptonic decays $W^+ \to \ell^+ \bar{\nu}_\ell$ is about $1/9 \simeq 0.11$, where $\ell$ is any of the charged leptons. And for hadronic decay the branching ratio is $6/9 = 2/3\ \simeq 0.67$

$Z$ boson is neutral massive electroweak gauge boson with the mass of $91.1876 \pm 0.0021$ GeV/$c^2$. The coupling of $Z$ with fermions is similar to photon, but because of weak interaction, coupling with $Z$ violates parity conservation. The degree of parity violation differs by fermions, and it is parameterized with two coefficients $c_V^f, c_A^f$. Where $f$ denotes the flavor of the fermion. The relative strength of the coupling constant of $Z$ differs from that of $W^\pm$ by factor $\sqrt{2}/\cos\theta_W$, where $\theta_W$ is a fundamental constant of the Standard Model called the Weinberg angle. The

matrix element of the leptonic decay of $Z$ boson $Z \to e^+e^-$ is

$$\mathcal{M} = -i\frac{g}{\cos\theta_W}\epsilon_\mu^\lambda(P)\bar{e}(k)\gamma^\mu\frac{1}{2}(c_V^e - c_A^e\gamma^5)e(p) \tag{2.45}$$

To calculate the partial decay width, we follow similar procedure to $W^\pm$ case. Applying $c_V, c_A$ of each fermion and imposing the negligible fermion mass limit at the first order, the decay widths are

$$\Gamma(Z \to \bar{\nu}\nu) = \Gamma_Z^0 \equiv \frac{G_F M_Z^3}{12\pi\sqrt{2}} \tag{2.46}$$

$$\Gamma(Z \to \ell^+\ell^-) = \Gamma_Z^0\left(1 - 4\sin^2\theta_W + 8\sin^4\theta_W\right) \tag{2.47}$$

$$\Gamma(Z \to \bar{u}u, \bar{c}c, \bar{b}b) = \Gamma_Z^0\left(1 - \frac{8}{3}\sin^2\theta_W + \frac{32}{9}\sin^4\theta_W\right) \tag{2.48}$$

$$\Gamma(Z \to \bar{d}d, \bar{b}b) = \Gamma_Z^0\left(1 - \frac{4}{3}\sin^2\theta_W + \frac{8}{9}\sin^4\theta_W\right) \tag{2.49}$$

where $\sin^2\theta_W \approx 0.23$. Note that $Z \to \bar{t}t$ is again prohibited. As a result, the branching ratio of $Z \to \ell^+\ell^-$ is about 3.36 %.

### 2.3.1 Hadronic production and decays of $W$ bosons

**Hadronic productions of $W$:** The dominant $W$ production from hadrons is the sub-process

$$q_i\bar{q}_j \to W^+$$

where $q_i$ is $u, c, t$-quarks and $\bar{q}_j$ is $\bar{d}, \bar{s}, \bar{b}$-antiquarks. Using momenta labeled ($p_1$, $p_2$ and $P$ for $q$, $\bar{q}$ and $W$ respectively) as Figure 2.5, the matrix element and cross

section of the sub-process are

$$\mathcal{M} = -i\frac{g}{\sqrt{2}}V_{ij}\epsilon_{\mu}^{\lambda}(P)\bar{q}_j(p_2)\frac{1}{2}\gamma^{\mu}(1-\gamma^5)q_i(p_1) \tag{2.50}$$

$$\hat{\sigma}(q_i\bar{q}_j \to W^+) = 2\pi|V_{ij}|^2\frac{G_F}{\sqrt{2}}M_W^2\delta(\hat{s}-M_W^2) \tag{2.51}$$

where $\hat{s}$ is square of the center of mass energy of the subprocess, $\hat{s} = (p_1+p_2)^2$.

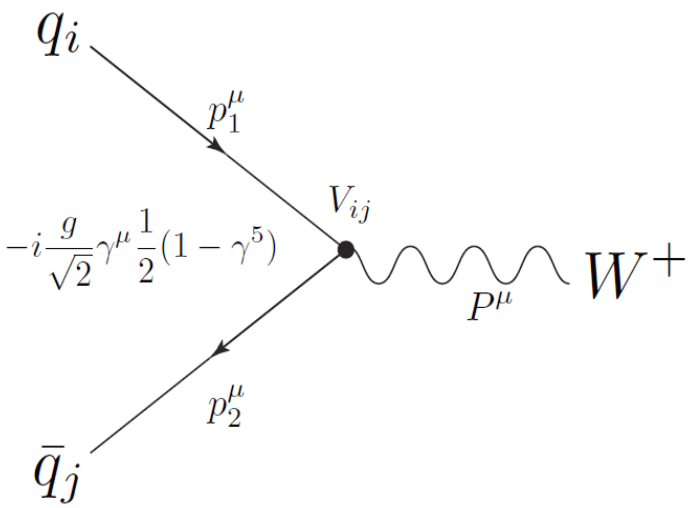



Figure 2.5: Hadronic production subprocess of $W^+$.

According to the factorization theorem the total $W^+$ production cross section in proton-proton collision is at the leading order

$$\sigma(pp \to W^+) = \frac{K}{3}\int dx_1 dx_2 \sum_{i,j} q_i(x_1, M_W^2)\bar{q}_j(x_2, M_W^2)\hat{\sigma}(q_i\bar{q}_j \to W^+) \tag{2.52}$$

where $q_i(x, M_W^2)$, $\bar{q}_j(x, M_W^2)$ are quark and antiquark PDFs at $Q^2 = M_W^2$. $K$ is called the $K$-factor which includes the first order QCD corrections,

$$K = 1 + \frac{8\pi}{9}\alpha_s(M_W^2) + \cdots \tag{2.53}$$

and the factor 1/3 is the color factor.

In terms of the *rapidity* of the $W$ boson ($y_W$), the differential cross section becomes

$$\frac{d\sigma}{dy_W}(pp \to W^+) = K\frac{2\pi G_F}{3\sqrt{2}} \sum_{i,j} |V_{ij}|^2 x_1 x_2 q_i(x_1, M_W^2)\bar{q}_j(x_2, M_W^2) \tag{2.54}$$

$$\begin{aligned}\frac{d\sigma}{dy_W}(pp \to W^+) \simeq K\frac{2\pi G_F}{3\sqrt{2}} x_1 x_2 \big[&\cos^2\theta_c \left\{u(x_1)\bar{d}(x_2) + \bar{d}(x_1)u(x_2)\right\} \\ &+ \sin^2\theta_c \left\{u(x_1)\bar{s}(x_2) + \bar{s}(x_1)u(x_2)\right\}\end{aligned}$$

where $\theta_c$ is the Cabbibo angle. The Cabbibo angle suppresses the second term (contribution from $\bar{s}$) by factor $\sim 18$. $x_1, x_2$ is related with $y_W$ as

$$x_{1,2} = \frac{M_W}{\sqrt{s}} e^{\pm y_W}. \tag{2.55}$$

The production cross section is then found by integrating over $y_W$. $y_W$ has kinematical limit of

$$-\ln\left(\frac{\sqrt{s}}{M_W}\right) < y_W < \ln\left(\frac{\sqrt{s}}{M_W}\right) \ . \tag{2.56}$$

In case of $\sqrt{s} = 510$ GeV this is $-1.84 < y_W < 1.84$. Figure 2.6 shows the total cross section of $W^\pm$ times the branching ratio of $W^\pm \to \ell^\pm \nu_\ell$ as a function of $\sqrt{s}$ for $pp$ and $p\bar{p}$ collisions.

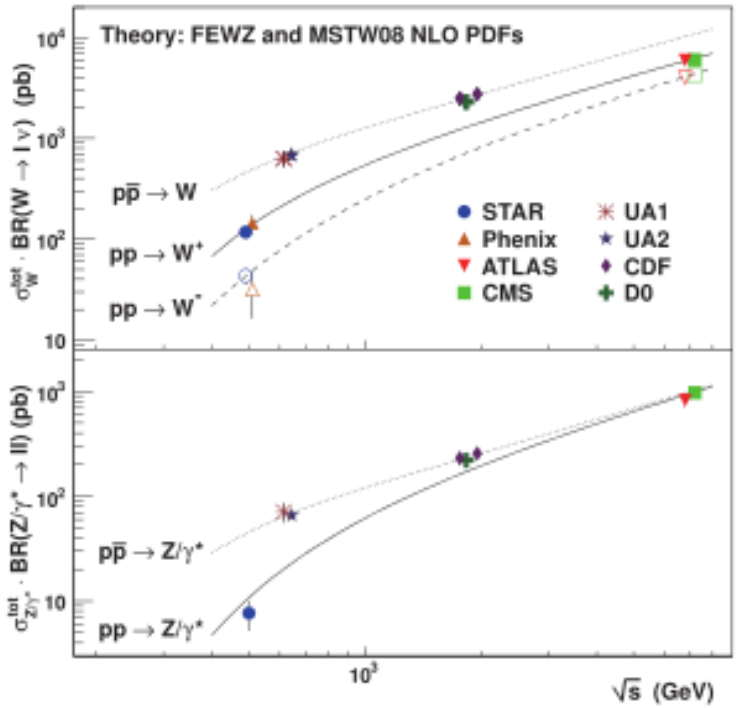



Figure 2.6: Measurements of production cross section of $W^{\pm} \to \ell^{\pm}\bar{\nu}$ and $Z \to \ell^{+}\ell^{-}$ in proton-proton and proton-antiproton collisions at various $\sqrt{s}$ [33, 34, 35, 36, 37, 38, 39, 40, 41, 42, 43, 44].

**Leptonic decay of $W$:** The second subprocess of $pp \to W^+ \to \ell^+\bar{\nu}_\ell$ is the leptonic decay process in

$$u\bar{d} \to W^+ \to \ell^+\bar{\nu}_\ell \ . \tag{2.57}$$

In the $\ell^+\nu_\ell$ rest frame, the center of mass scattering angle $\hat{\theta}$ is defined as the angle between $u$ and $\ell^+$. The matrix element and the corresponding cross section,with summing up the matrix elements over the spin of the final states,are

$$\mathcal{M} = i\frac{G_F}{\sqrt{2}}M_W^2 V_{ud}\frac{\bar{d}\gamma^\mu(1-\gamma^5)u\bar{\nu}\gamma_\mu(1-\gamma^5)\ell}{\hat{s}-M_W^2+iM_W\Gamma_W} \tag{2.58}$$

$$\frac{d\hat{\sigma}}{d\cos\hat{\theta}}(u\bar{d}\to W^+\to\ell^+\nu_\ell) = \frac{|V_{ud}|^2}{8\pi}\left(\frac{G_F M_W^2}{\sqrt{2}}\right)^2\frac{\hat{s}(1-\cos\hat{\theta})^2}{(\hat{s}-M_W^2)^2+(\Gamma_W M_W)^2} \tag{2.59}$$

where $\hat{s}$ is square of the center of mass energy, $M_W$ is the mass of $W^+$, $\Gamma_W$ is the decay width of $W^+$, and $\bar{d}, u, \bar{\nu}, \ell$ are the fermion external lines of the corresponding flavors. The above equation implies,

$$\frac{d\hat{\sigma}}{d\cos\hat{\theta}}(u\bar{d}\to W^+\to\ell^+\nu_\ell) \propto (1-\cos\hat{\theta})^2. \tag{2.60}$$

The factor $(1-\cos\hat{\theta})^2$ is the direct consequence of parity violation. The $W^+$ boson in the maximally parity violating interaction couples only the left-handed $u$-quark and the right-handed $\bar{d}$-quark. This forces the produced $W^+$ boson to be perfectly polarized to the direction of the right-handed $\bar{d}$-direction. The neutrino from the $W^+$ decay must be left-handed, then the charged lepton prefers to be emitted to $\bar{d}$-direction.

Similarly, for $W^-$ production case, if we take $\hat{\theta}$ as the angle between $d$ and $\ell^-$, we obtain

$$\frac{\hat{\sigma}}{d\cos\hat{\theta}}(d\bar{u} \to W^- \to \ell^-\nu_\ell) \propto (1+\cos\hat{\theta})^2. \tag{2.61}$$

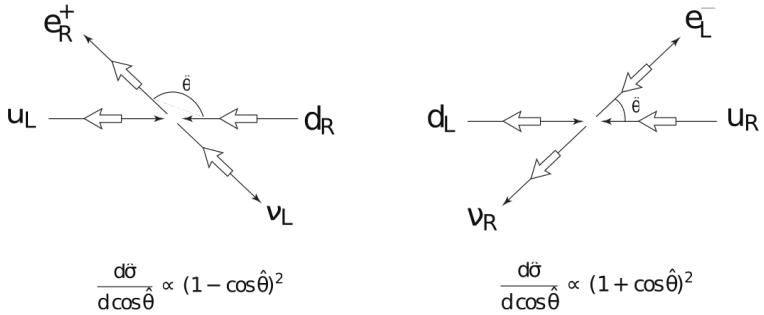



Figure 2.7: Helicity conservation in production and decay of $W^\pm$ boson.

In terms of the rapidity $\hat{y}_{\ell\pm}$ of the scattered lepton in the center of mass frame of $W$ production, the cross section is given as

$$\frac{d\hat{\sigma}}{d\hat{y}_{\ell\pm}} = \sin^2\hat{\theta}\frac{d\hat{\sigma}}{d\cos\hat{\theta}} \propto \sin^2\hat{\theta}(1\mp\cos\hat{\theta})^2 \simeq \left(\frac{1\mp\tanh\hat{y}_{\ell\pm}}{\cosh\hat{y}_{\ell\pm}}\right)^2, \tag{2.62}$$

Or, if we transform the center of mass frame rapidity $\hat{y}_{\ell\pm}$ to the lab frame rapidity $y_{\ell\pm}$, we obtain the cross section in the lab rapidity distribution as

$$\frac{d\sigma}{dy_{\ell\pm}} = \frac{1}{3}\int dx_1 dx_2 \sum_{i,j} q_i(x_1)\bar{q}_j(x_2)\left[\frac{d\hat{\sigma}}{d\cos\hat{\theta}}(q_i\bar{q}_j \to \ell^\pm\nu)\sin^2\hat{\theta}\right]. \tag{2.63}$$

Since quark PDFs are dominated by contributions from valance quarks, quark PDFs have relatively high probability to have larger $x$ (carry most fraction of proton momentum) as compared to antiquarks. Then for $W^+$ production the

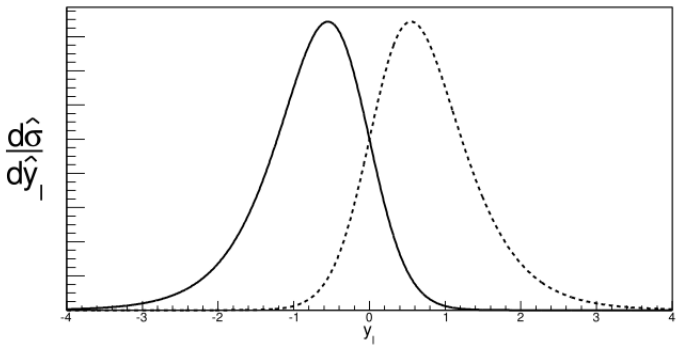



Figure 2.8: The rapidity distribution of the charged lepton from $W$ decays at the center of mass frame. The solid line is of $W^+ \to \ell^+$ and the dotted line is of $W^- \to \ell^-$.

rapidity of the $W^+$ tends to be along with the $u$-quark direction, while for $W^-$ production the rapidity of the $W^-$ tends to be along with the $d$-quark direction.

**Jacobian peak** In the center of mass frame, the decayed lepton carries transverse momentum $\hat{p}_T$ which is equal to half of the mass of the parent $W$ boson,

$$\hat{p}_T = \frac{\sqrt{s}}{2}\sin\hat{\theta} \quad \text{or} \quad \cos\hat{\theta} = \left(1 - 4\frac{\hat{p}_T^2}{\hat{s}}\right)^{1/2}, \tag{2.64}$$

If we consider the differential of the second part of the above equation, we get

$$\frac{d\cos\hat{\theta}}{d\hat{p}_T^2} = -\frac{2}{\hat{s}}\left(1 - 4\frac{\hat{p}_T^2}{\hat{s}}\right)^{1/2} . \tag{2.65}$$

The differential cross section in terms of $\hat{p}_T$ is then

$$\frac{d\hat{\sigma}}{d\hat{p}_T^2} = 3\frac{\hat{\sigma}}{\hat{s}}\frac{(1 - 2\hat{p}_T^2/\hat{s})}{(1 - 4\hat{p}_T^2/\hat{s})^{1/2}} \tag{2.66}$$

This cross section has a singularity at $\hat{p}_T = \sqrt{s}/2 = M_W/2$, which corresponds to the maxima at 40 GeV/c. This peak is known as the Jacobian peak. This peak

is dominated by leptons from $W$ decays whose direction at the center of mass frame is perpendicular to the beam axis. This perpendicular direction corresponds to low (mid) rapidity range. For this reason, at larger (forward or backward) rapidities the probability of having the Jacobian peak is rare (see Figure 2.14).

In this thesis, we measure charged muon from muon from $W$ decay in the forward rapidity. So, we may not see the peak at $p_T = M_W/2$.

### 2.3.2 Hadronic production and decays of $Z$ bosons

$Z$ boson's hadronic production in proton-proton collision is similar to the $W$ boson production. The production subprocess is

$$q\bar{q} \to Z \tag{2.67}$$

with the matrix element and the cross section of the subprocess are given by

$$|\mathcal{M}|^2 = 32\frac{G_F}{\sqrt{2}}\left((c_V^q)^2 + (c_A^q)^2\right) M_Z^4 \tag{2.68}$$

$$\frac{d\sigma}{dy_Z}(pp \to Z) = K\frac{8\pi}{3}\frac{G_F}{\sqrt{2}}\sum_q \left((c_V^q)^2 + (c_A^q)^2\right) x_1 x_2 q(x_1)\bar{q}(x_2). \tag{2.69}$$

If we insert the PDFs, we find the production cross section of $Z$ is smaller than that of $W$ production.

The cross section for the leptonic decay of $Z$ is also very small. Because of the combined effect of smaller production cross section and smaller branching ratio, the ratio of $p + p \to Z \to \ell^+\ell^-$ to $p + p \to W^\pm \to \ell^\pm\nu_\ell$ is about 1/10.

## 2.4 Probing sea quark polarization via $W/Z$ bosons

### 2.4.1 Longitudinal single spin asymmetry $A_L^{\ell\pm}$

For longitudinally-polarized proton-proton collisions, the single spin asymmetry is defined as

$$A_L \equiv \frac{d\sigma^{\Rightarrow} - d\sigma^{\Leftarrow}}{d\sigma^{\Rightarrow} + d\sigma^{\Leftarrow}} \tag{2.70}$$

where $d\sigma^{\Rightarrow} = d\sigma(p^{\Rightarrow}p \to X)$, $d\sigma^{\Leftarrow} = d\sigma(p^{\Leftarrow}p \to X)$. Non zero $A_L$ appears because of parity-violating processes. If we apply the massless limit of quarks, the helicity state is identical to the chirality state. For the two possible orientations of the polarized proton spin in the polarized $pp$ collision, the cross sections for the combined hadronic production and decay sub processes are

$$\begin{aligned} d\sigma(p^{\Rightarrow}p \to W^+ \to \ell^+\nu_\ell) &= \frac{K}{3}\int dx_1 dx_2 \sum_{i,j} \left(q_{i-}^{\Rightarrow}(x_1)\bar{q}_{j+}(x_2) + \bar{q}_{j+}^{\Rightarrow}(x_1)q_{i-}(x_2)\right) \\ &\quad \times d\hat{\sigma}(q_i\bar{q}_j \to W^+ \to \ell^+\nu_\ell) \end{aligned} \tag{2.71}$$

$$\begin{aligned} d\sigma(p^{\Leftarrow}p \to W^+ \to \ell^+\nu_\ell) &= \frac{K}{3}\int dx_1 dx_2 \sum_{i,j} \left(q_{i-}^{\Leftarrow}(x_1)\bar{q}_{j+}(x_2) + \bar{q}_{j+}^{\Leftarrow}(x_1)q_{i-}(x_2)\right) \\ &\quad \times d\hat{\sigma}(q_i\bar{q}_j \to W^+ \to \ell^+\nu_\ell)\ . \end{aligned} \tag{2.72}$$

Recalling the definition of polarized PDFs that $\Delta q(x) \equiv q_+^{\Rightarrow} - q_-^{\Rightarrow}$,

$$\begin{aligned} A_L(p^{\Rightarrow}p \to W^+ \to \ell^+\nu_\ell) &= \frac{\int dx_1 dx_2 \sum_{i,j} \left(-\Delta q_i(x_1)\bar{q}_j(x_2) + \Delta\bar{q}_j(x_1)q_i(x_2)\right)\cdot d\hat{\sigma}}{\int dx_1 dx_2 \sum_{i,j} \left(q_i(x_1)\bar{q}_j(x_2) + \bar{q}_j(x_1)q_i(x_2)\right)\cdot d\hat{\sigma}} \\ &\approx \frac{\int dx_1 dx_2 \left(-\Delta u(x_1)\bar{d}(x_2) + \Delta\bar{d}(x_1)u(x_2)\right)\cdot d\hat{\sigma}}{\int dx_1 dx_2 \left(u(x_1)\bar{d}(x_2) + \bar{d}(x_1)u(x_2)\right)\cdot d\hat{\sigma}} \end{aligned} \tag{2.73}$$

As discussed in the previous sections, terms with $u\bar{s}$ are supressed because of the small Cabbibo angle. Therefore we neglected the small contributions from $u\bar{s}$ and

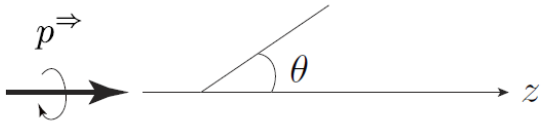



Figure 2.9: The convention of the coordinate system for spin asymmetry.

other channels, and only considered production in $u\bar{d}$. In particular, we focus on the charged lepton rapidity dependence of $A_L$. If we denote the $A_L$ of $W^+ \to \ell^+\nu_\ell$ as a function of $y_\ell$ as $A_L^{\ell+}(y_\ell)$, single spin asymmetry becomes

$$A_L^{\ell+}(y_\ell) = \frac{\int dx_1 dx_2 \left(-\Delta u(x_1)\bar{d}(x_2)(1-\cos\hat{\theta})^2 + \Delta\bar{d}(x_1)u(x_2)(1+\cos\hat{\theta})^2\right)}{\int dx_1 dx_2 \left(u(x_1)\bar{d}(x_2)(1-\cos\hat{\theta})^2 + \bar{d}(x_1)u(x_2)(1+\cos\hat{\theta})^2\right)} \quad (2.74)$$

Where, $\hat{\theta}$ is re-defined as the angle between the direction of the momentum of the polarized proton and the charged lepton at the center of mass frame. The rapidity $y_\ell$ is positive (negative) when $p_z^\ell > 0$ ($p_z^\ell < 0$), where the $z$-axis is parallel with the momentum of the polarized proton (Figure 2.9). Similarly, $A_L$ of $W^- \to \ell^-\nu_\ell$ as a function of $y_\ell$ as $A_L^{\ell-}(y_\ell)$ is given by

$$A_L^{\ell-}(y_\ell) = \frac{\int dx_1 dx_2 \left(\Delta\bar{u}(x_1)d(x_2)(1-\cos\hat{\theta})^2 - \Delta d(x_1)\bar{u}(x_2)(1+\cos\hat{\theta})^2\right)}{\int dx_1 dx_2 \left(\bar{u}(x_1)d(x_2)(1-\cos\hat{\theta})^2 + d(x_1)\bar{u}(x_2)(1+\cos\hat{\theta})^2\right)} \quad (2.75)$$

Eq. (2.74) and (2.75) are both convolutions over $x_1$ and $x_2$, and quark and antiquark PDFs are coupled in such a way that the antiquark PDFs are not directly extracted. However, it is also possible to make some qualitative arguments about the sensitivity of the antiquark PDFs to different rapidity ranges. For the $W^- \to \ell^-\nu_\ell$ case, large negative $y_\ell$ corresponds to $\hat{\theta} \sim \pi$ and $x_1 \ll x_2$, then the

convolution over $x_1, x_2$ is approximately decomposed. Then the second term of the $d\bar{u}$ coupling is highly suppressed. This limit reduces the asymmetry to

$$A_L^{\ell^-}(y_\ell \to \text{large neg.}) \approx \frac{\Delta\bar{u}(x_1)}{\bar{u}(x_1)} \tag{2.76}$$

Similarly, for large positive $y_\ell$ case, $\hat{\theta} \sim 0$ and $x_1 \gg x_2$. In this case, on the contrary, the second term dominates. Therefore, this limit reduces the asymmetry to

$$A_L^{\ell^-}(y_\ell \to \text{large pos.}) \approx \frac{\Delta d(x_1)}{d(x_1)} \tag{2.77}$$

Thus $A_L$ measurements of $W^- \to \ell^-\bar{\nu}_\ell$ at large positive or negative rapidity regions are very sensitive to $\Delta\bar{u}(x)$ and $\Delta d(x)$ respectively. For $W^+ \to \ell^+\nu_\ell$ case, however, the convolution over $x_1, x_2$ is not decomposed, for large positive/negative rapidities. Both the first and the second term of Eq. (2.74) almost equally contribute. Thus measuring $A_L^{\ell+}$ for wide rapidity range is desired to constrain on polarized PDFs. Figure 2.10 shows $A_L$ of $W^\pm \to \ell^\pm$ at $\sqrt{s} = 500$ GeV with the CHE NLO generator[11] as a function of $y_\ell$ with DSSV08 global analysis of polarized PDFs[9].

**Effect of $Z$ boson on $A_L^{\ell\pm}$** Because of the small production and decay cross section of $Z$ boson as compared to $W^\pm$, the single spin asymmetry $A_L^{\ell\pm}$ is dominated by $W^\pm$. Besides, in the decay process $Z^\pm \to \ell^+\ell^-$ contribution from one of the two charged lepton is not always observed in the detector. PHENIX is non-

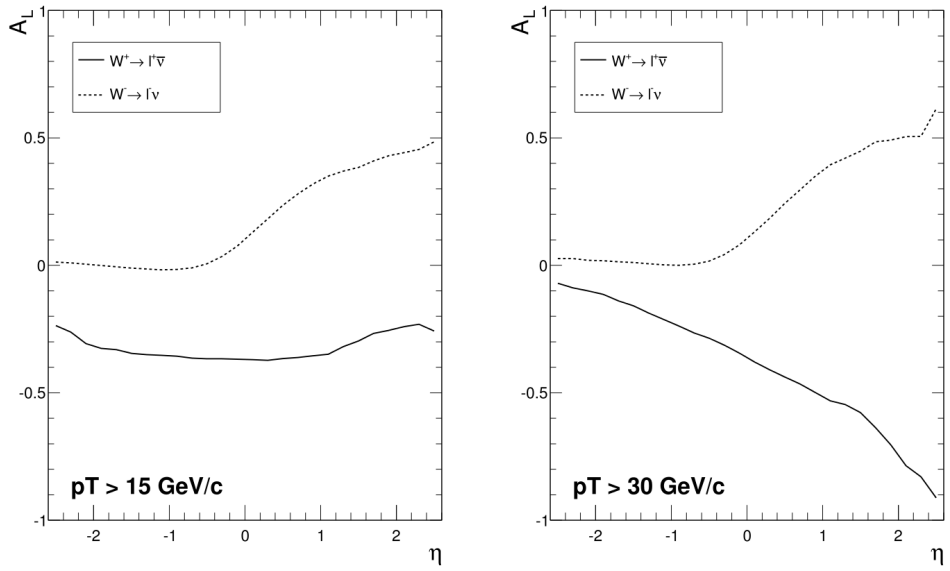



Figure 2.10: Estimation of $A_L$ of $W^{\pm} \to \ell^{\pm}$ at $\sqrt{s} = 500$ GeV with the CHE NLO generator[11]. The DSSV08 PDFs[9] were used for polarized PDFs, and the MRST2002 PDFs[8] were used for unpolarized PDFs.

hermetic detector, and there are significant chance to observe only one charged lepton from $Z$ boson.

In this study, both muons from $W^{\pm}$ and $Z$ are considered as signal, and the inclusive single spin asymmetry is measured. Figure 2.11 shows $A_L$ of $Z^{\pm} \to \ell^+\ell^-$ at $\sqrt{s} = 500$ GeV with the CHE NLO generator[11] as a function of $y_\ell$ with DSSV08 global analysis of polarized PDFs[9].

## 2.5 $A_L^{\ell\pm}$ at mid and forward rapidities

At RHIC, both the PHENIX and the STAR experiments have been measuring $A_L^{\ell\pm}$ at $\sqrt{s} = 500$ GeV in longitudinally polarized proton-proton collisions at mid-

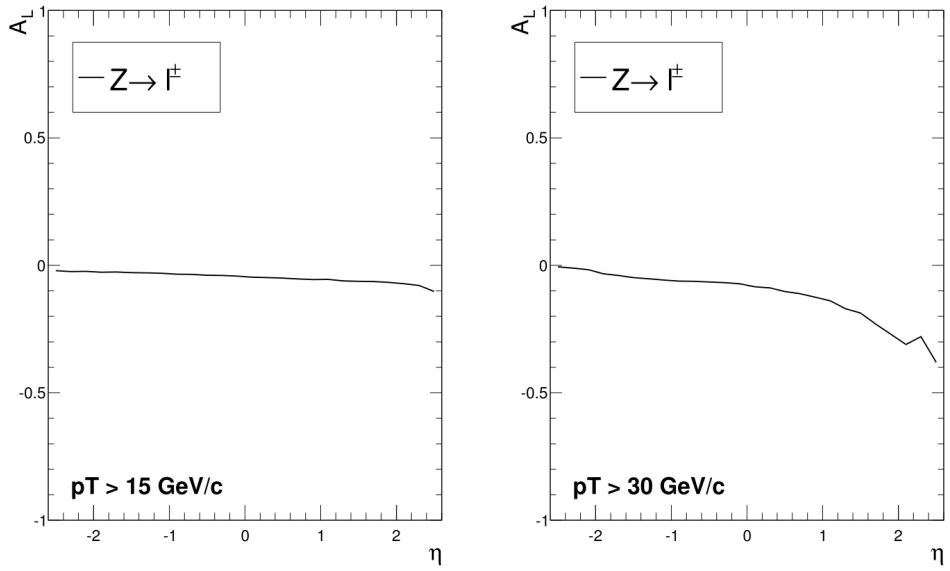



Figure 2.11: Estimation of $A_L$ of $Z \to \ell^{\pm}$ at $\sqrt{s} = 500$ GeV with the CHE NLO generator[11]. The DSSV08 PDFs[9] were used for polarized PDFs, and the MRST2002 PDFs[8] were used for unpolarized PDFs.

rapidity since 2009. In PHENIX, in the forward and backward hemispheres, the muon spectrometers have been recently upgraded and were measuring $A_L^{\mu^{\pm}}$ since 2011. Measurements from PHENIX and STAR in run 2009 have large statistical uncertainity, but the results are consistent with calculation of various global analysis of polarized PDFs. Figures 2.12 and 2.13 show results from the mid rapidity PHENIX and STAR, respectively. Both experiments are continuing to take data to improve the results. The PHENIX detector has acceptance for electrons in central and muons in forward rapidity regions. Detectors in the central arm have acceptance $|\eta| < 1.5$, whereas the forward arms have effective acceptance

of $-2.2 < \eta < -1.4$ and $1.4 < \eta < 2.4$. The PHENIX detector is not a hermetic detector and it does not have ability to measure the missing energy taken by neutrinos from $W$ decays. Also the limited acceptance may cause us to miss one of the two muons from $Z$ decays. It is not easy to separate $Z$ events from $W^{\pm}$, and both processes could produce parity-violating $A_L$. Thus we treat single muons from both $W^{\pm}$ and $Z$ bosons as signals. However the muon production cross section from $W^{\pm}$ decays dominates the signal, and the contribution of $Z$ events in the signal is only in the order of 10%. This thesis will be focusing on the techniques and results of run 2013 $W^{\pm}/Z$ measurement at the PHENIX forward spectrometers.

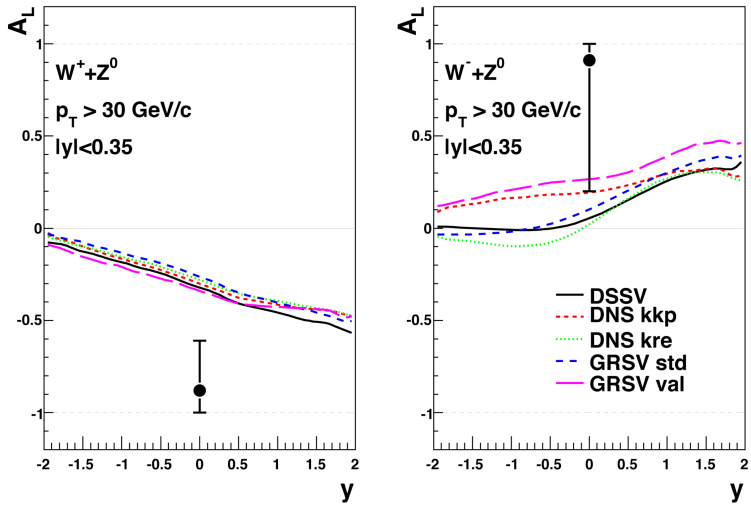



Figure 2.12: $A_L$ for $e^{\pm}$ from $W^{\pm}/Z^0$ boson decays for $|\eta| < 0.35$, $30 < p_T < 50$ GeV/$c$ from PHENIX Run 2009[45].

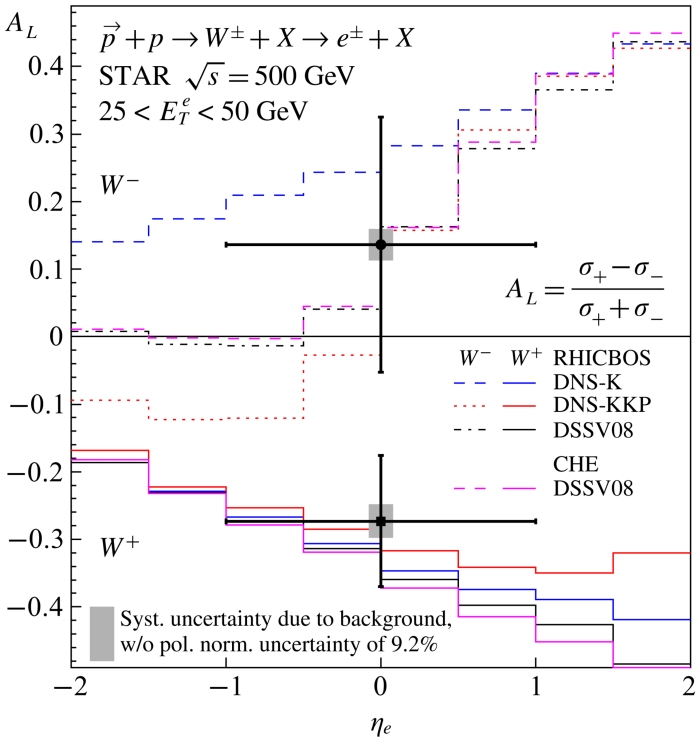



Figure 2.13: $A_L$ for $e^{\pm}$ from $W^{\pm}$ boson decays for $|\eta| < 1,\ 25 < p_T < 50$ GeV/$c$ from STAR Run 2009[46].

### 2.5.1 Measurement of $W^{\pm}/Z \to \mu^{\pm}$ at forward rapidity

**Signal distribution at the forward rapidity** As discussed in Sec. 2.5 the Jacobian peak is significant in the mid rapidity region for both $W^{\pm}$, while it is less significant in the forward/backward rapidity ranges. As shown in simulation plots in Figure 2.14, at the pseudorapidity region of $1.4 < \eta < 2.4$ the $p_T$ spectrum of muons from $W^{\pm}$ is rather continuous and the Jacobian peak barely remains only for $W^+$.

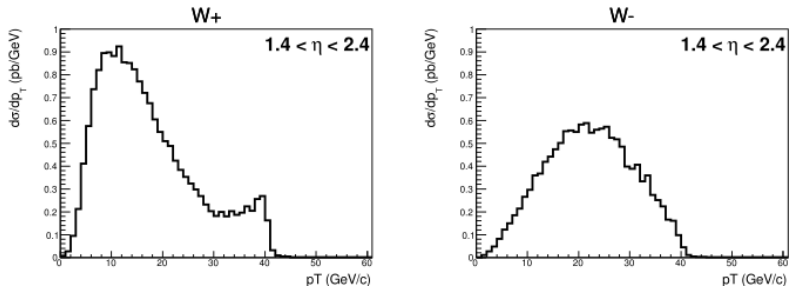



Figure 2.14: $p_T$ distribution of $\mu^{\pm}$ from $W^{\pm}$ in $1.4 < \eta < 2.4$.

**Backgrounds distribution at the forward rapidity** Apart from backgrounds from misreconstruction by detectors, the possible muon backgrounds of $W \to \mu$ signals in the forward arms of PHENIX are from

- open heavy flavors ($c,\ b \to \mu + X$),
- quarkonia $J/\psi,\ \Upsilon$ states ($J/\psi \to \mu^+\mu^-$),
- Drell-Yan ($q\bar{q} \to \gamma^* \to \mu^+\mu^-$),
- Direct photon,
- $W \to \tau \to \mu$,
- $W \to$ hadrons $\to \mu$.

Figures 2.15 and 2.16 show the simulation of these backgrounds at $1.2 < \eta < 2.4$ with PYTHIA6 event generator[87]. The majority of muon backgrounds are from open heavy flavors and quarkonia. However the $p_T$ spectra of most of the muonic backgrounds fall steeply with $p_T$ and are well suppressed above

$p_T > 20$ GeV/$c$. The high $p_T$ single muons are then considered as candidates of $W \to \mu$ events. $W \to \tau \to \mu$ could be a background which may produce finite $A_L$, but its contribution at high $p_T$ is smaller than Drell-Yan and $Z$ events.

However in actual situation, the finite momentum resolution of the detector smears the $p_T$ spectra. Then the $W \to \mu$ signals at high $p_T$ region are contaminated with backgrounds whose original momentum is lower than the reconstructed one.

In addition to the above muon backgrounds, the signal would be heavily buried in a large amount of hadronic backgrounds ($\pi^{\pm}, K^{\pm}$). Prompt hadrons decay to muons inside the detector and may be mis-reconstructed as high $p_T$ muons (also called fake high $p_T$ muons). Rejecting these hadronic backgrounds is very challenging especially in the forward arms of PHENIX (no Jacobian peak). Different techniques of identifying and reducing hadronic backgrouns in the PHENIX forward arms will be discussed in the analysis part this thesis.

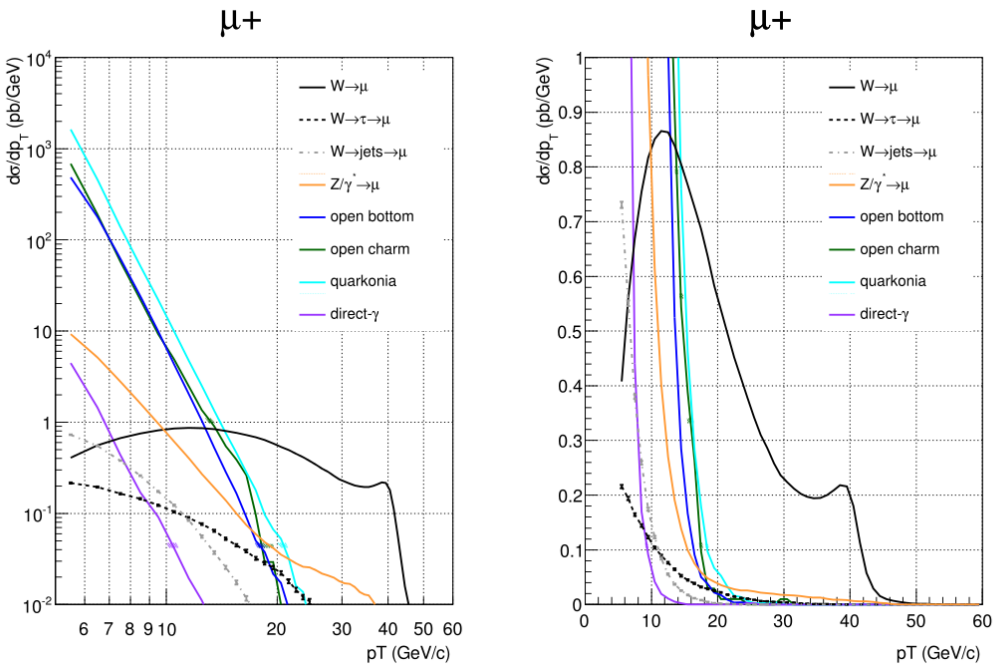



Figure 2.15: Simulated $W^+ \to \mu^+$ process and muon background processes at $1.4 < |\eta| < 2.4$ with PYTHIA.

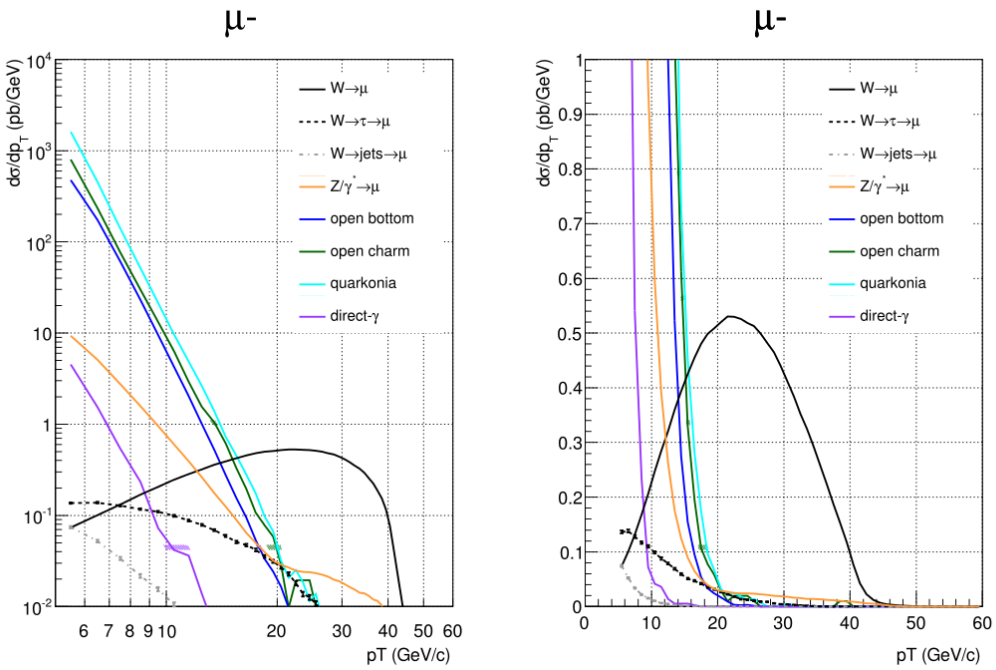



Figure 2.16: Simulated $W^- \to \mu^-$ process and muon background processes at $1.4 < |\eta| < 2.4$ with PYTHIA.

# 3 Apparatus and Data Taking

As discussed in chapter 2, measurement of single spin asymmetry in $p + p \rightarrow W^{\pm} \rightarrow \ell^{\pm}\bar{\nu}_{\ell}$ process requires polarized protons be accelerated and collide at energies high enough to probe the internal structure of protons. The Relativistic Heavy Ion Collider (RHIC) at Brookhaven National Laboratory in Long island is a unique polarized proton-proton collider suitable for such measurement. The first part of this chapter will describe the production and acceleration of polarized protons. In the second section, the RHIC collider will be introduced. In the third section the PHENIX detector system with particular attention to its forward arms will be explored. The last section will focus on the data taking mechanisms at PHENIX forward arms and the triggers used in the run 2013 polarized proton-proton collision.

## 3.1 Polarized proton at RHIC

The RHIC accelerator facility is built for the study of

- the new state of matter at very high temperature also called Quark Gluon Plasma (QGP) through collisions of heavy ions, and
- the spin structure of the proton using the collisions of polarized p + p.

RHIC is the only polarized p + p collider in the world providing a unique opportunity for studying the proton spin structure. RHIC has produced polarized p +

p collisions at the center of mass energies ($\sqrt{s}$) of 62.4, 200, 500 and 510 GeV since 2005.

### 3.1.1 Polarized beam source

The source of polarized proton beam supplied to the RHIC is called Optically-Pumped Polarized Ion Source (OPPIS)[47]. The OPPIS produces pulse of $\sim 10^{12}$ nuclearly polarized $H^-$ ion bunches of kinetic energy 35 keV in 300 $\mu$s long pulses. The $H^-$ ions extracted from OPPIS are accelerated by RFQ to 750 keV and transferred to the Linear Accelerator (LINAC), stripped of their electrons, and passed onto the Alternating Gradient Synchrotron (AGS) Booster. In the AGS Booster they are further accelerated to a beam energy of 1.5 GeV.

### 3.1.2 Accelerator complex

The polarized proton produced from OPPIS source is then delivered to the RHIC-AGS accelerator complex. In Figure 3.1 the components related with acceleration and collision of polarized proton beams are briefly described.

**LINAC** The LINAC is a 200 MHz linear accelerator and it accelerates $H^-$ ions to 200 MeV and strips the electrons off to inject proton beams into the Booster Synchrotron.

**Booster Synchrotron** The Booster Synchrotron accepts the proton beam from the LINAC of the 300 $\mu$s pulse into a single bunch, and it accelerates the proton bunch to 2.35 GeV and injects them into the AGS.

**Alternating Gradient Synchrotron (AGS)** The AGS is a pioneering accelerator operating since 1960, which employed the strong focusing principle with the concept of alternating gradient focusing. AGS accelerates polarized protons to 24.3 GeV and injects them to the RHIC.

**Relativistic Heavy Ion Collider (RHIC)** The RHIC ring is a 3.8 km circumference double-ring superconducting collider which accelerates proton beams up to 255 GeV to achieve the center of mass energy ($\sqrt{s}$) ranging from 62.4 GeV to 510 GeV. Each of two independent rings can fill maximally 120 proton bunches, the bunch crossing time period is 106 ns. As a matter of convention, the clockwise beam is named as "Blue beam", and the counterclockwise beam is named as "Yellow beam". In year 2013 runs, the RHIC achieved about $165 \times 10^9$ ions per bunch in proton-proton collisions, and the peak and average luminosity was $1.45 \times 10^{32}$ cm$^{-2}$s$^{-1}$ and $0.90 \times 10^{32}$ cm$^{-2}$s$^{-1}$, respectively. The typical lifetime of one fill is about 8 hours. The beams are steered to cross at four different collision points around the ring, where p + p interactions occur. Four Different experiments have operated at RHIC: PHENIX[48], STAR[49], PHOBOS[50], and BRAHMS[51], where the latter two experiments have concluded their experimen-

tal research phases. For each collision point, the two oppositely coming beams are guided by the DX dipole magnets so that they make head-on collisions.

The spin direction at the moment of the collision is controlled by the spin rotators which are set both outside the DX magnets with respect to the collision point. Longitudinal (spin oriented along with the beam axis), vertical (spin oriented perpendicular with beam axis), and radial (spin oriented along with radial axis) collisions are possible independently for each collision point. For each bunch of either beam the nominal direction of the polarization can be either vertical-up (+) or vertical-down (−). The pattern of the spin direction is selected so that all possible four pattern collisions, i.e., $\{++, +-, -+, --\}$ take place almost equally. Several patterns are provided by the accelerator group and the pattern is usually different fill by fill. The last 10 packets out of 120 (#110 - #119) are reserved for utility time ("abort gap"), such as laser calibration of the detector, and each beam has two bunch-length blanks ("keys") at different bunch crossings (#38 and #39 for the Blue beam, #78 and #79 for the Yellow beam) to crosscheck the pattern. Controlling the spin of proton beams are described in the next subsection.

### 3.1.3 Maintain and measure the polarization at RHIC

#### Siberian Snakes and Spin Rotators

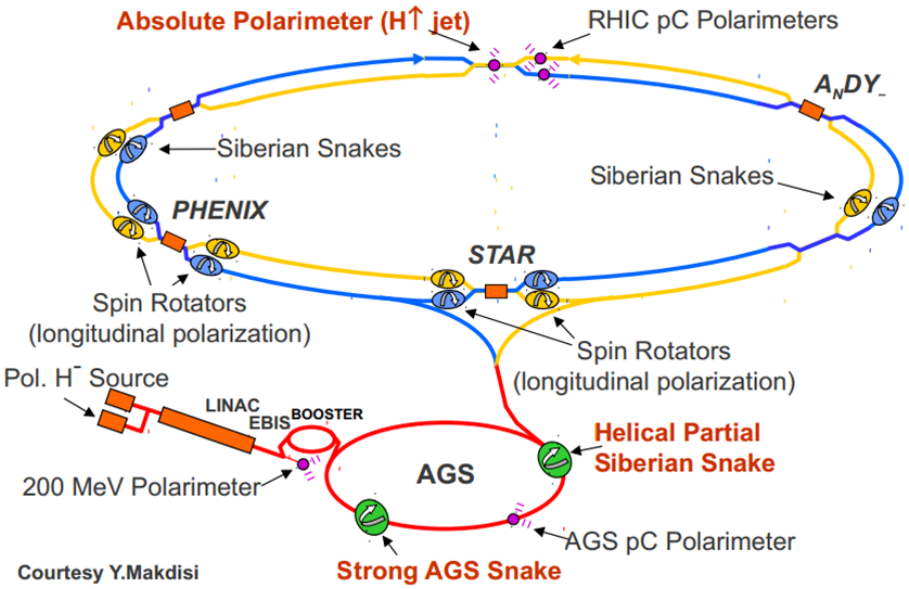



Figure 3.1: RHIC accelerator complex.

**Siberian Snakes:** Maintaining the polarization during acceleration and collision could be a difficult task because of depolarization. The polarization of proton beams may be lost with time during a fill which may take upto 8 hours. The main reasons for depolarization are classified into two: one is due to imperfection of dipole and quadrupole magnetic field caused by mis-alignment, *etc.*; the other is due to the existence of intrinsic spin resonance caused by spin precession around the radial field components in the focusing magnets. Both of them can be prevented by inserting instruments named "Siberian snakes"[56, 57]. A Siberian Snake consists of helical dipoles, in which the direction of the proton spin is rotated by 180° in the full Snake or at a certain degree in the partial Snake. By using Siberian Snakes, the effect of depolarizations in the beam path is cancelled

out between one and the next circulation of the beam. The AGS employs a 9° partial Snake, and the RHIC employs two full Snakes.

**Spin Rotator:** The spin rotator is a similar instrument as the Siberian Snake, which consists of four helical dipoles, but the helicity of the two of them is opposite to the others. By tuning the current weaker than the Siberian Snake, it is possible to rotate the direction of spin of proton beams.

**Polarimetry:** The polarization of either beam is measured at different points in RHIC by three different types of polarimeters. All these polarimeters are designed to measure the transverse spin asymmetry The transverse spin asymmetry $A_N$ and its raw asymmetry $\varepsilon_N$ are defined as follows

$$\varepsilon_N \equiv P A_N \equiv \frac{N_L - N_R}{N_L + N_R} \tag{3.1}$$

where for each event $P$ is the polarization of either the beam or the target, and $N_{L(R)}$ is the number of events detected at the left(right)-side detector with respect to the beam direction.

**Coulomb-Nuclear Interference (CNI) polarimeter:** The Coulomb-Nuclear Interference (CNI) polarimeter uses thin carbon ribbons to measure the polarization profile of the beam[59]. The CNI polarimeter gives the relative polarization precisely, however, the absolute polarization is not available. It measures the

transverse spin asymmetry of recoil carbons scattered about 90° with respect to the beam direction in $p^{\Uparrow} + C \to p + C$. Coulomb-nuclear interference elastic scattering by inserting horizontal and vertical thin carbon ribbons into the beam path. The recoil carbons are detected with six silicon detectors surrounding the beam path. The width of the ribbon is 10 $\mu$m, thus the CNI polarimeter is possible to scan the polarization profile of the beam. Thanks to the large cross section of proton-carbon elastic scattering, the CNI polarimeter collects about $4 \times 10^6$ recoil carbons per one scanning, which takes time about one minute. Consequently two or three times of polarization measurements are possible per fill, which are used to monitor the long-term polarization decrease during the fill. Since the true transverse asymmetry $A_N$ for proton-carbon elastic scattering is not known, the CNI polarimeter measures polarization relatively.

**Hydrogen jet polarimeter:** The Hydrogen Jet (H-jet) polarimeter provides an independent measurement of the absolute polarization of the beam with the polarized hydrogen gas jet[60, 61]. The H-jet polarimeter is used to calibrate the CNI polarimeter. It uses a polarized hydrogen gas jet stream as a target. The direction of the polarization of the gas is vertical and the direction is flipped to opposite in every 10 minutes. The event rate of H-jet polarimetry is about 5 Hz, and the density of the hydrogen gas is not significant enough to affect to the physics measurement at PHENIX and STAR. Thus the H-jet measurement is

continuously taking during the fill. The absolute polarization of the hydrogen jets is absolutely measured with a Breit-Rabi polarimeter. The elastic scattering of the proton beam and the proton target is measured with silicon detectors similar to the CNI polarimeter. We can measure the raw transverse asymmetry for both the beam and the target by averaging the polarization of the other hand, thus we obtain the following relation.

$$A_N = \varepsilon_N^{\text{beam}}/P_{\text{beam}} = \varepsilon_N^{\text{target}}/P_{\text{target}} \quad . \tag{3.2}$$

By using the polarization value of the jet target measured with the Breit-Rabi polarimeter, we obtain the absolute polarization of the beam by rearranging the terms as

$$P_{\text{beam}} = \frac{\varepsilon_N^{\text{beam}}}{\varepsilon_N^{\text{target}}}.P_{\text{target}} \quad . \tag{3.3}$$

**PHENIX local polarimeter:** The PHENIX uses the Zero Degree Calorimeter (ZDC) (which will be introduced in the next paragraph and in Sec. 3.2.2) as its local polarimeter. For longitudinally polarized collisions, we need to rotate the spin of the beam from the nominal vertical orientation to the longitudinal orientation by the Spin rotators described in Sec. 3.1.3. In the vertically polarized collision case, local polarimeter is used to validate the polarization value obtained in the CNI and H-jet polarimeters. Where as, in the longitudinally polarized collision case, local polarimeter is used to validate if the spin direction is appropriately rotated by the spin rotator.

ZDCs are small transverse area hadron calorimeters located downstream of the DX dipole magnets in PHENIX. ZDC's will be described in detail in Sec. 3.2.2. These detectors are located between Blue and Yellow beam rings next to the DX magnets as shown in Figure 3.2, and the distance from the collision point of the PHENIX detector is about 18 m. Here all charged particles are deflected by the DX magnet, and only neutral particles inject to ZDCs. ZDCs mainly detect neutrons produced by collisions. The neutron production in proton-proton collision has a transverse single spin asymmetry of $A_N \sim 10$ %, but it should not have longitudinal single spin asymmetry, since the longitudinal single spin asymmetry is parity-violating. Thus we can measure the residual transverse polarization with ZDCs. For the longitudinally polarized collisions, the local polarimeter plays important role in measuring the remaining transverse polarization of the beam which could be a source of systematic uncertainties of the spin asymmetry measurement.

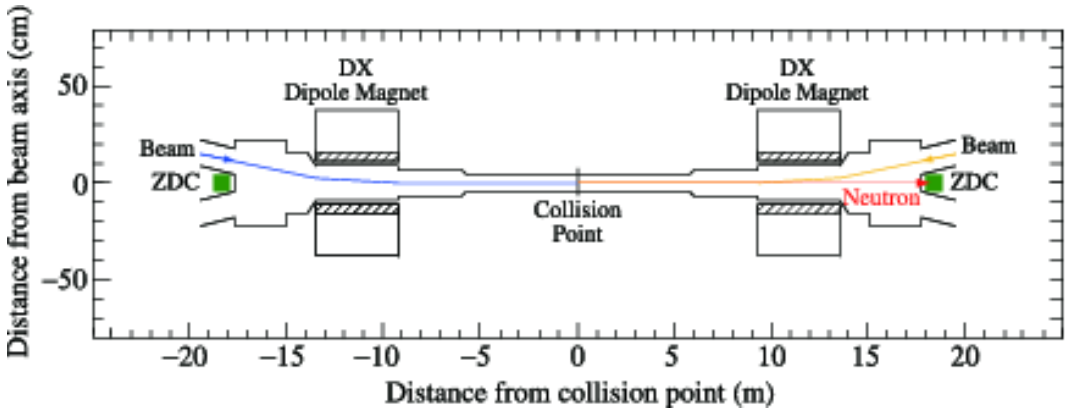



Figure 3.2: Geometric location of the Local polarimeter (ZDC,SMD) of the PHENIX detector.

## 3.2 The PHENIX detector

**Overview** The PHENIX is a large-scale multi-purpose detector system. It is located at one of four collision points of the RHIC called "8 o'clock". It is composed of four major spectrometers as well as complementing detectors. The four spectrometers cover different rapidity and azimuthal angle $\phi$ ranges. Two spectrometers which cover backward and forward rapidity regions of about $-2.2 < \eta < 1.2$ (North) and $1.2 < \eta < 2.4$ (South) respectively, are called Muon Arms. Muon Arms are specialized to measure muons. The other two spectrometers around the beam line are called Central Arms (East and West). They cover $2x(\pi/2)$ in azimuthal angle $\phi$ in the rapidity region of $|\eta| < 0.35$. The Central Arms are specialized to measure electrons, photons and hadrons with particle identification detectors. In addition to these large spectrometers, the PHENIX has recently installed the Muon Piston Calorimeters (MPC) which cover forward rapidity region of $3.1 < |\eta| < 3.7$.

**PHENIX coordinate system and conventions** Figure 3.4 shows the layout of the PHENIX Cartesian coordinate system. The origin of the global coordinate system is set at the nominal collision point at 8 o'clock of the RHIC. The $z$-axis is taken along the beam axis in clockwise, and its direction is clockwise seen from above. The beam pipe is made of Beryllium, whose radius and thickness are 20 mm and 500 $\mu$m. The $y$-axis perpendicular from bottom to top, and the $x$-axis

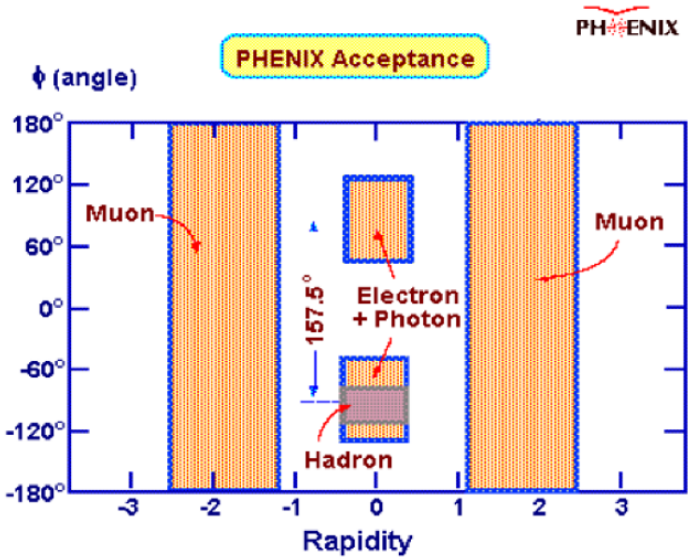



Figure 3.3: Pseudorapidity($\eta$) and azimuthal angle ($\phi$) coverage for the PHENIX detector subsystems.

is horizontal and it directs to the outside of the RHIC ring so that the resulting coordinate system is right-handed. The $-z$ direction is called "South" side and the $+z$ direction is called "North", the $+x$ direction is called "West" and the $-x$ direction is called "East", named after the geographical direction. We call a Muon Arm in the North (South) side "North (South) Arm". Similarly, a Central Arm in the East (West) side is called "East (West) carriage". The clockwise beam coming from $-z$ (South) to $+z$ (North) is called "Blue beam" and the counterclockwise beam from $+z$ (North) to $-z$ (South) is called "Yellow beam". The radial distance $r$ from the beam axis is defined as $\sqrt{x^2+y^2}$. The polar angle $\theta$ of a vector is defined as the angle between the positive $z$-axis and the vector. The azimuthal angle $\phi$ of a vector is defined as the angle between the positive $x$-axis and the

vector projected to the $xy$-plane. The pseudorapidity $\eta$ is defined as

$$\eta = -\ln[\tan(\theta/2)]. \tag{3.4}$$

In the longitudinal spin asymmetry calculation the polar angle $\theta$ is defined between the spin orientation of the polarized proton and the beam direction vector. Thus the definition of the polar angle changes which of two beams we take as the polarized beam. For the Blue beam case the definition of polar angle is the same as the PHENIX coordinate system (forward is $+z$ and backward is $-z$). For the Yellow beam case (forward is $-z$ and backward is $+z$), we measure the polar angle from the direction of the beam ($-z$). As a result of this convention the sign of $\eta$ becomes opposite to that of Blue beam.

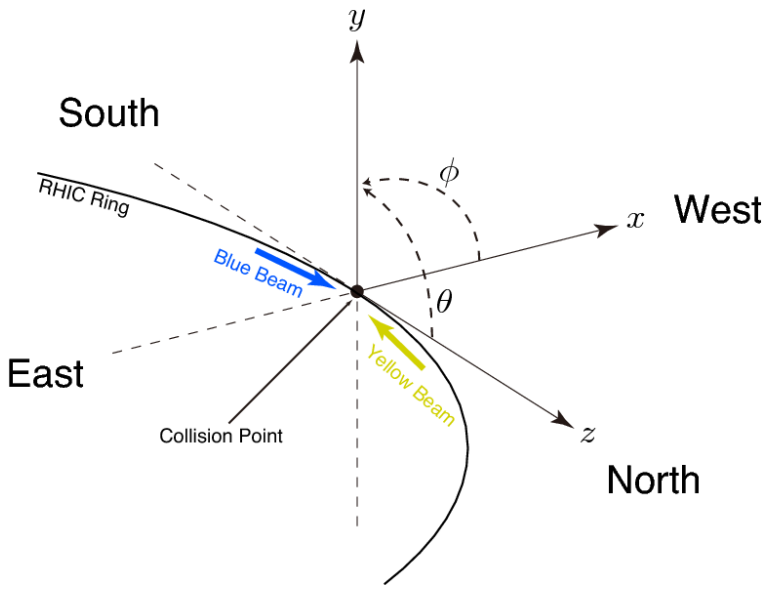



Figure 3.4: Definition of the global coordinate system used in the PHENIX experiment.

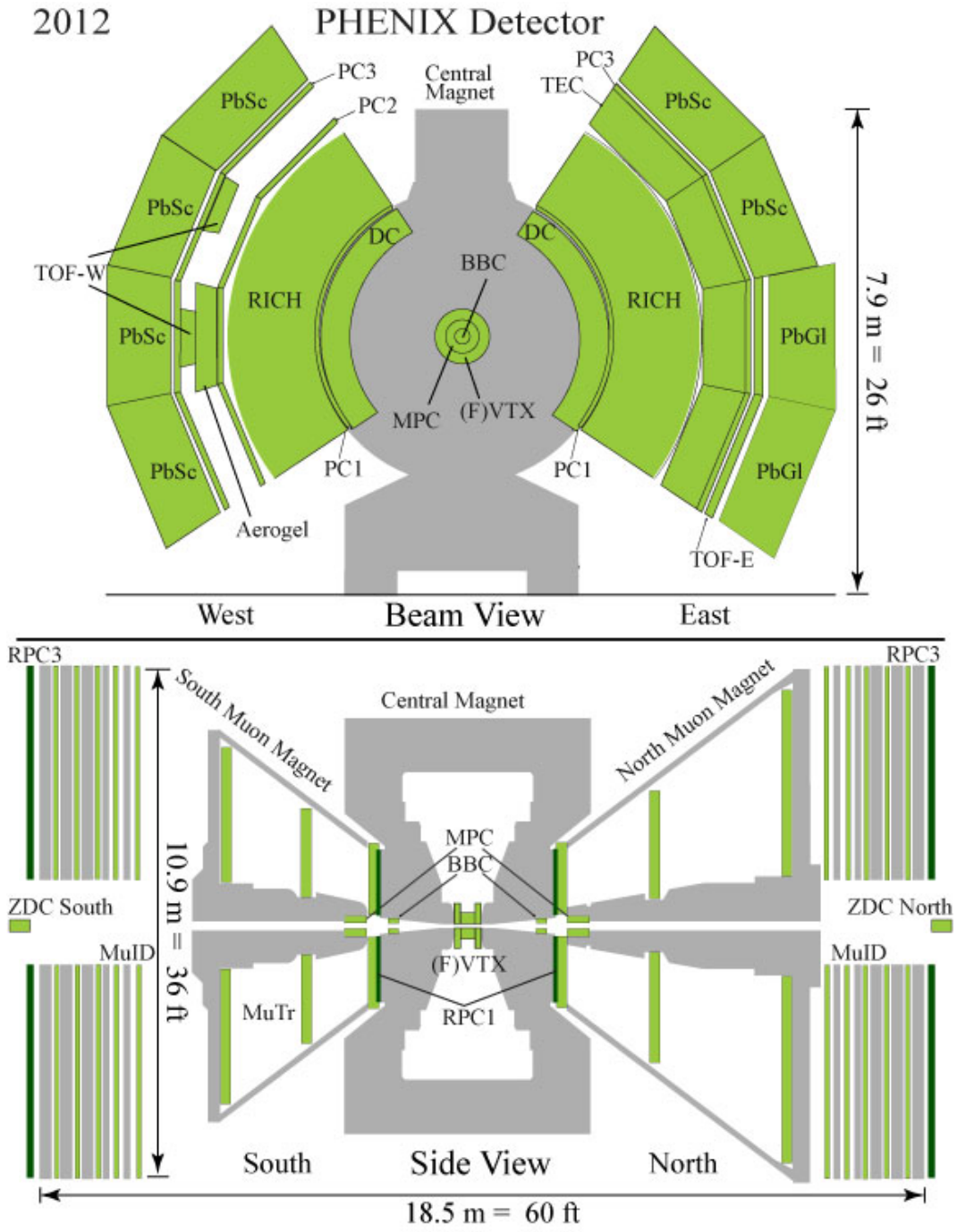



Figure 3.5: Detector subsystems of the PHENIX detector in year 2012 run setup. Top Plot: A side view featuring Muon Arm detectors and forward detectors. Bottom Plot: A beam view featuring Central Arm detectors.

### 3.2.1 PHENIX magnets and hadron absorber

**PHENIX magnets** The three magnets, the Central Magnet (CM), North Muon Magnet (MMN) and South Muon Magnet (MMS) (Figure 3.6) form the PHENIX magnet system.

The Central Magnet creates the magnetic field parallel to the beam axis ($z$-direction) by two pairs of concentric coils, as a result, charged particles bend in the azimuthal direction. As the Central Arms have PID detectors (RICH, TOF, Aerogel), it is desirable to minimize the amount of material between the collision point and the Central Arms. The integrated magnetic field of the Central Magnet is 0.78 T $\cdot$ m, while the field strength at the position of the RICH is about 200 Gauss. The Central Magnet also works as a hadron absorbers for forward rapidity.

The Muon Magnets produce a radial magnetic field. Each magnet has two solenoidal coils in the tapered core of the Muon Arm called the Muon Piston to produce the radial field. The field flux is saturated in the Muon Piston and it diverges radially from the Muon Piston to the eight-frustum yoke called *lamp-shade*, then returns via a 30 cm thick endplate. The integrated magnetic field at $\theta = 15^\circ$ is $\int B \cdot dl = 0.72$ T $\cdot$ m. Table 3.1 summarizes the key parameters of the magnets.

Table 3.1: The key parameters of the PHENIX Central Magnet and the Muon Magnets.

| **parameters** | **Central Magnet** | **Muon Magnets** |
|---|---|---|
| Type | two pairs of concentric coils | solenoidal coils |
| Field | solenoidal | radial |
| Mass | 500 tons | 400 tons/arm |
| Height | 9 m | 10 m |
| Rapidity coverage | $\|\eta\| < 0.35$ | $1.1 < \|\eta\| < 2.4$ |
| Polar angle coverage (°) | $70 < \theta < 110$ | $10 < \theta < 37$ |
| Integrated field $\int B \cdot dl$ | 0.78 T · m | 0.72 T · m at $\theta = 15°$ |

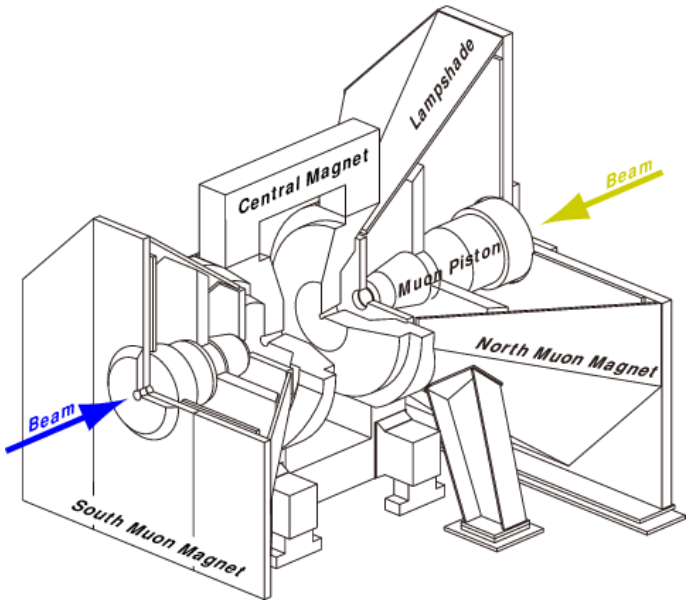



Figure 3.6: The PHENIX Central Arm and Muon Arm magnets.

**Hadron absorbers** Hadrons ($\pi$ or $K$) decaying to muon may produce a fake high-$p_T$ track and are the major backgrounds in $W$ measurement. To reduce these hadrons two groups of hadron absorbrs are installed in PHENIX forward arms. Table 3.2 summarizes the specification of the hadron absorbers.

The first group is located before Muon Trackers (pre-Mutr absorbers). The Central Magnet which is made of 60 cm steel also has a role of hadron absorber. At the inner surface of the Central Magnet is another 20 cm-thick copper nose cone. In addition to these existing pre-MuTr absorbers, new absorbers were installed at the rear surface of the Central Magnet for the measurement of $W^{\pm} \rightarrow \mu^{\pm}$ measurement (Figure 3.7). The new hadron absorber is the 35 cm-thick plates of 24 tons. The plates are made of Cr (24 - 26 %) and Ni (19 - 22 %) enriched stainless steel. By adding the new absorber, the pre-MuTr absorber presents a total thickness (interms of hadronic interaction length) of $7.1\lambda_I/\cos\theta$, which corresponds to hadron reduction of $\sim 10^{-3}$.

The second group of hadron absorbers are located behind the Muon Tracker, Mutr shown in Figure 3.5. One of them is Muon Magnet Yoke which is part of the Muon Magnet and the others are Muon Identifier, MuID (Section 3.2.3) layers which are part of the MuID shown in Figure 3.5. The thickness of the Muon Magnet Yoke (backplane) is 20 cm for the South Arm and 30 cm for the North Arm. The MuID has five steel walls in each arm. The total thickness of the MuID steel walls is 80 cm. The total interaction length from the origin to the rear of the MuID (at the

location of the RPC3) is $13.0\lambda_I(13.4\lambda_I)$ for the South (North) Arm.

Table 3.2: Parameters of hadron absorbers in the PHENIX detector.

| **Location** | **Material** | **South Thickness** (cm) | **North Thickness** (cm) | $\lambda_\mathbf{I}/\cos\theta$ |
|---|---|---|---|---|
| Nose cone | Copper | 20 | 20 | 1.8 |
| Central Magnet | Steel | 60 | 60 | 3.1 |
| New absorber | SS310 | 35 | 35 | 2.2 |
| Sum of pre-MuTr | - | 115 | 115 | 7.1 |
| Muon Magnet Yoke | Steel | 20 | 30 | S:1.1, N:1.5 |
| MuID 1st Layer | Steel | 10 | 10 | 0.6 |
| MuID 2nd Layer | Steel | 10 | 10 | 0.6 |
| MuID 3rd Layer | Steel | 20 | 20 | 1.2 |
| MuID 4th Layer | Steel | 20 | 20 | 1.2 |
| MuID 5th Layer | Steel | 20 | 20 | 1.2 |
| Total | - | 215 | 225 | S:13.0, N:13.4 |

### 3.2.2 Global detectors, BBC and ZDC

In order to characterize the nature of an event after collision, global detectors are employed. The Beam Beam Counters (BBC) and the Zero Degree Calorime-

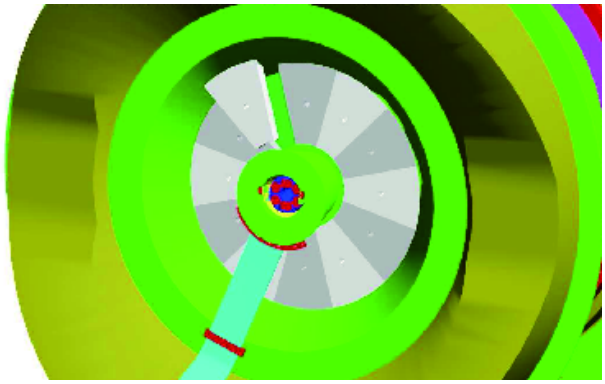


Figure 3.7: A layout of extended hadron absorbers.

ters (ZDC) are categorized as the global detectors in the meaning that those are commonly used by all measurements in PHENIX.

**Beam Beam Counters (BBC)** [75]

There are two modules of BBC mounted on south and north arms of PHENIX. The BBCs cover forward rapidity region of $3.1 < |\eta| < 3.9$ and full azimuthal coverage. Each of them consists of 64 quartz Cherenkov counters mounted on Photo Multiplier Tubes (PMT). The PMTs surround the beam pipe in three layers (Figure 3.9). The BBC array has an inner diameter of 10 cm and outer diameter 30 cm. The distance of the quartz crystals from the origin is 144 cm for both arm modules. Optical fibers branched from the two laser sources are mounted on quartz crystals to calibrate the gain and detection timing. The vertex calculation is performed both offline and online. The online vertex calculation is used to issue the minimum bias triggers which limit the vertex range to e.g. $|z_{\rm vtx}| < 30$ cm.

BBC is used for (a) triggering, (b) to monitor the luminosity (c) to determine event vertex along beam direction and (d) for timing calibrating used in the time of flight calculations. The spatial resolution of BBC $z_{vtx}$ vertex measurement is about 5 cm for online measurements and 2 cm for offline measurements.

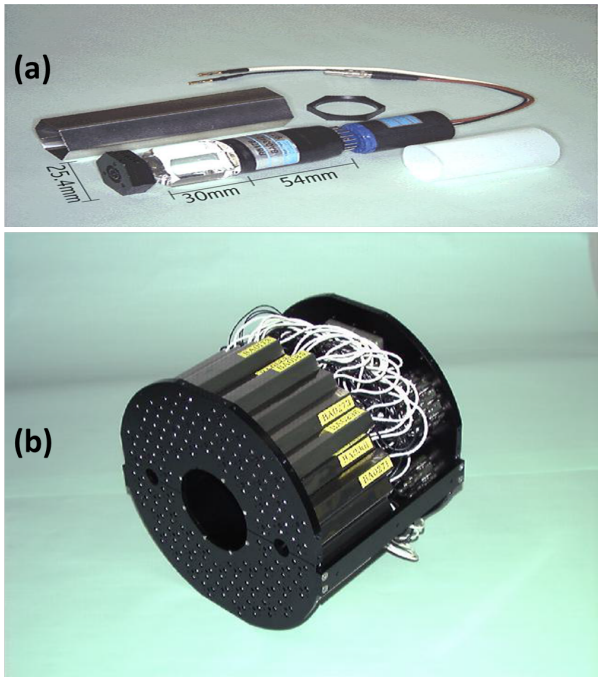



Figure 3.8: (a) Single BBC consisting of Photo Multiplier Tube (PMT) on a 3 cm quartz radiator and (b) BBC array comprising of 64 units.

**Zero Degree Calorimeter (ZDC)** [76]

The Zero Degree Calorimeter (ZDC) is hadronic calorimeter used for forward neutron tagging at PHENIX. a tungsten neutral hadron calorimeter located at the very forward region of $\theta < 2.8$ mrad i.e. $\sim 0^{\circ}$ behind the DX magnet. One set of the ZDC is placed at each the South side and the North side. The ZDCs

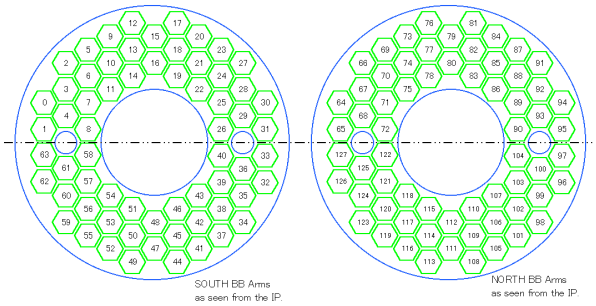



Figure 3.9: Arrangement of PMTs in the BBC. The blue circle blanks are the positions of laser sources.

are located at $\pm 18$ m from the nominal interaction center, the furthest detector of the PHENIX. Each ZDC covers a cone of 2 mrad with pseudo-rapidity range $\eta \geq 6$. A ZDC consists of the three identical calorimeter modules and the Shower Maximum Detector. The calorimeter module is a sampling hadronic calorimeter made of tungsten plates and optical fibers. The hadronic interaction length of the 27 tungsten plates in one module is $2.0\lambda_I$.

Most charged particles are deflected by the DX magnet, but neutrons and photons directly inject into the ZDC. The fibers collect Cherenkov lights created by hadronic showers. The fibers are coupled to a 2 inch standard PMT. The relative angle between the tungsten plates and neutron fluxes are set to 45°, which maximizes the light yield to achieve the best energy resolution. The energy resolution is $20 \cdot \sqrt{100 \text{ GeV}/E}$ %. Three modules are arrayed in beam direction, and mostly photons deposit all energy only on the first module, and neutrons deposit certain fraction of the energy on the second or the third modules. Between the first and

the second module there is a 5 mm-thick X and Y orientation hodoscope called Shower Maximum Detector (SMD) inserted.

The ZDC can also provide local level-1 triggers requiring hits in both the South and North side detectors. It can also measure the collision vertex roughly by measuring time-of-flights as the BBC does. The spatial resolution of ZDC vertex measurement is about 30 cm for online measurements and 10 cm for offline measurements.

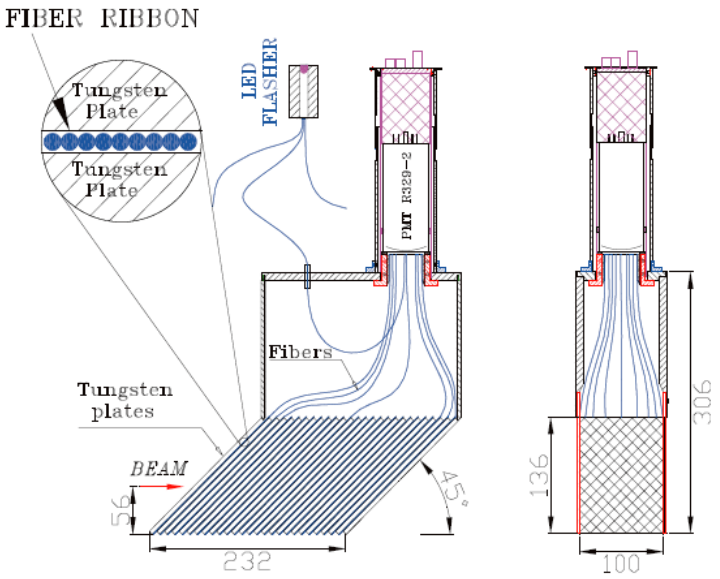



Figure 3.10: Drawing of a ZDC module. Dimensions are in mm.

### 3.2.3 Muon Tracker (MuTr)[66]

The Muon Tracker (MuTr) system, shown in Figure 3.5, is located at the forward (North) and backward (South) regions of PHENIX. Each muon arm consists of

MuTr and Muon Identifier (MuID). MuTr is the main tracking detector of the Muon Arms. Each MuTr arm is composed of three stations of cathode-strip read-out tracking chambers built inside the "lampshade" of the Muon Magnets. The three stations are called Station-1,2,3 counting from inner to outer. The South MuTr covers 12.5° - 35° ($-2.2 < \eta < -1.1$), and the North MuTr covers 10° - 35° ($1.1 < \eta < 2.4$) of the polar angle. The $z$-position of the three stations are distant from the origin by $1.80, 3.00, 4.60$ m for the South Arm and $1.80, 3.47, 6.12$ m for the North Arm, respectively.

The first station consists of four identical segments called "quadrants", while the second and third stations consist of eight segments called "octants". A layer of a station is made of cathode strip chamber and it is called "gap". The distance between the two cathode planes of the gap is 6.4 mm. The number of layers of the Station-1,2,3 is 3, 3, 2, respectively. Summary of key parameters related to each arm and station are given in Table 3.3. For the mechanical construction, honeycomb technology was used for stations 1 and 3 and thin foil technology for station 2. Each station used a specific technology to produce a cathode pattern to an accuracy of better than 25 microns.

### 3.2.4 Muon Identifier (MuID)[66]

The Muon Identifier (MuID) system comprises walls of steel absorber interleaved with five layers of plastic proportional tubes of the Iarocci type in each of the

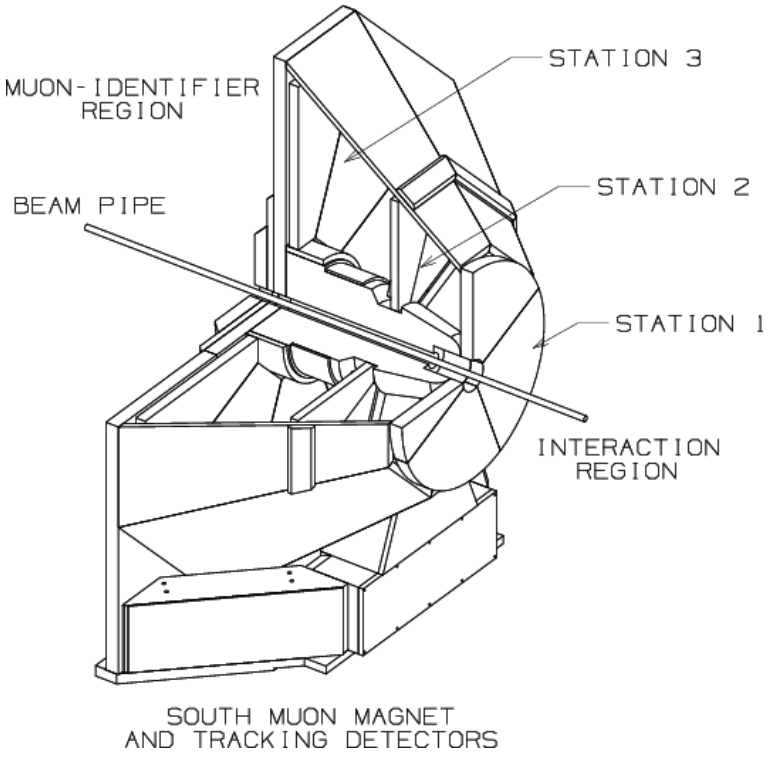



Figure 3.11: The South Muon ARM tracking spectrometer. Muons from the intersection region, to the right, intercept the station 1, 2 and 3 detectors

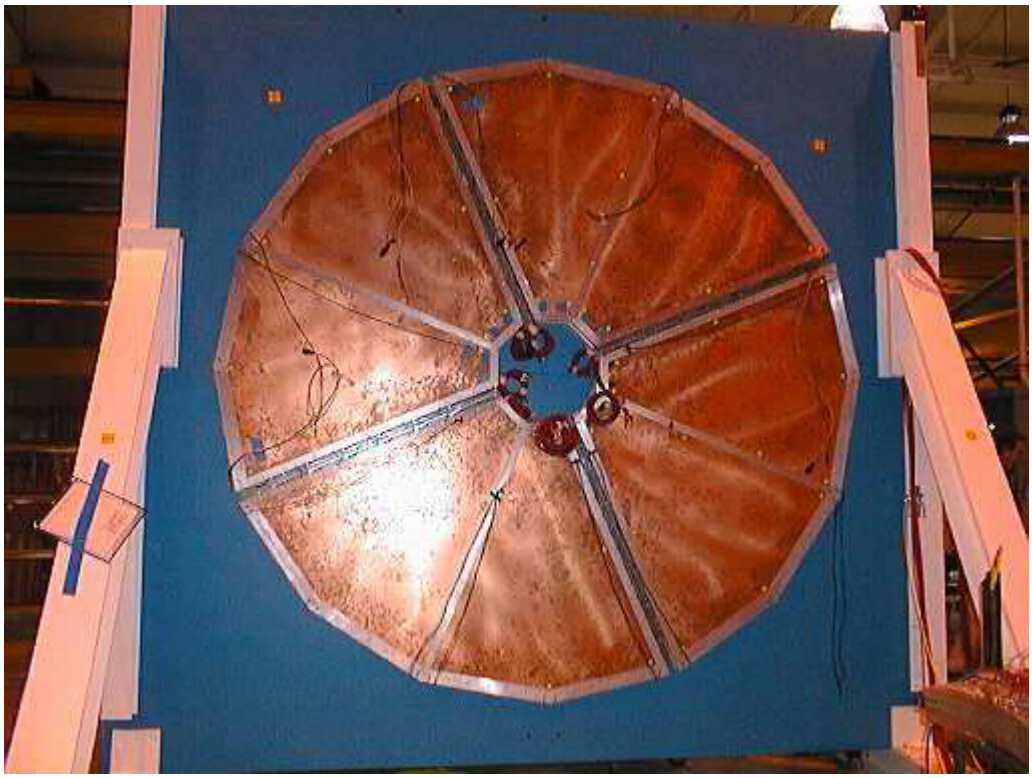


Figure 3.12: Station 1 is built in four segments called quadrants but is electrically divided into octants to match the octants of station 2 and station 3.

Table 3.3: Key parameters related to the three stations of the MuTr.

| **Parameter** | **South (St. 1/2/3)** | **North (St.1/2/3)** |
|---|---|---|
| $\|z\|(m)$ | 1.80 / 3.00 / 4.60 | 1.80 / 3.47 / 6.12 |
| Radius (m) | 1.26 / 2.10 / 3.22 | 1.26 / 2.43 / 4.29 |
| Number of gaps | 3 / 3 / 2 | 3 / 3 / 2 |
| Number of cathode planes | 6 / 6 / 4 | 6 / 6 / 4 |
| Number of RO | | |
| channels/octant/plane | 96 / 160 / 256 | 96 / 192 / 320 |
| polar angle coverage (°) | 12.5° - 35° | 10° - 35° |
| rapidity coverage | $-2.2 < \eta < -1.1$ | $1.1 < \eta < 2.4$ |

two muon arms. The Muon Identifier (MuID) is a trigger detector of the Muon Arm as well it provides the seed of the offline tracking. The purpose of MuID is for muon/hadron separation. The detector layer between steel absorbers is also called as "gap". The width and the height of the gap is about 15 m and 10 m, respectively. Thickness of each steel absorber wall with the corresponding radiation length is given in Table 3.2. The detector is composed of a aluminum-frame wire chamber called Iarocci streamer tube (Figure 3.13).

On each gap there are 4 large panels and 2 small panels as shown in Figure 3.14, and each panel has horizontal and vertical arrays of two-packs. In a panel, Iarocci tubes with either 2.5 or 5.6m length and 8.4cm width run both horizontally and

vertically. An Iarocci tube in the MuID is an array of nine $9 \times 9$ mm wire cells with either 2.5 or 5.6m length, and each cell has an anode wire surrounded by a square cathode. The gas is the mixture of 92 % $CO_2$ and 8 % isobutane. In both arms there are 6340 tubes (3170 channels per Arm). The applied high voltage is 4300 - 4500 V, which achieves the multiplication of $\sim 2 \times 10^4$. Two units of Iarocci tube arrays are bundled with shifting by a half cell on each other, and this becomes the unit of the readout of one channel called "two-pack".

**MuID FEE** Differential signals are driven over long ( 15 m) twisted-pair cables to crates of processing electronics. Signal conditioning (digitization and variable delay), buffering (LVL1 and DCM latency) and communication (LVL1-trigger) occur on a series of 96-channel Readout Cards (ROCs). Each crate contains 20 ROCs and a Front-End Module (FEM) card that serve as the interface to PHENIX (serial control, timing controls, and data collection). There are two MuID FEE crates per Muon Arm.[67]

### 3.2.5 PHENIX muon arm upgrade

The PHENIX muon arms have recently upgraded as shown in Figure 3.2.5 to accomplish the $W$ measurement[68]. One of the greatest difficulties in measuring $W$ bosons is that the trigger rate at RHIC design luminosities will be too high to record every event with the existing PHENIX trigger system by the MuID. The

Table 3.4: Key parameters of MuID.

| **Parameter** | **Design** |
|---|---|
| Width | 13 m |
| Height | 10 m |
| Gaps | 5 |
| Panels per gap | 4 (large) + 2 (small) |
| Segmentation | 8.35 cm (X,Y) |
| Gas constituent | $CO_2$ (92 %) + isobutane (8 %) |
| Operational voltage | 4300 - 4500 V |
| Multiplication | $\sim 2 \times 10^4$ |
| Drift time | $\sim 60$ ns |
| rapidity coverage | South:$-2.25 < \eta < -1.15$, North:$1.15 < \eta < 2.44$ |
| $\Delta\phi$ coverage | $360^\circ$ |

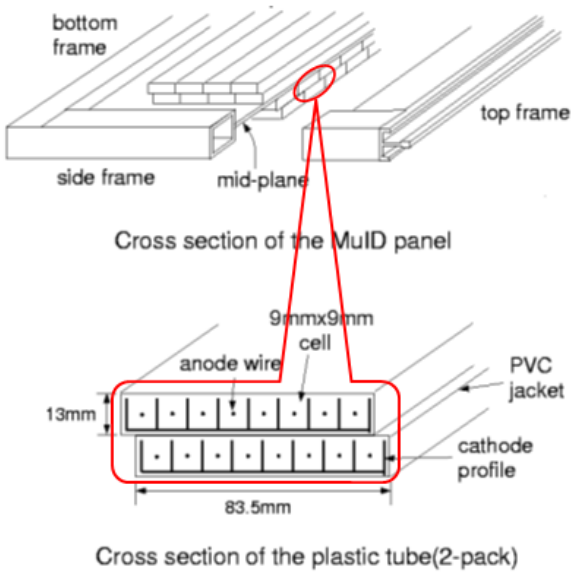



Figure 3.13: A drawing of Iarocci streamer tubes in the MuID.

proton-proton collision rate is expected to become higher than 10 MHz at the full luminosity, while the DAQ bandwidth assigned to the muon arms is limited to $\sim 2$ kHz. The MuID-based trigger has a rejection power of only $\sim 100$, so for efficient acquisition of W-candidates, a new trigger was developed for the $W$ detection, which must provide better rejection of at least 5000.[68] The $W$ trigger consists of two components, additional front-end electronics for the MuTr to process fast trigger signals (MuTRG-FEE) and Resistive Plate Chamber (RPC) which provide momentum-sensitive position information with good time resolution.

The other upgrade is installation of a new absorber. Dominant background in the W extraction is estimated to be fake high-momentum tracks caused by hadron decays to a muon in the MuTr volume. The new absorber of 35 cm-thick stainless

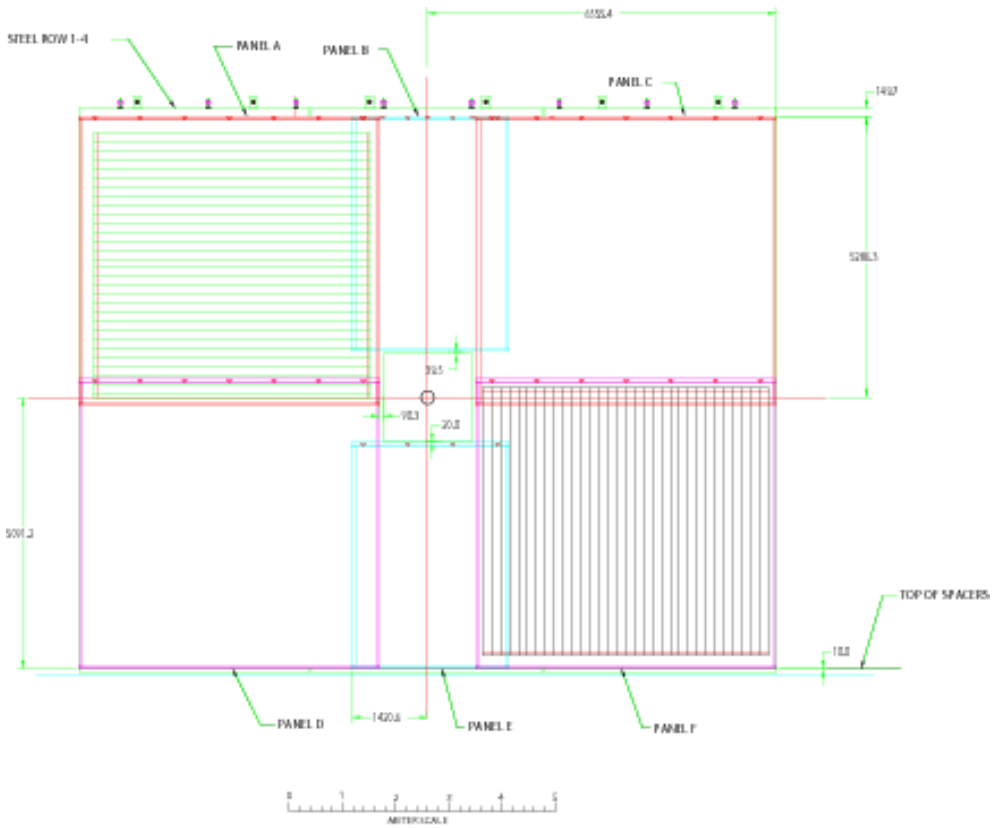



Figure 3.14: A drawing of one gap of the MuID. A gap consists of 4 large panels(Panels A,C,D and F) and 2 small panels (Panels B and E) as shown. Each panel has a horizontal tube array and a vertical tube array of two-packs. Dimensions are in mm.

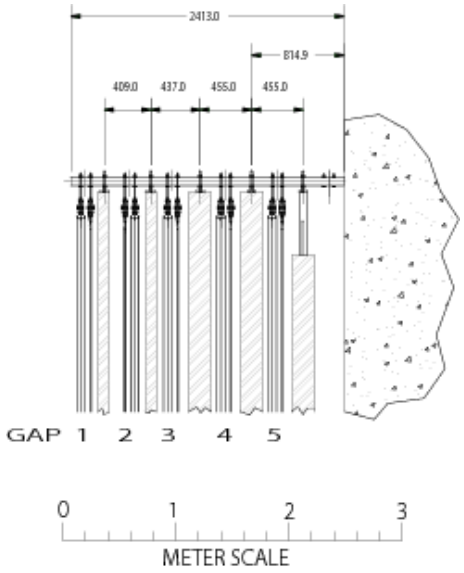



Figure 3.15: A side view drawing of the MuID gaps. The hatched materials are the steel wall absorbers. Dimensions are in mm.

steel (SS310) was installed in front of MuTr as discussed in section 3.2.1.

The other recent forward upgrade is installation of Forward Vertex Detector (FVTX). The purpose of FVTX is to enhance the capability of PHENIX muon arms by providing precision in tracking charged particles. The FVTX detector will be discussed more in section 3.2.7.

### 3.2.6 Resistive Plate Chambers(RPC)

As shown in Figure 3.5 RPC1 and RPC3 are insalled right before MuTr St1 and right behind MuID. Purpose of RPCs is to provide a dedicated trigger for $W$ measurement by providing excellent timing resolution. RPC3 was installed in 2009 and RPC1 was installed in 2011.

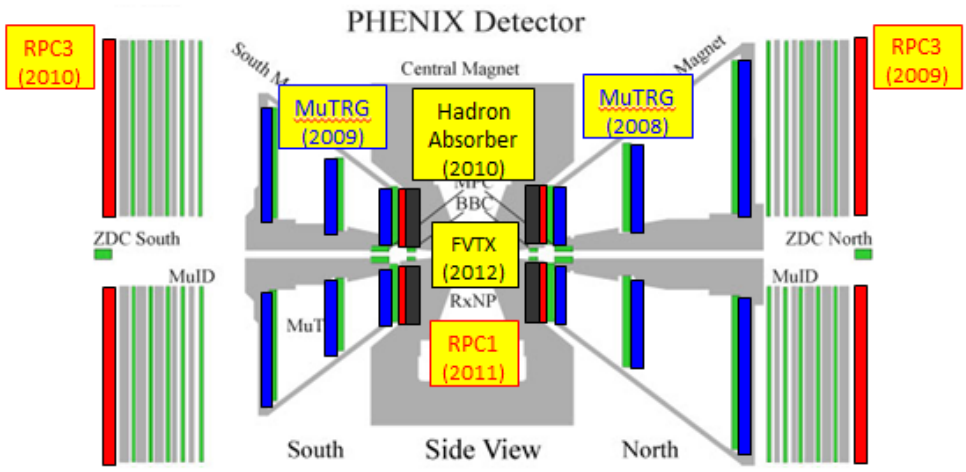



Figure 3.16: Recent upgrades in PHENIX muon arms[68].

In RHIC run 2013 proton-proton collisions at $\sqrt{s}$ = 510 GeV, the luminosity was so high that collisions occur almost in every bunch crossing (every 106 ns). So, it is important to have fast timing to avoid recording hits from previous or next bunch crossing. BBCs would mix up bunch crossings with the neighbouring beam crossing when the collision rate is high. Installing RPCs is one of the recent PHENIX forward upgrades to provide the required fast timing resolutions to differentiate bunch crossings. Geometry of one of the RPCs and cross-section view of the RPC layers are shown in Figure 3.17 and Figure 3.18

### 3.2.7 Forward Vertex Detector (FVTX)

One of the recent PHENIX forward upgrades is the installation of the Forward Vetex Detector (FVTX) in 2012. FVTX is silicon detector developed to enhance

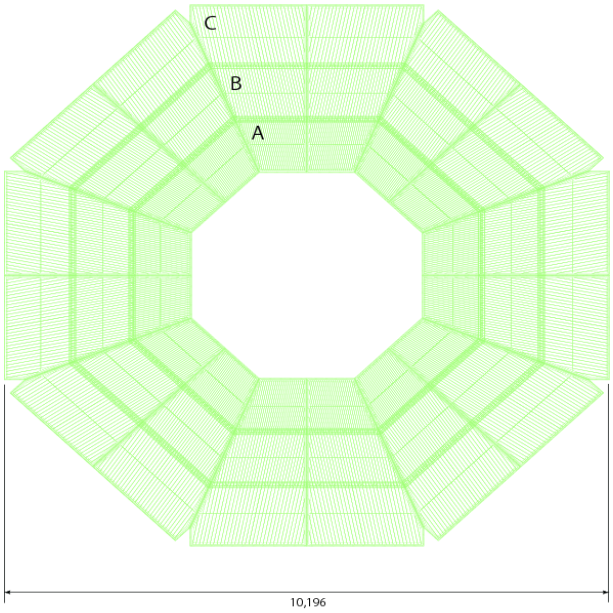



Figure 3.17: Geometry of the RPC3 strips. The width of the strip is different by regions A,B,C.

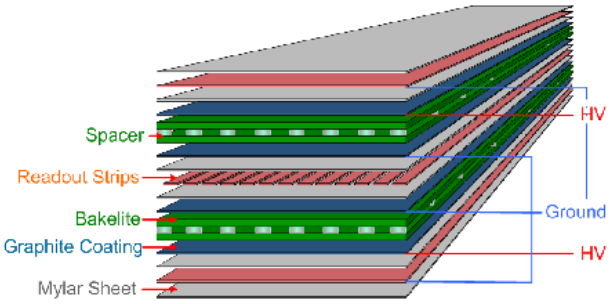



Figure 3.18: An exploded view of the layers of the RPCs.



Figure 3.19: RPC3 seen from the RHIC beam tunnel.

the capability of both PHENIX muon arms by providing precision in tracking charged particles before they interact with hadron absorber. FVTX will help suppress hadrons from jet for W. In RHIC run 2013 proton-proton collisions at $\sqrt{s} = 510$ GeV, FVTX was actively taking data with 90% of its sensors operational.

FVTX is composed of two arms located on either end of VTX (a 4 layer barrel silicon vertex detector in the central arms) covering rapidity $1.2 < \eta < 2.4$ that closely matches the existing south and north PHENIX muon arm trackers [69]. Each FVTX arm has 4 stations labeled as Station 0, 1, 2 and 3 in Figure 3.20. Each station is a disk consisting of $24 + 24$ silicon sensors (also called wedges) attached at the front and back of the disk plane. Station 0 is composed of smaller

sized wedges than stations 1, 2 and 3. Each wedge has two columns of array of mini-strips with 75 $\mu$m pitch in radial direction and 3.75° width in $\phi$ direction. In both arms, FVTX has a total of 1.08 Million mini-strips. A group of 128-channel front end readout ASICS called FPHX chips are wire bonded to the mini-strips. Summary of key design parameters of FVTX is given in Table 3.5.

Table 3.5: Summary of FVTX design parameters.

| **Parameter** | **Design** |
|---|---|
| Rapidity coverage | $1.2 < \|\eta\| < 2.4$ |
| Polar angle coverage (°) | 360 |
| Strip pitch ($\mu$m) | 75 |
| Strip ($\phi$) coverage (°) | 3.75 |
| Number of sensor wedges in a station | 48 |
| Strips per column for small, large sensor wedges | 640, 1664 |
| Inner radius of sensor wedges (mm) | 44.0 (all stations) |
| Outer radius of sensor wedges (mm) | 100.6, 170.0, 170.0, 170.0 |
| Mean z-position of stations (mm) | 201.1, 261.4, 321.7, 382.0 |
| Nominal operating sensor bias (V) | +70 |

From the data taken in RHIC run 2013 proton-proton collisions at $\sqrt{s}$ = 500 GeV FVTX has demonstrated single particle hit efficiency above 95 % with resolution better than 30 $\mu$m indicating that the intrinsic efficiency of the detector

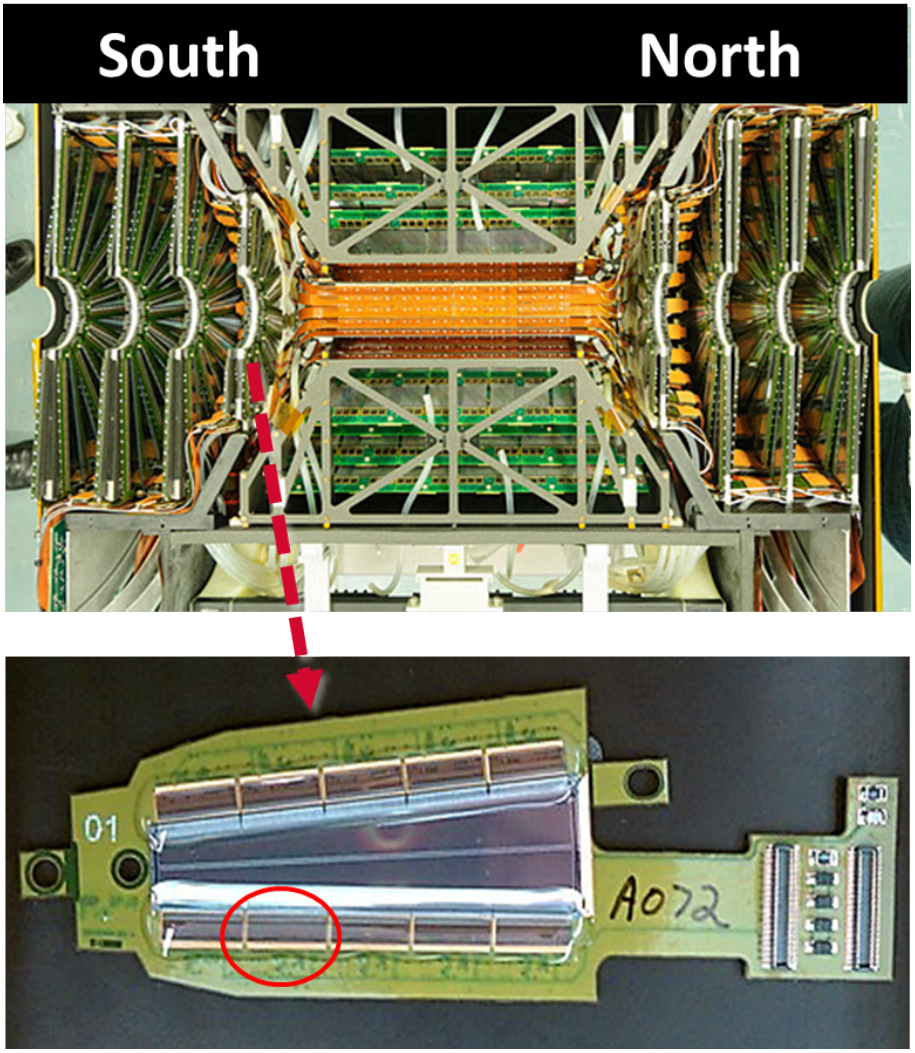



Figure 3.20: Top: Half of FVTX assembled. Half-disks corresponding to the 4 stations of each arm are shown. The overall length is 80 cm. Bottom: A completed FVTX small wedge, with sensor facing up. A Wedge has two columns of array of silicon mini-strips with 75 $\mu$m pitch in radial direction and 3.75° in $\phi$ direction. One of FPHX chips wire bonded to read 128 silicon mini-strips is shown in the red ring.

is quite high[70]. The probability of finding a hit at the projected spot in station 2 using tracks identified by hits in stations 0, 1, and 3 is shown in Figure 3.21, as a function of the angle $\phi$ around the disk[70]. Efficiency drops such as the one near $\phi = 90°$ in the north arm are due to broken component of ROC card. In general, in RHIC run 2013 proton-proton collisions the overall live area was greater than 95%[69].

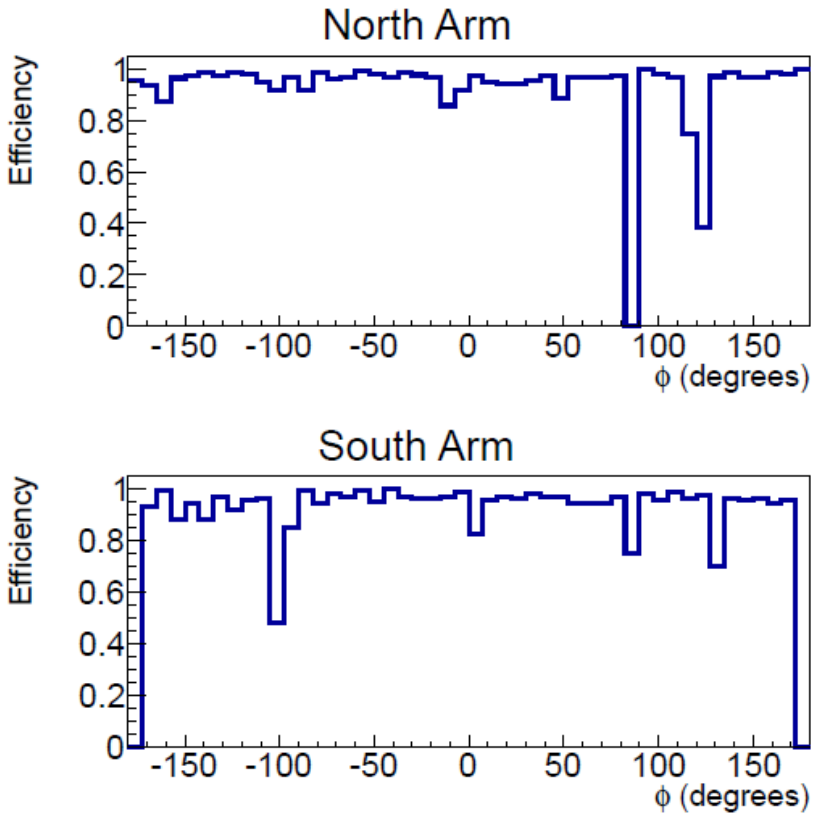



Figure 3.21: Hit efficiency for FVTX station 2 as a function of $\phi$

### 3.3 Data taking and Triggers

The PHENIX Data Acquisition System (DAQ) is compatible to the different collision rates and track multiplicities. The collision rate of heavy ion collisions is a few kHz while the multiplicity of tracks are enormous. On the other hand, the collision rate of proton-proton collisions are a few MHz, but the track multiplicity is not so large. An efficient and streamlined triggering system is designed to optimize data taking in PHENIX. The root of the clock of the DAQ system is the RHIC original clock of 9.4 MHz which controls the beam bunches. For every bunch crossing in RHIC, each PHENIX detector subsystem's signals are processed by their Front End Modules (FEM) and passed to the detector's Front End Electronics (FEE), where the analog and timing signals measured by the detector are converted to digital format by analog-to-digital conversion (ADC) and timing-to-digital conversion (TDC). Figure 3.22 illustrates the PHENIX DAQ system[78].

At PHENIX the Master Timing Module (MTM) receives the RHIC clock and distributes to Global Level-1 Module (GL1) and Granule Timing Modules (GTM) which corresponds to each sub-system. And GTM forwards the clock to FEMs. GL1 manages Local Level1 triggers (LL1) which are provided by user. Once the clocks are synchronized, if GTM is not busy and LL1 conditions are satisfied, GL1 issues a trigger signal to the GTMs and each GTM transmits to its FEMs. Then FEM digitizes the corresponding timing event data and sends it to the Data

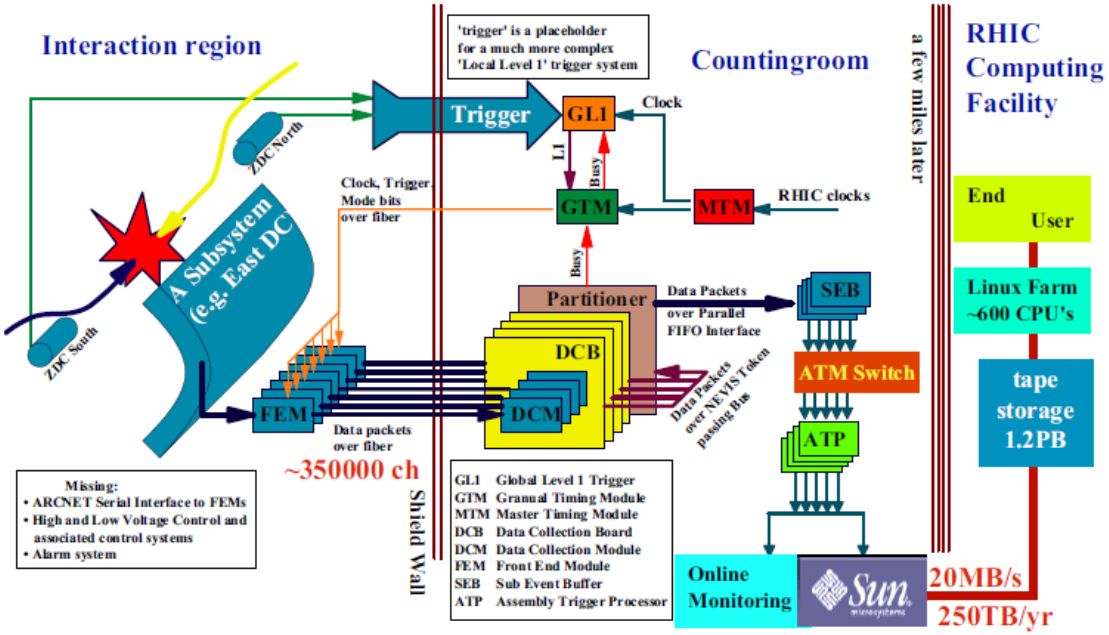



Figure 3.22: Illustration of the PHENIX DAQ system[78].

Collection Module (DCM). Signals from FEM and FEE in the PHENIX IR are carried to DCM in the PHENIX control room by fiber optic cables of length about 20 m long.

After Quality assurance and signal reprocessing in DCM, parallel DCM signals are passed to the Sub Event Builder (SEB) and onto the Assembly and Trigger Processors (ATP). Data passing all the above conditions are then passed to the PHENIX On-line Control System (ONCS), where it is further processed and stored for eventual offine analysis. A full description of the data taking procedure, from the initial processing of signals in the FEM to data storage is outlined in [52] and [53].

As a multi-purpose detector, the PHENIX uses various level-1 triggers. There are totally 32 slots of the level-1 triggers, and each trigger can take data separately. The elements of the level-1 trigger, as described in the previous section, are called local level-1 (LL1) triggers. A LL1 trigger can be a standalone trigger, or it can be combined with other LL1 triggers to generate some elaborate triggers. In the following paragraphs, several LL1 triggers related with this thesis are described.

**Minimum bias triggers (BBCLL1)** The minimum bias (MB) triggers are used to monitor the luminosity, assigns the collision to its timing. The MB triggers use the BBCs. The MB triggers issue the trigger bit when both the South and North BBC modules have more than one hits.

Three triggers are provided. The first one has no requirements on the vertex position of the collision (called BBCLL1($>$ 0tubes) novertex), and the second one requires the $z$-position of the collision vertex within 30 cm from the origin (called BBCLL1($>$ 0tubes) and $|z_{\rm vtx}| < 30$ cm), and the last one requires the collision vertex within 15 cm from the origin (calledBBCLL1($>$ 0tubes) and $|z_{\rm vtx}| < 15$ cm). The vertex cut of $|z_{\rm vtx}| < 30$ cm roughly matches with the acceptance of the Central Arms, and $|z_{\rm vtx}| < 15$ cm corresponds to the acceptance of the VTX detector. These triggers are not referred so much in this thesis, since the Muon Arms have much wider acceptance and VTX was not fully functional in RHIC 2013 run.

**MuID Local Level 1 Trigger (MuIDLL1)** In MuID, If you consider a line connecting a collision vertex to a hit at gap-1 logical tube, the most probable trajectory is to continue on a path of same slope (equal dx/dz (vertical tubes) or dy/dz (horizontal tubes)). Tubes with the same dx/dz (or dy/dz) get the same index. Then the logical tubes in the other gaps which intersect with the line are grouped as a set called *symset*. Two symset logic conditions are provided. One is called "1D (one-deep)", which is used for identifying muons, and the other is called "1H (one-hadron)", which is used for identifying hadrons. Counting the gaps from 0 to 4, the 1D algorithm requires at least one hit in the gap-3 or the gap-4, while the 1H algorithm requires no hits in the gap-4. The logic diagrams of the two conditions are shown in Figure 3.23.

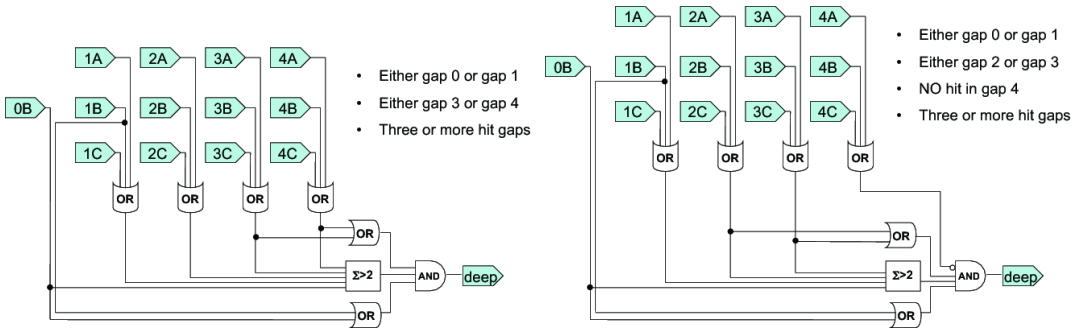



Figure 3.23: MuID symset logics. The left is MuID-1D (one-deep) logic and the right is MuID-1H (one-hadron) logic.

The MuIDLL1 can provide the trigger condition for plural tracks, called "2D (two-deep)" or "1D1H (one-deep and one-hadron)", etc. Note that the 2D algorithm is not only the product of two 1D trigger conditions, but it also considers the opening angle between the two tracks. The three possible MuIDLL1 triggers used are triggers as follows:

- MuID-1D "(MUIDLL1_N1D||S1D)&BBCLL1(noVtx)"

  This trigger is fired when either the South or North MuID satisfies the 1D condition as well as the BBC(novtx) condition.

- MuID-1H "(MUIDLL1_N1H||S1H)&BBCLL1(noVtx)"

  This trigger is fired when either the South or North MuID satisfies the 1H condition as well as the BBC(novtx) condition.

- MuID-2D "((MUIDLL1_N2D||S2D)||(N1D&S1D))&BBCLL1(noVtx)"

  This trigger is fired when either the South or North MuID satisfies the 2D

condition, or both the South and North MuID satisfy the 1D condition. Also the BBC(novtx) condition is additionally required.

All the muon triggers (including MUIDLL1 triggers) used in Run 2013 are given in Table 3.6.

**Mutrg-LL1** The Mutrg-LL1 uses the hit patterns of the MuTr for triggering. If the MuTr hit pattern of the event matches with any of the trigger maps, the LL1 trigger bit is issued. There are several classes of trigger maps, classified with the size of sagitta. The sagitta is defined as the distance between the station-2 hit and the intersection point of the station-2 plane and the line which connects the station-1 hit and the station-3 hit digitized by the strip size. The trigger map which allows up to $N$-strip sagittas is classified as SG$N$. The trigger maps are determined based on the GEANT simulation (PISA). The momentum threshold of the SG1 trigger map is $p_T \simeq 2.5$ (3.5) GeV/$c$ for the South (North) Arm. In year 2013 runs the SG1 trigger map was employed for triggering $W^{\pm} \to \mu^{\pm}$ event candidates. Note that the larger $N$-strip trigger map includes the smaller $N$-strip trigger maps. For example, all strip combinations in the SG0 trigger map are included in the SG1 trigger map.

**Physics triggers for $W^{\pm} \to \mu^{\pm}$** The physics triggers used in this thesis employ the coincidence of BBC(novtx), MuID-1D and Mutrg-SG1 LL1 triggers as

schematically shown in Figure 3.24.

- South Arm: MUON_S_SG1&BBCLL1(NoVtx)&MUIDLL1_S1D
- North Arm: MUON_N_SG1&BBCLL1(NoVtx)&MUIDLL1_N1D

For short, we use the conventions "WTRG(S)" and "WTRG(N)" hereafter.

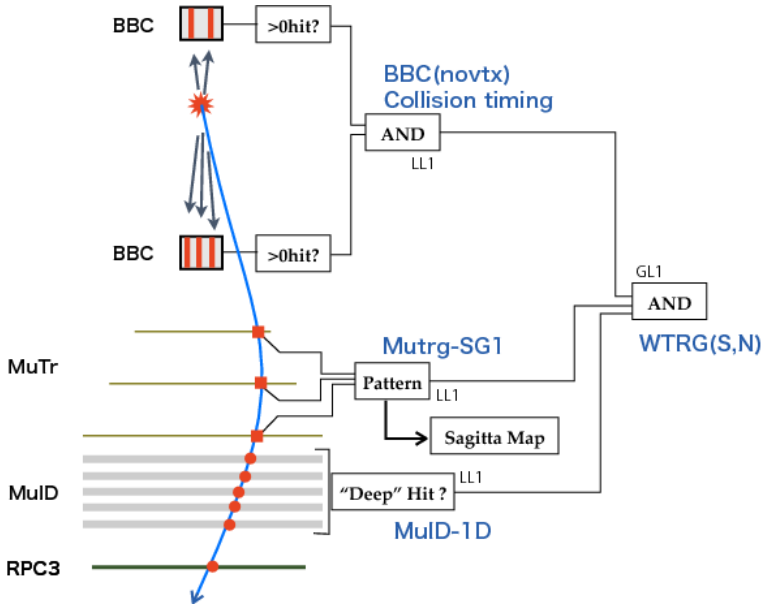



Figure 3.24: Schematic illustration of the physics trigger for $W^{\pm} \to \mu^{\pm}$.

Table 3.6 shows muon triggers employed for the $W$ analysis in RHIC run 2013 proton-proton collisions[54].

Table 3.6: Muon triggers employed in RHIC run 2013 proton-proton collisions at $\sqrt{s} = 510$ GeV.

| **Bit** | **Trigger Name** |
|---|---|
| 9 | SG3&MUID_1H_N\|\|S |
| 16 | ((MUIDLL1_N2D\|\|S2D)\|\|(N1D&S1D))&BBCLL1(noVtx) |
| 17 | (MUIDLL1_N1D\|\|S1D)&BBCLL1(noVtx) |
| 18 | RPC1+RPC3 S |
| 19 | RPC1+RPC3 N |
| 20 | SG3&RPC3&MUID_1D_N\|\|S |
| 21 | SG1+RPC1(C)&MUIDLL1_N\|\|S |
| 22 | MUON_S_SG1_RPC3A&MUID_S1D |
| 23 | MUON_N_SG1 RPC3A&MUID_N1D |
| 24 | MUON_S_SG1&BBCLL1(noVtx) |
| 25 | MUON_N_SG1&BBCLL1(noVtx) |
| 26 | MUON_S_SG1_RPC3_1_B\|\|C |
| 27 | MUON_N_SG1_RPC3_1_B\|\|C |

# 4 Data Set

## 4.1 Overview

This thesis analyzes the data from RHIC run 2013 proton-proton collisions at $\sqrt{s} = 510$ GeV. RHIC run 13 has been mostly dedicated to spin physics, and in particular the main priority was the forward $W$ to $\mu$ measurements[54]. During the run, proton-proton beams have been collided at a center of mass energy $\sqrt{s} = 510$ GeV, and the final average beam longitudinal polarizations have been $54 \pm 0.42\%$ for the blue beam, and $55 \pm 0.40\%$ for the yellow beam. PHENIX collected a luminosity of 240 pb$^{-1}$, more than three times the total luminosity previously collected during run11 (25 pb$^{-1}$) and run12 (50 pb$^{-1}$).

In RHIC, polarized protons are filled in both yellow and blue rings and stay for about 8 hours. Each fill is identified by fill number associated to RHIC. The PHENIX DAQ collects data in a unit of 1.5 hour at a time. This data taking unit is identified by run number associated to PHENIX. Normally, several runs are taken in a fill. The fill numbers used in this thesis range from 17156 to 17601, and the corresponding run numbers in Run 2013 production ready for analysis ranges from 386773 to 398149. Among these, totally 1778 runs are the physics runs used in the analysis. In addition to physics runs, the PHENIX takes other categories of runs for different purposes. The zero field runs are taken every time before turning the magnets on. The zero field runs are used to calibrate

the alignment of muon arm detectors. To study cosmic backgrounds, cosmic run data is taken before the physics run while beams are not filled. The cosmic runs are taken with only the MuID trigger turned on. The calibration runs are taken normally once per day. Calibration runs are taken for each detector subsystem, by the standalone DAQ mode. Calibration runs are also taken normally once a day for each detector subsystem and latter will be referred at the time of data production. Since the figure of merit for a single spin asymmetry goes as $P^2L$, it is of the utmost importance to maintain a high polarization and luminosity. Figure 4.1 shows comparison of the achieved integrated luminosity and polarization for different proton proton runs in RHIC. Integrated figure of merit metric vs. day for RHIC run 2013 is shown in Figure 4.2.

In this chapter the analyzed real data as well as simulations relevant to the analysis are discussed.

## 4.2 Luminosity Monitor

To measure spin asymmetry, its imperative to know very well the number of collisions that have occurred. In PHENIX the luminosity is monitored by BBCs. The BBCs detect proton-proton inelastic scattering collisions with a fraction called BBC efficiency, $\varepsilon_{\mathrm{BBC}}$ due to diffraction and similar events. BBC's luminosity monitoring is triggered by requiring coincidence of both North and South BBC arms detect hits, see Figure 4.3-a. However in cases when more than one collision

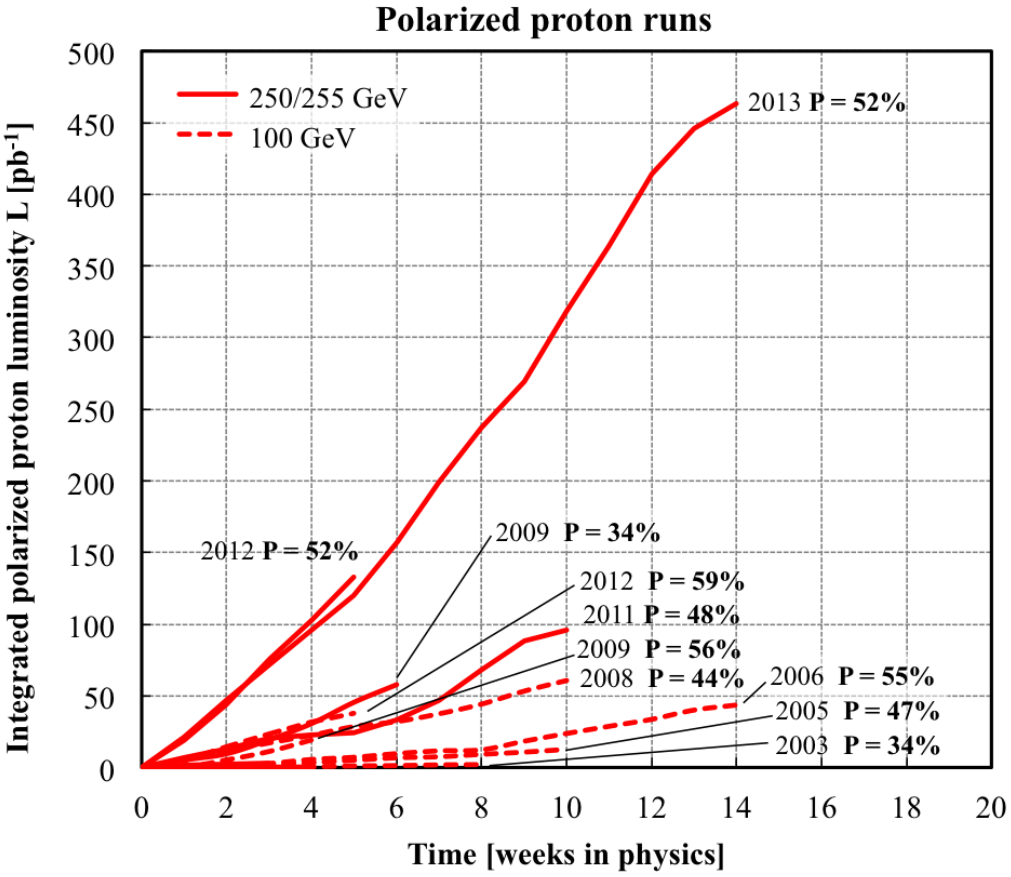



Figure 4.1: Comparison of the polarization and total integrated luminosity achieved for the polarized pp runs at RHIC.

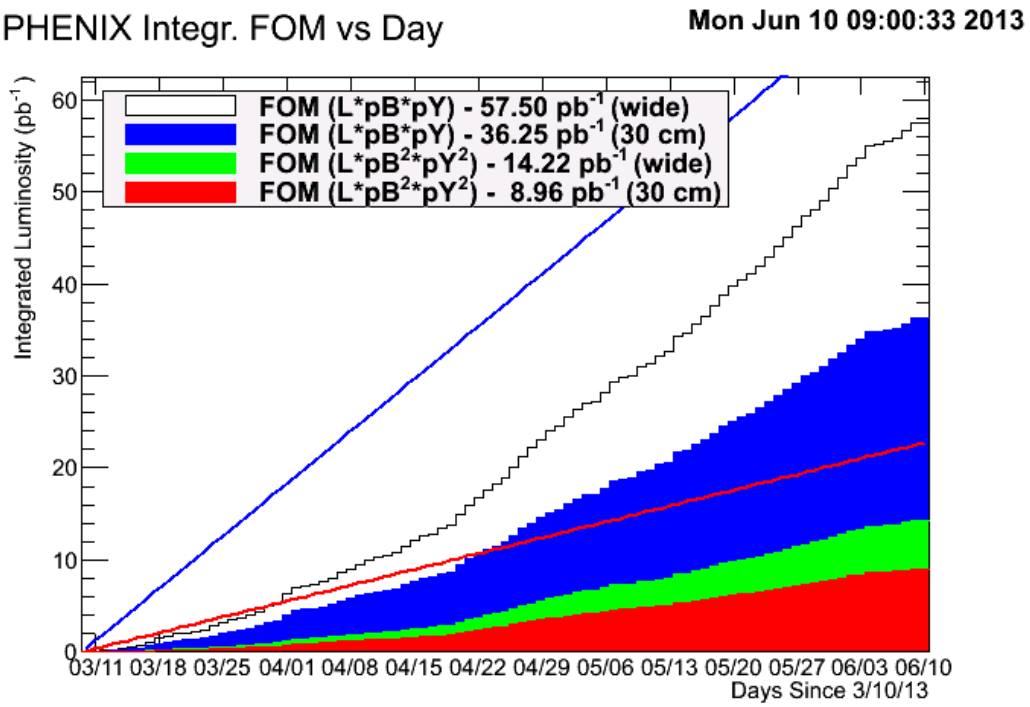



Figure 4.2: Integrated figure of merit metric vs. day for the Run 2013 running period at RHIC.

occurs, counting collisions based on only coincidences may lead to over (under) counting collision[83]. This condition is called pile up. For example, consider a case when two collisions occur and one collision hits only the south BBC and the other collision hits the south BBC, see Figure 4.3-b. In this particular case BBCs will misread the incident as one collision with triggered event. However, these two single side hit collisions do not actually satisfy BBC trigger condition (2 hits) and should have been rejected. This would result in over-counting of collisions. Similarly, Figure 4.3-c and d shows another condition that would lead to under-counting.

The pile-up correction study has been performed for the last three $W \rightarrow \mu$ running periods by forward analysis group of PHENIX . The technique used was initially developed by the central $W$ analysis [82] and later refined for various double spin asymmetry measurements [83, 84]. For further details the reader is asked to study these analysis notes. The general idea is, that the luminosity detectors, in this case the BBC, has a finite efficiency for each side and therefore can either undercount or overcount the actual number of collisions. Instead of calculating the efficiencies for one, two, three, etc collisions in one crossing together, it is easier to calculate the probablity of not counting any collision. In an iterative procedure which generally converges after one or two iterations, the north (south) efficiencies $k_N$, ($k_S$) were evaluated based on the true number of collisions per

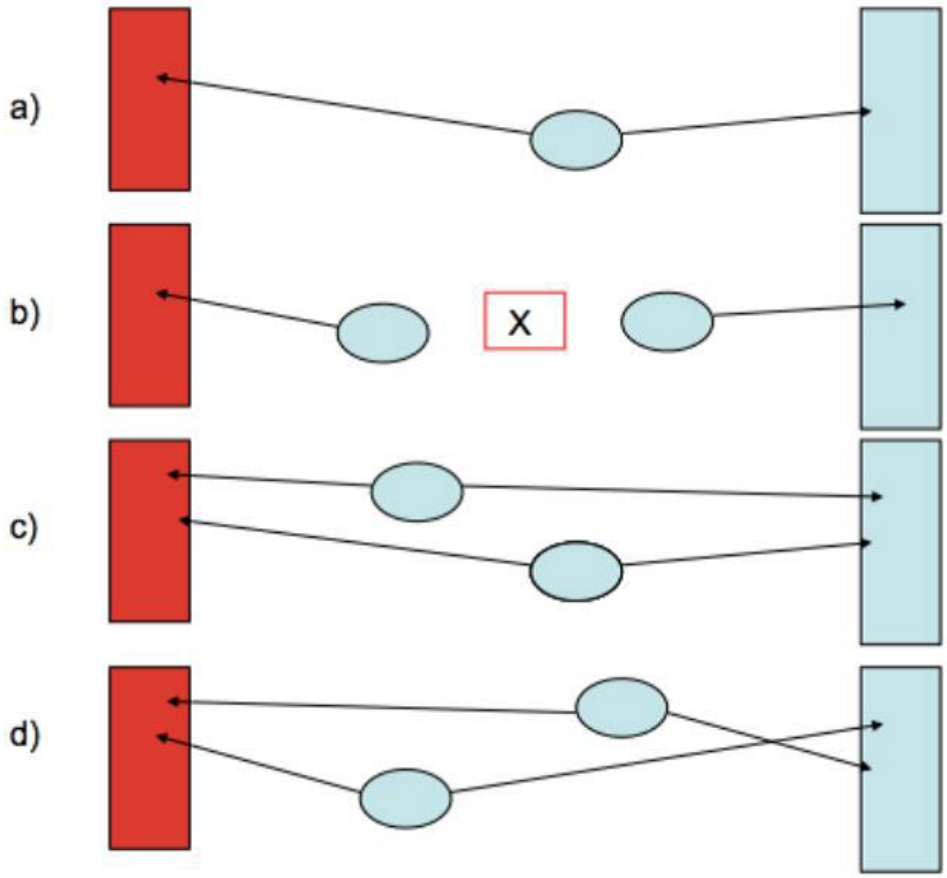



Figure 4.3: Examples of pileup. The boxes at the left and right representing North and South BBCs : a)Normal Collision. b)Two collisions in the same crossing w/false vertex, but only one hit per collision per side. c and d) Two collisions producing two hits, generating four possible vertexes 2 real and 2 ghosts

crossing $\mu$:

$$R_{BBC} = 1 - e^{-\mu\epsilon_{BBC}(1+k_N)} - e^{-\mu\epsilon_{BBC}(1+k_S)} + e^{-\mu\epsilon_{BBC}(1+k_N+k_S)} \quad , \tag{4.1}$$

where $R_{BBC}$ is the observed number of collisions per crossing and $\epsilon_{BBC}$ is the overall BBC efficiency of 0.53 for any given collision due to diffractive and similar events. This way the actual average collisions rate can be evaluated for each run. And the actual luminosity can then be obtained via the collision frequency ( $f_{coll} = 1/106$ ns), the duration of the run $t$, its live fraction and the total BBC cross section ( at 510 GeV, $\sigma_{pp} = 61$ mb ):

$$L_i = \frac{BBC_{live}}{BBC_{raw}} \times t \times f_{coll}/\sigma_{pp} \quad . \tag{4.2}$$

Summing up all produced runs available on the production data, one thus obtains a total luminosity of 277 pb$^{-1}$. The actual number or collisions as well as the measured and true MinBias collisions rates for each run are displayed in Figure 4.4.

The collision frequency also depends on the number of actually filled bunches (for run13 between 107 to 111 of the 120 bunches). As this affects also the evaluation of the actual number of collisions per crossing, $\mu$ taking this correction into account or not has a negligible effect on the total luminosity.

### 4.3 Beam polarization

As discussed in Sec. 3.1.3, the beam polarization is measured with the CNI polarimeter for relative profiling and the H-jet polarimeter for absolute calibration.

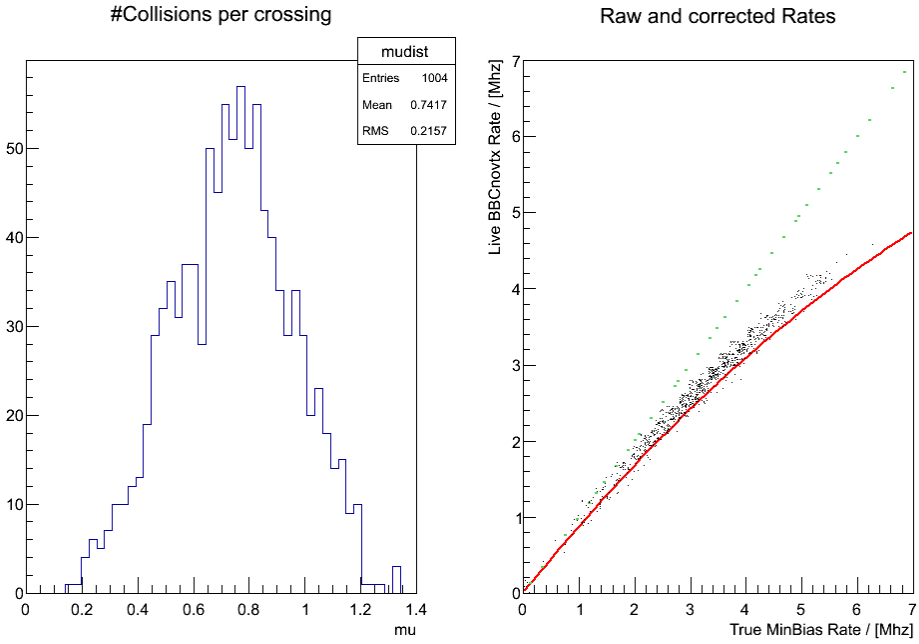



Figure 4.4: Left: distribution of number of collisions per crossing $\mu$ for all runs in the 2013 running period. Right: True and observed BBCnovtx live rates for all runs as a function of the true rate and calculated as described in the text. The green, dashed line reprents a perfect accounting of true collisions, while the red curve takes the efficiencies of the two BBC sides into account.

Figure 4.5 shows the fill-by-fill beam polarization after correcting the absolute scaling in 2013 runs[85].

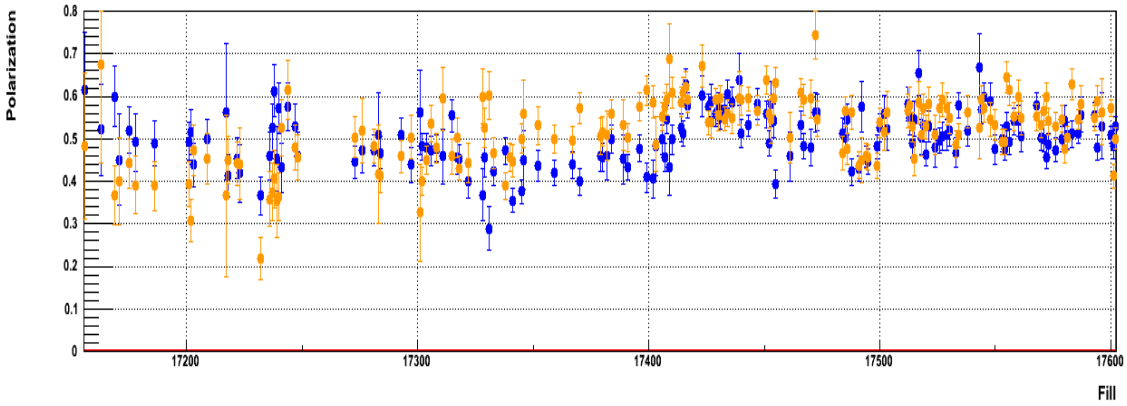



Figure 4.5: Fill-by-fill beam polarizations in year 2013 runs for the Blue beam and Yellow beam.

The RHIC/AGS accelerator complex has the capability to inject up to 120 bunches of protons into the storage ring in a given fill. In order to dump the beam when the experiments and CAD (Collider-Accelerator Department) agree the fill should end, an abort kicker is used to steer the beam out of its orbit and into a concrete absorber. The abort kicker takes about 1 $\mu$s to ramp up. The RF cavity has a frequency of 9.383 MHz so each bunch has an associated time (length) of 106.572 $s$ (31.949m). Therefore, an abort gap of at least 9 bunches (for Run 2013 9 to 13 bunches) in each beam is left unfilled to allow time for the kicker to ramp up. There are therefore 111 maximum crossings with collisions for

the PHENIX experiment to observe, though a given fill always has a few less than this. As each crossing passes through the PHENIX Interaction Region (IR) its polarization is rotated from its default transverse direction into the longitudinal direction, either in the same direction as its momentum, giving it positive helicity, or in the opposite direction of its momentum with negative helicity. Bunches with positive helicity are referred to as + bunches and bunches with negative helicity are referred to as − bunches. Table 4.1 and 4.2 show the different types of spin patterns that RHIC was filled at different times in Run 13 [86].

Table 4.1: Spin patterns used in the initial part of run 13.

| | | | | | | | | | | | | | | |
|---|---|---|---|---|---|---|---|---|---|---|---|---|---|---|
| P1 BLUE: | + | + | - | - | + | + | - | - | + | + | - | - | | |
| YELLOW: | + | + | + | + | - | - | - | - | + | + | + | + | - | - |
| P2 BLUE: | - | - | + | + | - | - | + | + | - | - | + | + | | |
| YELLOW: | + | + | + | + | - | - | - | - | + | + | + | + | - | - |
| P3 BLUE: | + | + | - | - | + | + | - | - | + | + | - | - | | |
| YELLOW: | - | - | - | - | + | + | + | + | - | - | - | - | + | + |
| P4 BLUE: | - | - | + | + | - | - | + | + | - | - | + | + | | |
| YELLOW: | - | - | - | - | + | + | + | + | - | - | - | - | + | + |
| P5 BLUE: | + | + | + | + | - | - | - | - | + | + | + | + | - | - |
| YELLOW: | + | + | - | - | + | + | - | - | + | + | - | - | | |
| P6 BLUE: | + | + | + | + | - | - | - | - | + | + | + | + | - | - |
| YELLOW: | - | - | + | + | - | - | + | + | - | - | + | + | | |
| P7 BLUE: | - | - | - | - | + | + | + | + | - | - | - | - | + | + |
| YELLOW: | + | + | - | - | + | + | - | - | + | + | - | - | | |
| P8 BLUE: | - | - | - | - | + | + | + | + | - | - | - | - | + | + |
| YELLOW: | - | - | + | + | - | - | + | + | - | - | + | + | | |

Table 4.2: Spin patterns for the later part of run 13

| | | | | | | | | | |
|---|---|---|---|---|---|---|---|---|---|
| P21 BLUE: | + | + | - | - | + | + | - | - | repeat |
| YELLOW: | + | + | + | + | - | - | - | - | repeat |
| P22 BLUE: | - | - | + | + | - | - | + | + | repeat |
| YELLOW: | + | + | + | + | - | - | - | - | repeat |
| P23 BLUE: | + | + | - | - | + | + | - | - | repeat |
| YELLOW: | - | - | - | - | + | + | + | + | repeat |
| P24 BLUE: | - | - | + | + | - | - | + | + | repeat |
| YELLOW: | - | - | - | - | + | + | + | + | repeat |
| P25 BLUE: | + | + | + | + | - | - | - | - | repeat |
| YELLOW: | + | + | - | - | + | + | - | - | repeat |
| P26 BLUE: | + | + | + | + | - | - | - | - | repeat |
| YELLOW: | - | - | + | + | - | - | + | + | repeat |
| P27 BLUE: | - | - | - | - | + | + | + | + | repeat |
| YELLOW: | + | + | - | - | + | + | - | - | repeat |
| P28 BLUE: | - | - | - | - | + | + | + | + | repeat |
| YELLOW: | - | - | + | + | - | - | + | + | repeat |

## 4.4 Types of background

The signal muon candidates from the $W$ decay are affected by a number of background processes that can be summarized into two main sources[54]

1. muonic background
2. hadronic background
    - punch-through charged hadrons
    - fake high-$p_T$ muons from hadrons decaying in Muon Tracker volume.

The actual distribution of these background events falls quickly with $p_T$ and are negligible in the $p_T$ range of interest for this analysis: $16 - 60$ GeV/$c$.

**Muonic background.** The muons we are interested to count are those from $W$ decay. However, muons detected in the muon arms could also be generated by processes other than $W$ decays. For instance open heavy flavors decays, quarkonia, Drell-Yan, direct photon production or $Z$ decays. Such background contributions decrease quickly with $p_T$, and they are generally negligible in the $p_T$ range used in this analysis: $16-60$ GeV, except for a small contribution ($\sim 10\%$) from $Z$ decays. Nonetheless, due to MuTr momentum smearing, low-$p_T$ muons coming from the mentioned background processes can be wrongly reconstructed as high-$p_T$ muons, thus they still should be treated as background.

**Hadronic background.** The dominant background contribution in $W$ measurement comes from hadronic processes. During proton-proton collisions a large number of charged hadrons, mainly pions and kaons, are generated. Unlike muons, most of such hadrons are absorbed by the central magnet or, later, by the MuID steel walls and thus do not reach the last MuID gap or the RPC3: these hadrons are therefore not included in the muon sample and do not represent a background.

**punch-through hadrons** are hadrons which penetrate all the way to the last MuID and RPC3. **Hadrons decaying insde MuTr** are hadrons which

decay in flight inside the MuTr to muons (also called fake muons in Section 2.5.1). Both these categories of events represent a possible background source. For both punch-through hadrons or muons from hadron decays, the tracks generally have lower energy with respect to the high momentum muons from $W$. In particular, the largest background is coming from hadrons decaying in the MuTr region that generates muons; in this case indeed, the tracking algorithm try, to fit the hits from the original hadron and the ones from the decayed muon asif the track is constructed from a single high-energy muon track. Although only a very small fraction of hadrons survives to the MuTr, the total cross section is so much high that this becomes the dominating background.

Figure 4.6 shows the various contributions from the mentioned background sources and from the $W \rightarrow \mu$ signal included in the single muon candidate sample. After applying tight cuts, the charged hadron background sources dominate the muon data sample yields.

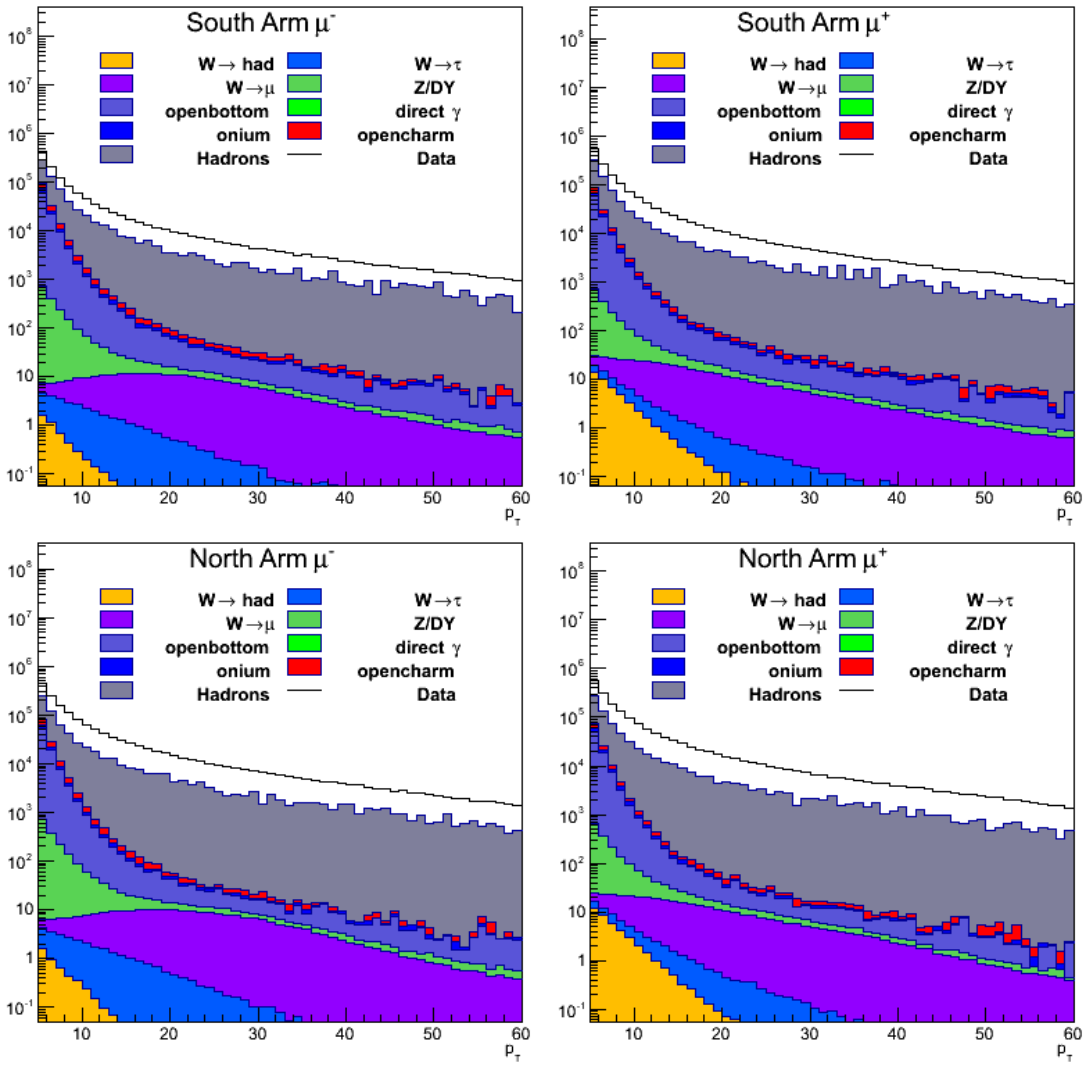



Figure 4.6: Stacked, cross sections as a function of the reconstructed $p_T$ using basic cuts for the separate simulated subprocesses as well as hadronic background as described in the text.

For analysis in this thesis MC simulations has been produced specifically for the Run 2013 analysis. They take into account the rate dependent effects of both Muon tracker and MuID approximated by the average rate over the whole 2013 running period.

The next two sections are mainly extracted from the analysis note we produced for Run 13 $W$ measurement and will discuss the nature of the signal, muonic background and hadronic background produced by $W$ analysis group of PHENIX.

### 4.5 Pythia related signal and muonic background simulations

Most of the muonic backgrounds are coming from different sub-processes. And, since their cross sections in rapidity regions of our interest are only partially known, simulations for muon producing sub-processes are required. For these, full event simulations were produced based on the Run 13 geometry and a reference run 393888 which will be discussed in Table 4.3. In these simulations, process-separated events are created using the so-called Pythia tune A [88] for light and diffractive, open charm, open bottom, onium, direct photon, Drell Yan and Z boson as well as $W$ boson production. This Pythia tune A was optimized to match the cross sections measured at the Tevatron.

In order to reduce computing time and concentrate on the high momentum part of interest only events with a muon with transverse momentum of at least $4\,\mathrm{GeV}/c$ pointing towards the muon arms ($1.1 < |\eta| < 2.5$) were selected. In addition the

$W$ process events were split up on the Pythia level in those originating directly into a $W$ decay muon and those muons produced either via an initial $W \to \tau + cc.$ decay (specified as $Wtau$ below) or hadronic $W \to q\overline{q}$ decay ($Whad$). The vertex $z$ distribution of the initial collision was taken as a Gaussian with width of 40 cm which resembles the actual data reasonably well.

For the study of the dependence on the collision rate three various reference runs were used to sample the detector response at low, medium and high collision rates. The reference runs, collision rates and MuTr efficiencies are summarized in Table 4.3.

Table 4.3: Multiple collision parameter $\mu$, luminosities and MuTR efficiencies for various run12 and Run 2013 reference runs used in the simulations.

| Arm | Run Number | $\mu$ | L nb$^{-1}$ | MuTr Efficiency |
|---|---|---|---|---|
| North | 367466 (Run 2012) | 0.576 | 56.9074 | 0.9051 |
| | 367593 (Run 2012) | 0.876 | 42.8445 | 0.8458 |
| | 368630 (Run 2012) | 0.409 | 60.4362 | 0.9281 |
| | 393888 (Run 2013) | 0.741 | 289.368 | 0.8753 |
| South | 367466 (Run 2012) | 0.576 | 56.9074 | 0.9513 |
| | 367593 (Run 2012) | 0.876 | 42.8445 | 0.9475 |
| | 368630 (Run 2012) | 0.409 | 60.4362 | 0.9556 |
| | 393888 (Run 2013) | 0.741 | 289.368 | 0.9486 |

The individual cross section as well as the initially generated number of events are summarized in Table 4.4 .

Table 4.4: Simulated sub-processes produced using reference run 393888 in Run 2013 including their generated event numbers as well as the corresponding luminosity.

| process | k factor | $\sigma$ (mb) | Num of gen events | Luminosity ($fb^{-1}$) |
|---|---|---|---|---|
| light | 1.5 | 5.94e+01 | 7 G | 0.00012 |
| open charm | 1.5 | 5.71e-01 | 584 G | 1.02 |
| onium | 1.5 | 1.35e-01 | 150 G | 1.11 |
| direct photon | 1.5 | 5.32e-02 | 58 G | 1.10 |
| open bottom | 1.5 | 7.30e-03 | 7 G | 1.01 |
| z/DY | 1.5 | 1.59e-05 | 292 M | 17.64 |
| ONLYZ | 1.5 | 3.37e-07 | 173 M | 577.0 |
| W | 1.5 | 1.66e-06 | 338 M | 198.9 |
| Wtau | 1.5 | 1.66e-06 | 343 M | 201.8 |
| Whad | 1.5 | 1.66e-06 | 342 M | 201.2 |
| zjet | 1.5 | 1.02e-06 | 73 M | 61.2 |
| Wjet | 1.5 | 1.20e-06 | 73 M | 73.7 |

### 4.6 Single hadron background simulations

The hadron simulations were produced for separately generated transverse momentum bins between 1 and 13 GeV/$c$ for the four most dominant hadron species $K^+$,$K^-$, $\pi^+$ and $\pi^-$. A Gaussian vertex $z$ distribution of 40 cm width was generated to resemble the data as good as possible. The flat distribution was simulated between $1.2 < |\eta| < 2.2(2.4)$ for the South (North) arms respectively and later extended to 2.3(2.5). The prescription follows closely the one described in PHENIX Analysis notes 899 and 1024 [90, 91]. The individual transverse momentum bins are reweighted according to their cross section by either using the UA1 spectra modified for the forward rapidities or using the NLO perturbative QCD calculations. The absolute yield and general composition of the background does not change as the differences are only sizable at very high transverse momenta where the cross sections are not relevant anymore for the $W$ analysis. As only a few hadrons survive into the muon tracker, a large amount of hadrons had to be simulated through PISA and the muon reconstruction chain. The total amount of simulated hadrons to present are summarized in Table 4.5 for the Run 2013 simulations. As studied in the run11 analysis [91] the $K^+$ dominate in the transverse momentum range of interest with a fraction of 60% to 70% depending on the reconstructed charge of the muon track. The $K^-$ contribute another 20-30% while the $\pi$ contribution is on the order of 10% combined. One only sees larger

Table 4.5: Run 13 single hadron simulated events and weights as a function of arm, species and generated momentum.

| $p_T$ bin | $K^+$ | | $K^-$ | | $\pi^-$ | | $\pi^+$ | |
|---|---|---|---|---|---|---|---|---|
| [GeV/c] | South Arm | | | | | | | |
| 1 - 2 | 1.44e+10 | 2.76e+01 | 1.44e+10 | 2.57e+01 | 1.47e+10 | 2.13e+02 | 1.46e+10 | 2.16e+02 |
| 2 - 3 | 2.83e+10 | 1.17e+00 | 2.82e+10 | 1.10e+00 | 2.85e+10 | 4.43e+00 | 2.83e+10 | 4.53e+00 |
| 3 - 4 | 7.15e+09 | 6.05e-01 | 7.14e+09 | 5.48e-01 | 7.16e+09 | 1.96e+00 | 7.14e+09 | 2.02e+00 |
| 4 - 5 | 1.31e+09 | 7.08e-01 | 1.31e+09 | 6.10e-01 | 3.85e+09 | 7.09e-01 | 3.86e+09 | 7.42e-01 |
| 5 - 6 | 3.11e+08 | 8.62e-01 | 3.10e+08 | 7.10e-01 | 9.03e+08 | 8.16e-01 | 9.03e+08 | 8.72e-01 |
| 6 - 7 | 9.11e+07 | 1.05e+00 | 8.82e+07 | 8.41e-01 | 2.59e+08 | 9.52e-01 | 2.58e+08 | 1.05e+00 |
| 7 - 8 | 3.06e+07 | 1.28e+00 | 3.04e+07 | 9.45e-01 | 8.58e+07 | 1.12e+00 | 8.63e+07 | 1.25e+00 |
| 8 - 9 | 3.07e+07 | 5.77e-01 | 3.03e+07 | 4.05e-01 | 3.28e+07 | 1.26e+00 | 3.26e+07 | 1.46e+00 |
| 9 - 10 | 1.66e+07 | 5.21e-01 | 1.71e+07 | 3.33e-01 | 4.14e+07 | 4.68e-01 | 4.04e+07 | 5.68e-01 |
| 10 - 11 | 1.72e+07 | 2.63e-01 | 1.70e+07 | 1.66e-01 | 4.54e+07 | 2.13e-01 | 4.50e+07 | 2.62e-01 |
| 11 - 12 | 1.74e+07 | 1.43e-01 | 1.77e+07 | 8.30e-02 | 4.56e+07 | 1.12e-01 | 4.59e+07 | 1.39e-01 |
| 12 - 13 | 1.70e+07 | 8.42e-02 | 1.68e+07 | 4.74e-02 | 4.59e+07 | 6.14e-02 | 4.58e+07 | 7.90e-02 |
| | North Arm | | | | | | | |
| 1 - 2 | 1.45e+10 | 2.73e+01 | 1.44e+10 | 2.56e+01 | 1.48e+10 | 2.13e+02 | 1.46e+10 | 2.16e+02 |
| 2 - 3 | 2.83e+10 | 1.17e+00 | 2.84e+10 | 1.10e+00 | 2.86e+10 | 4.42e+00 | 2.85e+10 | 4.50e+00 |
| 3 - 4 | 7.14e+09 | 6.06e-01 | 7.16e+09 | 5.47e-01 | 7.17e+09 | 1.95e+00 | 7.16e+09 | 2.01e+00 |
| 4 - 5 | 1.31e+09 | 7.06e-01 | 1.32e+09 | 6.09e-01 | 3.86e+09 | 7.09e-01 | 3.85e+09 | 7.43e-01 |
| 5 - 6 | 3.09e+08 | 8.69e-01 | 3.09e+08 | 7.12e-01 | 9.04e+08 | 8.15e-01 | 9.03e+08 | 8.72e-01 |
| 6 - 7 | 8.80e+07 | 1.08e+00 | 8.75e+07 | 8.48e-01 | 2.60e+08 | 9.51e-01 | 2.61e+08 | 1.04e+00 |
| 7 - 8 | 3.06e+07 | 1.28e+00 | 3.00e+07 | 9.57e-01 | 8.72e+07 | 1.10e+00 | 8.56e+07 | 1.26e+00 |
| 8 - 9 | 3.03e+07 | 5.84e-01 | 3.02e+07 | 4.07e-01 | 3.29e+07 | 1.26e+00 | 3.31e+07 | 1.44e+00 |
| 9 - 10 | 1.70e+07 | 5.12e-01 | 1.74e+07 | 3.27e-01 | 4.02e+07 | 4.82e-01 | 4.10e+07 | 5.60e-01 |
| 10 - 11 | 1.76e+07 | 2.58e-01 | 1.72e+07 | 1.63e-01 | 4.16e+07 | 2.33e-01 | 4.05e+07 | 2.91e-01 |
| 11 - 12 | 1.70e+07 | 1.47e-01 | 1.72e+07 | 8.52e-02 | 4.59e+07 | 1.12e-01 | 4.60e+07 | 1.39e-01 |
| 12 - 13 | 1.70e+07 | 8.42e-02 | 1.70e+07 | 4.70e-02 | 4.60e+07 | 6.12e-02 | 4.65e+07 | 7.77e-02 |

$\pi$ contributions at low reconstructed transverse momentum, where some $\pi$ occassionally punch through and are almost correctly reconstructed. Therefore their contributions are largest for the corresponding charges. The fraction of actual punch-through hadrons being nearly correctly reconstructed is more clearly visible when plotted for separate generated transverse momentum bins, where the corresponding peaks are visible. From those plots, one can also identify the lowest generated transverse momenta to create the bulk of the falsely reconstructed high momentum muon candidates. The lowest transverse momentum bin between $1 < p_T < 2\,\mathrm{GeV}/c$ contributes around 70-75% of the background, the next bin contributes another 10-15% and the remaining 5-10% comes from all other generated transverse momenta. The reason for this behaviour originates in the steep fall-off of the hadron cross sections as shown in the previous subsection as the chance of surviving all absorbing material stays nearly the same or only increases slightly close to the actual transverse momentum.

## 4.7 Reliability of the simulations and comparison to data

The signal, muonic background simulations as well as the single hadron simulations were then combined by weighting them according to their cross sections and generated event numbers and compared to the Run 2013 data distributions. The initial distributions using basic cuts are displayed in Figure 4.6 as a function of the reconstructed transverse momentum for the two arms and charges. At this cut

level, the muon yields are largely dominated by the falsely reconstructed hadrons. At present, the data was only luminosity normalized. Some overestimation of the data by the simulations is therefore expected due to efficiencies.

# 5 Signal Extraction

The $W$ analysis strategy used to extract the signal to background ratio and calculate the asymmetry is basically composed of four major phases as shown in the chart in Figure 5.1.

Note that in chapters 5 and 6 the the abbreviation PDF stands for Probability Distribution Function, unlike to Parton Density Function in the previous chapters.

The first step is to identify the kinematic variables which are sensitive to signal and background, apply basic cut and construct probability density functions (PDFs). The second phase is called Likelihood-based pre-selection phase. At this stage, for every event which passed the basic cut, the likelihood ratio of an event to be signal event ($W^{\pm} \rightarrow \mu^{\pm}$) called $Wness$ is calculated. The $Wness$ is then used to identify events with high likelihood (high Wness) as signal candidates for further analysis in the next stage.

In the third stage, a technique called Extended Unbinned Maximum Likelihood Fitting (EUMLF) is used to calculate the signal to background ratio. This technique uses new uncorrelated sensitive kinematic variables distributions of the signals and background. The sum of the signal distribution and background distribution is tuned to fit the actual Run 2013 data in the high $Wness$ region. Finally at the fourth phase, the raw asymmetry of the signals is calculated and corrected by the signal to background ratio.

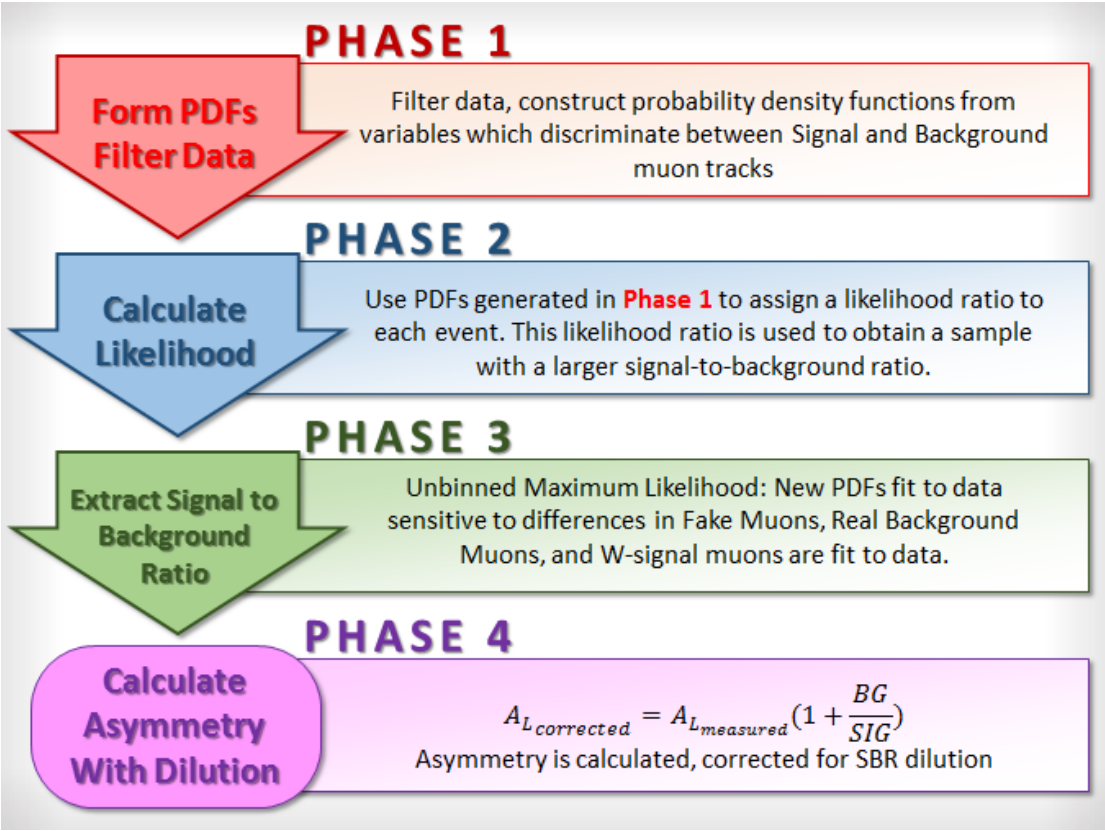



Figure 5.1: Run 2013 $W \rightarrow \mu$ analysis strategy

The goal in this chapter is to introduce the sensitive kinematic variables, calculate $Wness$ and extract the signal to background ratio (phases 1,2,3). Different statistical tools are used to minimize backgrounds while keeping the signal efficiencies high. The signal to background ratio found in this chapter will be used to correct the asymmetry which will be calculated in the next chapter (phase 4). Most of the discussions in this chapter are extracted from our analysis note (an1195) which is approved and internally published in PHENIX [54].

## 5.1 Kinematic variables and basic selection criteria

A brief summary of the kinematic variables relevant to this analysis are given in Table 5.2. Detectors FVTX, MuTr, MuID and RPC are capable of constructing their own track path of a particle from the collision vertex. Most of the variables considered are related to a measure of the degree of matching of a track from one detector to another detector or to vertex. In addition to describing the matching between the detectors tracks, $DG0$, $DDG0$, $DCA_r$, $DCA_z$,$FVTX_{dr}$, $FVTX_{d\theta}$, $FVTX_{d\phi}$ and $RpcDCA$ variables reflect the effect of multiple scattering in hadron absorbers and MuID absorbers. $DCA_r$ and $DCA_z$, which are related to decay position, are used to select event tracks originating from the interaction point or on the beam axis.

Table 5.1: Definition of the main Muon Tracker and Muon Identifier related kinematic variables used in this analysis.

| Variable | Definition |
|---|---|
| $DG0$: | distance between the projected MuTr track and the MuID road at the gap 0 $z$ position in cm. |
| $DDG0$: | deviation of the slopes of the MuTr track and the MuID road at the gap 0 $z$ position in degrees. |
| $\chi^2$: | Track fit quality which describes the quality of the fit to the MuTr and MuID hits. |
| $DCA_z$: | closest distance of approach to the vertex position as extracted using the BBC vertex after projecting the muon track back towards the vertex position. This DCA is the absolute difference of the $z$ positions of vertex and projected track in cm. |
| $DCA_r$: | closest distance of approach to the vertex position as extracted using the BBC after projecting the muon track back towards the vertex position. This DCA is the absolute difference of the radius of the projected track in cm. |
| $\Delta\phi_{12}$: | Azimuthal angle difference between between |
| $\Delta\phi_{23}$: | Azimuthal angle difference between between the MuTr stations 2 and 3 in radians. |
| $dw_{23}$: | Reduced azimuthal bending angle - the magnitude of this variable corresponds to the bending of the $\mu$ track in the muon arms in the $\phi$ direction. It is defined as $dw_{23} = p_T sin(\theta)(\Delta\phi_{23}\ )$ |

Table 5.2: Definition of the RPC and FVTX related kinematic variables used in this analysis.

| Variable | Definition |
|---|---|
| $Rpc1(3)DCA$: | transverse distance between the muon tracks' position at Station 1(3) projected on to the RPC1(3) $z$ position in cm. |
| $FVTX_{d\phi}$: | Phi residual between MuTr and FVTX track |
| $FVTX_{d\theta}$: | Theta residual between MuTr and FVTX track |
| $FVTX_{dr}$: | Radius residual between MuTr and FVTX track |
| $FVTX_{cone}$: | Number of FVTX clusters inside a cone around the track defined by 0.04rad $<$ dR $<$ 0.52rad, where $dR = sqrt(d\eta^2 + d\phi^2)$ |

For rough identification of muons, we apply basic cuts on the signal sensitive variables. The signal events, $W^{\pm} \rightarrow \mu^{\pm}$, are required to have a single track muon with high-$p_T$ in the event. The muons are typically identified by their deep penetrating property through matter than hadrons. So we require last gap hit in the MuID as hadrons ($K^{\pm}, \pi^{\pm}$) are rare to survive to the last gap through hadron absorbers at the Central Magnet and the MuID steel walls. Also some track qualities are required. We typically require

- Last MuID gap has to be gap 4 to ensure muons penetrating through all MuID steel
- high transverse momentum requirement: 16 GeV/$c$ < $p_T$ < 60 GeV/$c$
- maximum momentum $p < 250\,\mathrm{GeV}/c$ which is the maximum possible physical energy
- $\chi^2 < 20$ to require only reasonably constructed tracks
- $DG0 < 20\,\mathrm{cm}$.
- $DDG0 < 9\,\mathrm{degrees}$.
- single track candiate in one event.

The above set of requirements are called the *basic cut* in this analysis. After applying basic cuts, backgrounds will be further reduced via likelihood method which will be discussed in the later sections.

Another important factor to consider while selecting variables is the correlation among themselves. The correlation between important sensitive variables is shown in Figure 5.2.

## 5.2 W likelihood ratio extraction and background estimation

After applying basic cuts on the signal and background data sets, the probability of an event to be signal event ($W^{\pm} \rightarrow \mu^{\pm}$) has been determined by analyzing

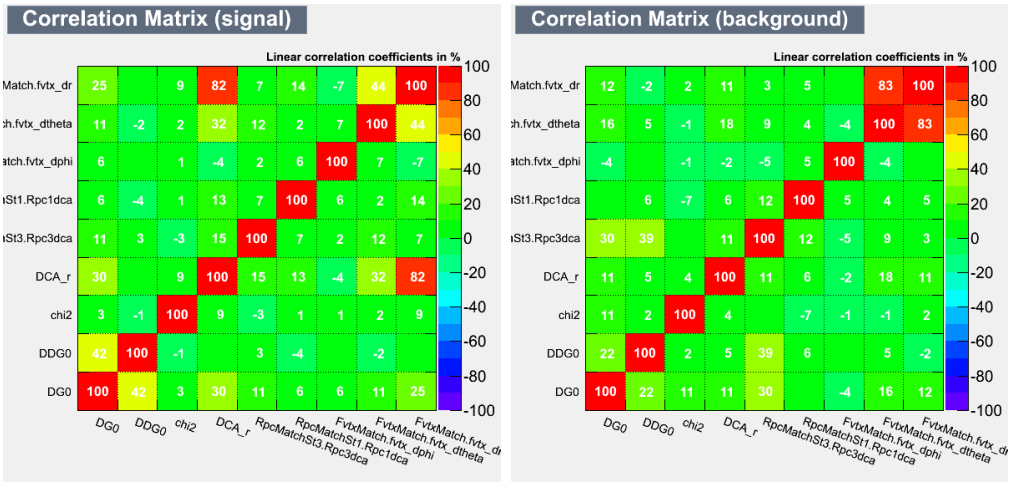



Figure 5.2: Correlation coefficient between kinematic variables used for signal extraction. The left panel is simulated signal while the right panel show the data.

distribution of the selected variables. Such likelihoods are extracted as a function of DG0, DDG0, DCAr, Rpc1DCA, RPC3DCA, the track reconstruction $\chi^2$, and the FVTX matching variables $FVTX_{d\phi}$, $FVTX_{dr}$ and $FVTX_{d\theta}$ and the FVTX cone multiplicity, $FVTX_{cone}$. To maximize the background in the real data and in the muon candidates the likelihoods have been determined by applying the basic cuts and requesting at least a hit in the RPC1 or RPC3 station. Similarly, since the FVTX covers only a small part of the forward muon arms, the FVTX matching variables have been used only for those events when a good FVTX and MuTr track match is available. The signal likelihood, $\lambda_{sig}$, has been determined using a Pythia event generator and GEANT based PHENIX Detector Simulation Package (Monte Carlo simulation) of $W^{\pm}(Z) \rightarrow \mu^{\pm}$, described in section 4.5.

The likelihood for the background, $\lambda_{bg}$, has been extracted from data. There

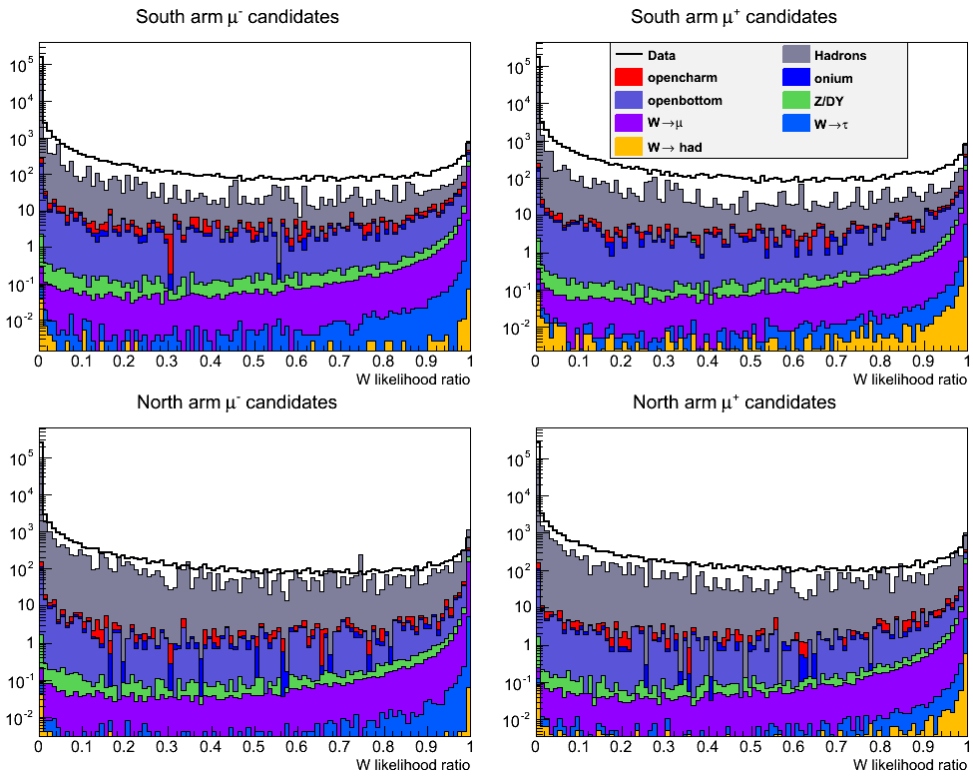



Figure 5.3: Signal (purple), Z/DY (green), open charm (red), onium (blue), open bottom (dark blue) and hadronic (grey) distributions as function of a given W likelihood ratio (Wness).

is only a small fraction of signal ($\sim 1\%$) in the muon samples which passed the basic cut, and does not significantly change the background distributions.

Once the signal and the background likelihood have been determined, a new variable $W$ likelihood ratio (Wness) is defined:

$$f = \frac{\lambda_{sig}}{\lambda_{sig} + \lambda_{bg}}. \tag{5.1}$$

As the likelihoods, $f$ depends on the variables DG0, DDG0, DCAr, Rpc1DCA, RPC3DCA, $\chi^2$, and the FVTX matching variables (whenever they are available). According to the definition, background events dominate in the low-$f$ region, while the signals are mainly located near $f \sim 1$. Therefore, $f$ represents a high-efficiency cut parameter to reject background and enhance muons from $W$ decay .

The correlations between the variables upon which $f$ depends are summarized in Figure 5.2. As DG0 and DDG0 are correlated, a two-dimensional propability density function for these two variables was calculated while the other variables can be obtained via individual propability density functions.

The $W$ likeliness ratios distributions $f$ are shown in Figure 5.3. As expected, the backgrounds are located at lower $f$, the real muon backgrounds are slightly more evenly distributed and the $W$ signal are contributing a higher fraction at high likelinesses. The corresponding relative distributions can be seen in Figure 5.4. One clearly sees again, that selecting higher likeliness values enhances the relative signal fraction.

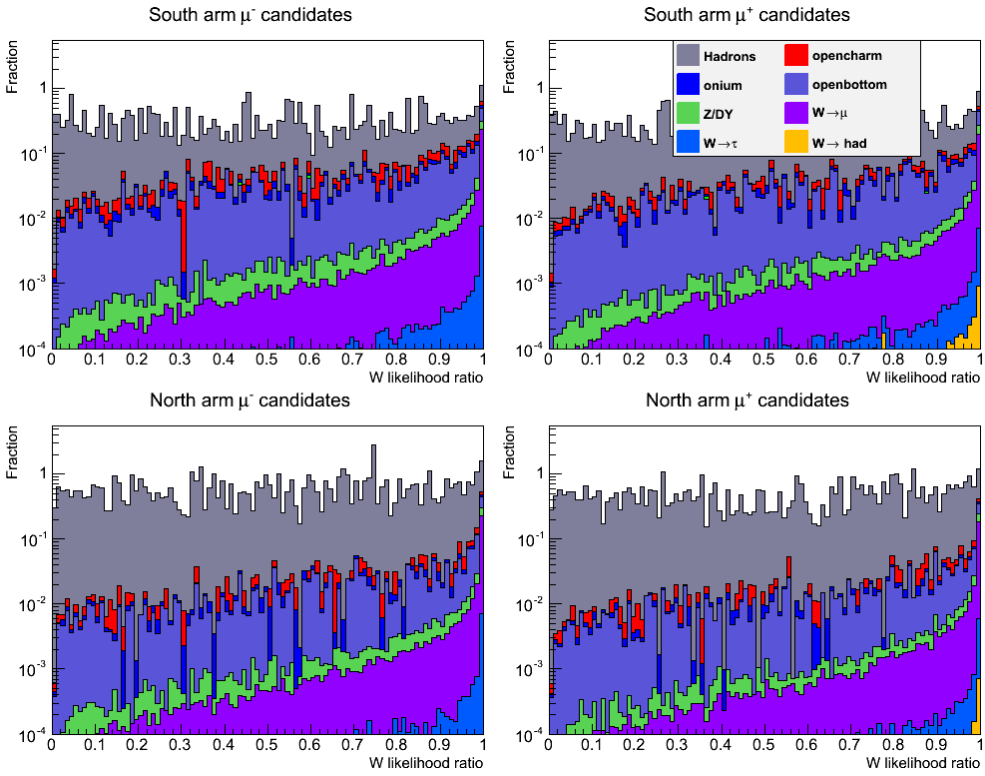



Figure 5.4: Signal (purple), Z/DY (green), open charm (red), onium (blue), open bottom (dark blue) and hadronic (grey) relative fractions as function of the minimum $W$ likelihood ratio $f$. As normalization reference the total data was taken after including efficiencies in the simulations (such as trigger and RPC efficiencies).

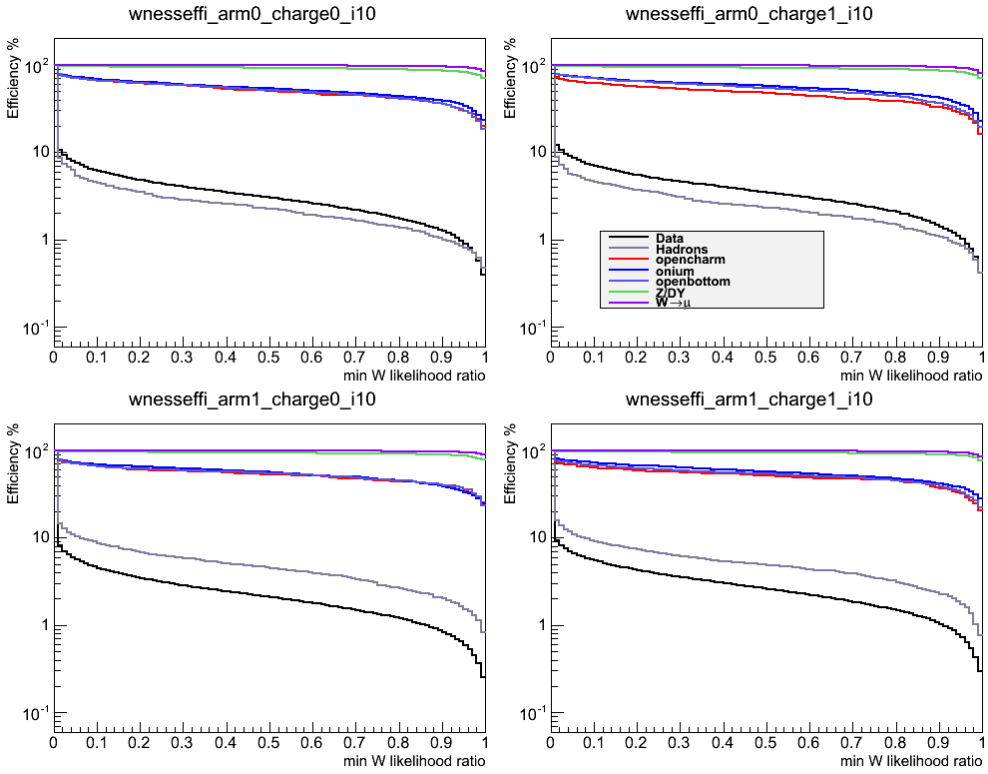



Figure 5.5: Signal (purple), Z/DY (green), open charm (red), onium (blue), open bottom (dark blue), hadronic (grey) and real data (black) efficiencies as function of the minimum $W$ likelihood ratio $f$. The top left represents negative muons in south arm, top right represents positive muons in south arm, bottom left represents negative muons in north arm and bottom right represents positive muons in north arm.

In addition the signal and background efficiencies are displayed in Figure 5.5 as a function of the minimum $f$ value. The background efficiencies rapidly drop for nonzero $Wness$ values and continue to decrease more rapidly than the the signal efficiencies. The muon background efficiencies, mostly dominated by lower transverse momenta smeared into the high momentum region also decrease slightly faster than the signal efficiencies.

The $f$ distributions extracted for signal and backgrounds have been cross checked by all Run 2013 analyzers. After a few iterations the initially selected event numbers are similar among analyzers. The extracted likelihood ratio distributions are in good agreement as can be seen in Figure 5.6 and Figure 5.7.

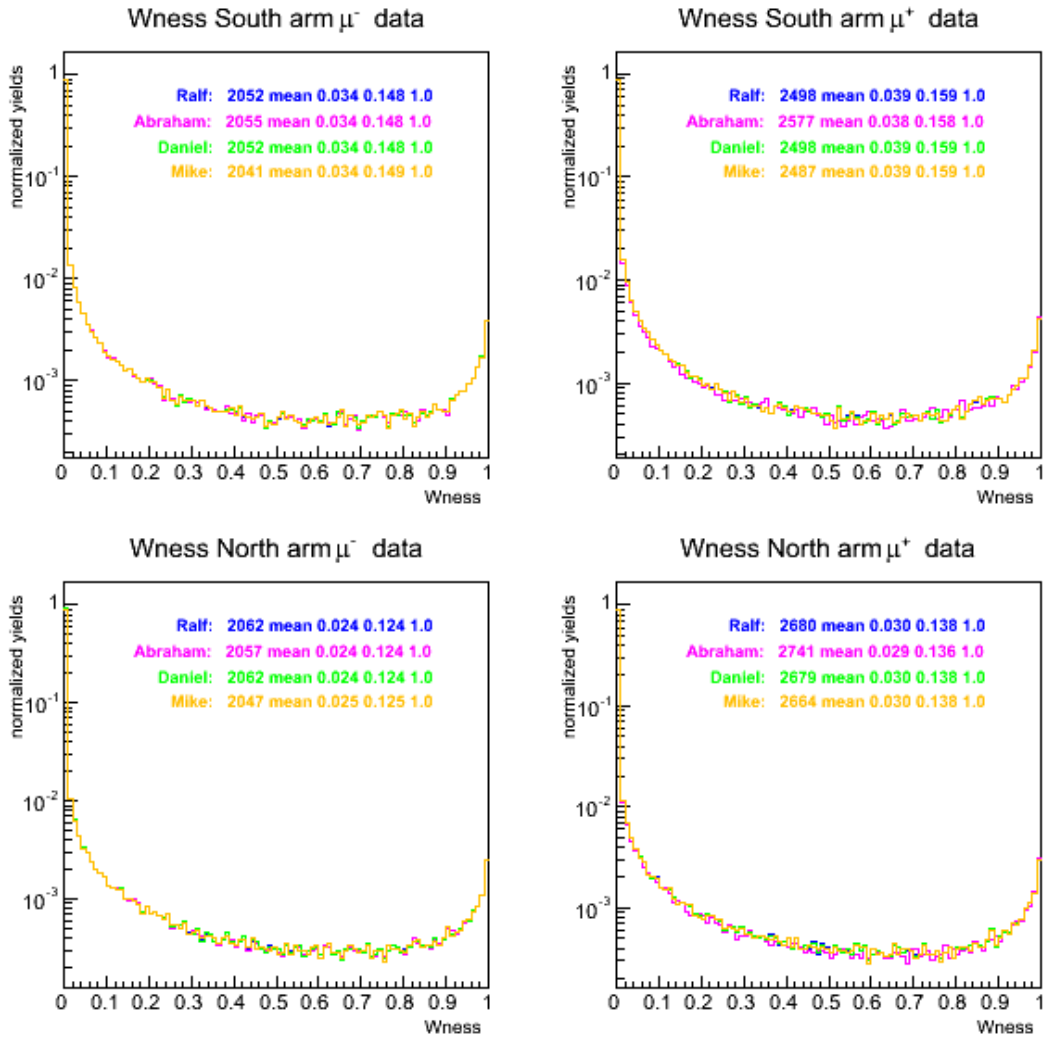



Figure 5.6: W likelihood ratio $f$ of data distributions from the determination from different analyzers for different arms and charges.

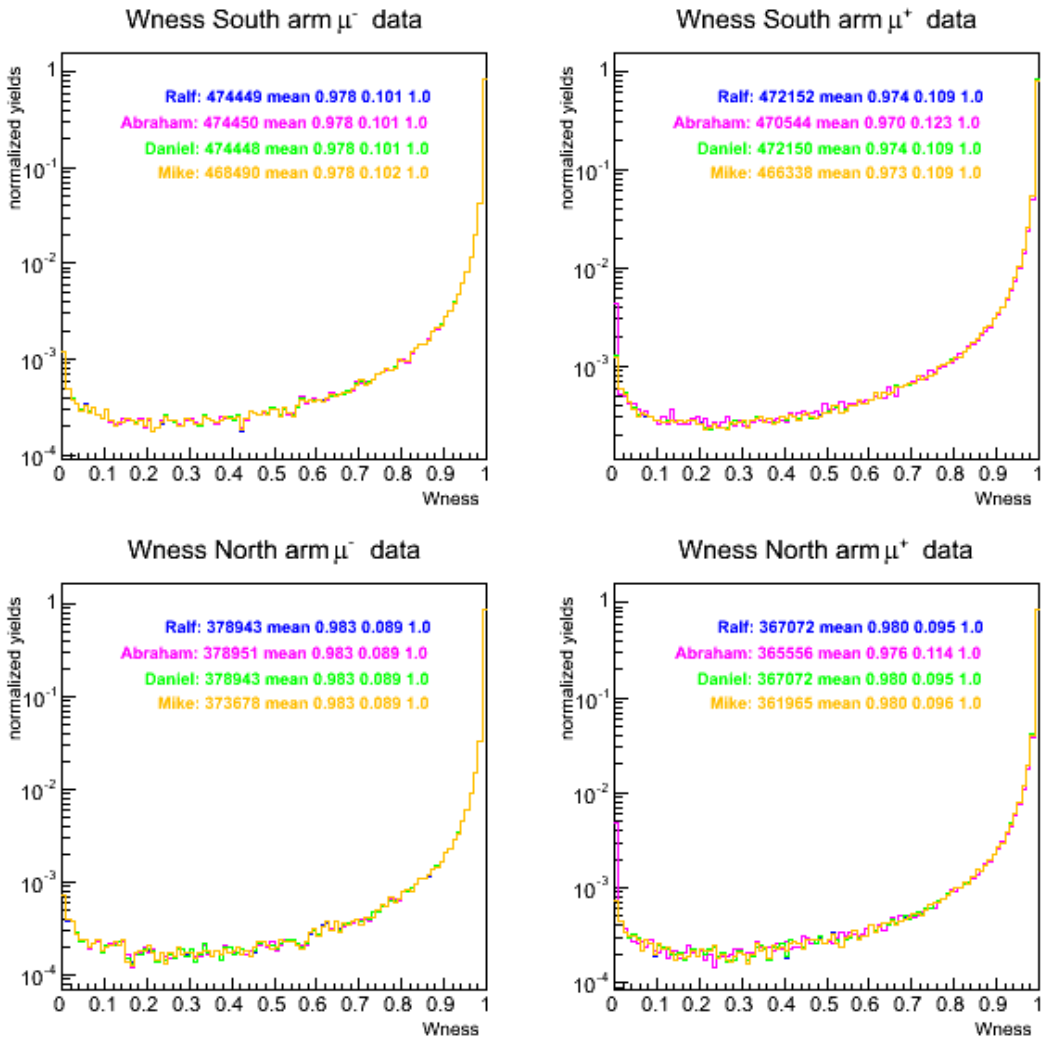



Figure 5.7: W likelihood ratio $f$ of signal simulation distributions from the determination from different analyzers for different arms and charges.

## 5.3 W likelihood ratio of valid FVTX events

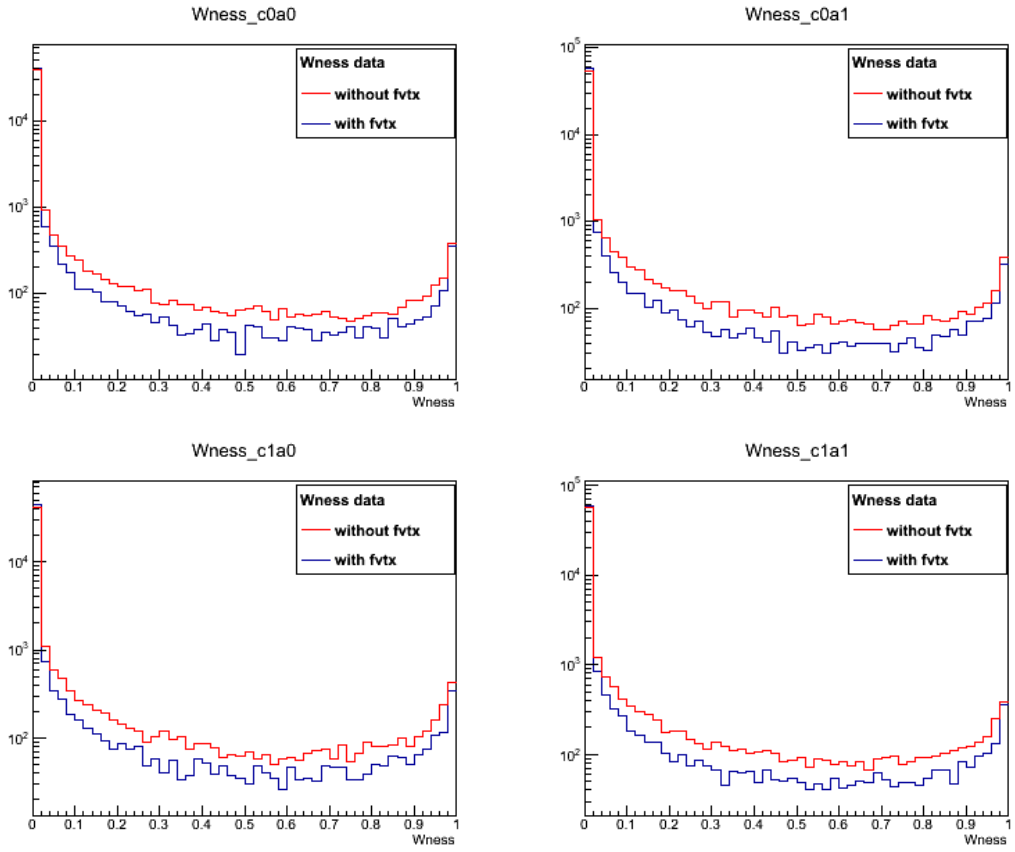



Figure 5.8: $Wness$ distributions of data for valid FVTX events. Red is $Wness$ without FVTX information and blue is including FVTX information. The top left represents negative muons in south arm, top right represents positive muons in south arm, bottom left represents negative muons in north arm and bottom right represents positive muons in north arm.

The FVTX variables selected to be used in $W$ likelihood ratio ($Wness$) calculation are $FVTX_{d\phi}$, $FVTX_{dr}$, $FVTX_{d\theta}$ and $fvtx_cone$. Their definition is given in Table 5.2. In this analysis, only some of the events have FVTX track matched

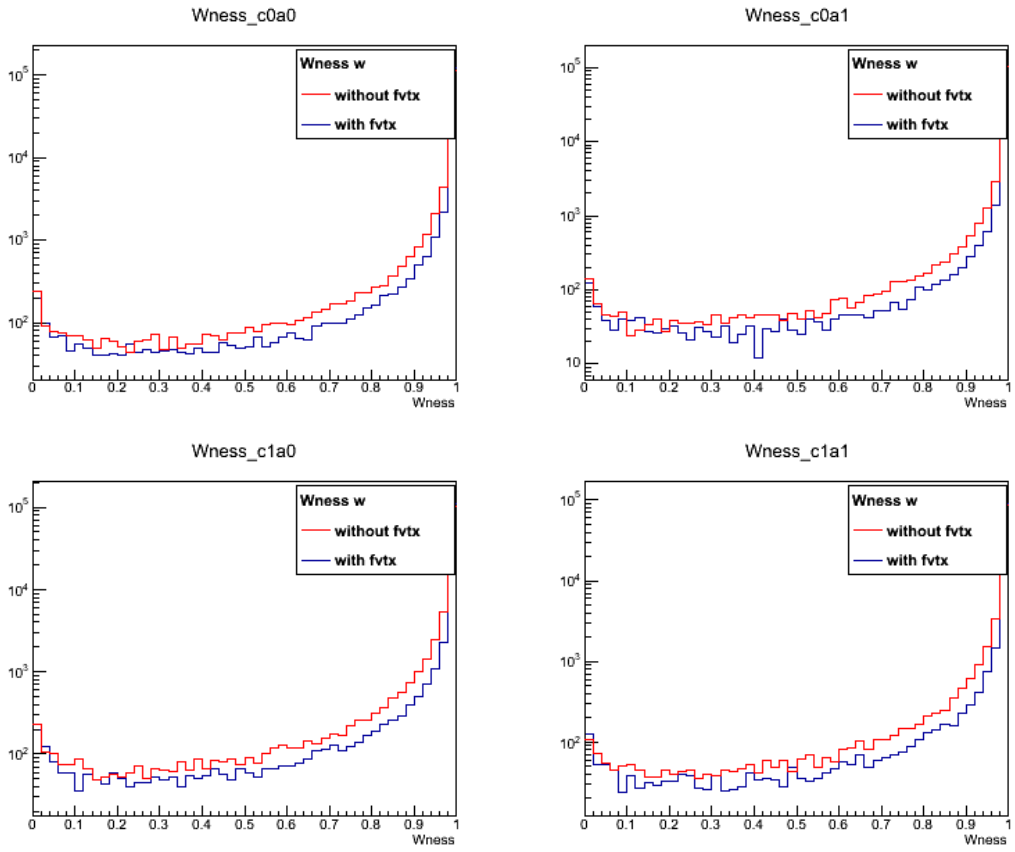



Figure 5.9: *Wness* distributions of data for valid FVTX events. Red is *Wness* without FVTX information and blue is including FVTX information. The top left represents negative muons in south arm, top right represents positive muons in south arm, bottom left represents negative muons in north arm and bottom right represents positive muons in north arm.

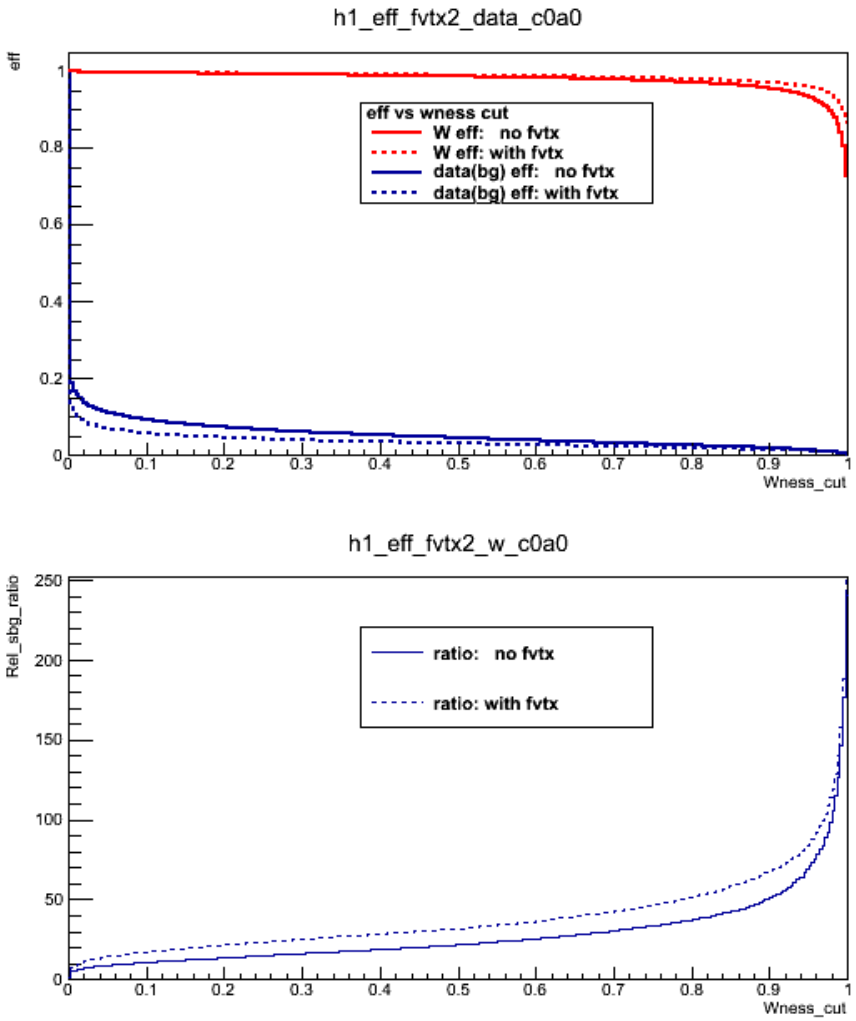



Figure 5.10: Top plot shows $W$ efficiency (red) and data efficiency (blue) as function of minimum $Wness$ cut for negative charge and south arm case. The dotted line represent "with FVTX" case and the solid line represents "without FVTX" case. Bottom plot shows "relative signal to background ratio". The dotted line represents "with FVTX" and the solid line represents "without FVTX".

with muon tracker's track. These events are called valid FVTX events. After basic cut, in data, 220245 events out of 952118 are considered as FVTX valid tracks ($\sim$ 23%). Similarly, in $W$ simulation, 457864 events out of 1780676 are considered as FVTX valid tracks ($\sim$ 26%). Whenever there is valid FVTX event , the above FVTX variables in addition to muon tracker and RPC variables are used in calculating $Wness$.

Figure 5.8 and Figure 5.9 show $Wness$ distribution of these selected events in two cases. The red one shows, the $Wness$ calculated "without FVTX" information (only muon tracker and RPC variables used). The blue one shows $Wness$ calculated "with FVTX" information (muon tracker, RPC and FVTX variables used). One can see from this figure that some events migrate to higher $Wness$ (in $W$ signal case) and some migrate to lower $Wness$ region (in background case). The top plot of Figure 5.10 shows $W$ efficiency (red) and data efficiency (blue) as function of minimum $Wness$ cut for negative charge and south arm case. The dotted lines ("with FVTX") are above the solid lines ("without FVTX") for $W$ efficiency case and vice versa for the data efficiency case. At the bottom plot, the ratio of $W$ efficiency to *data* efficiency which is the "relative signal to background ratio" is shown. The dotted line, which represents "with FVTX", shows higher "relative signal to background ratio" than the solid line which is "without FVTX".

Another, but may not be the efficient way of background rejection is successive

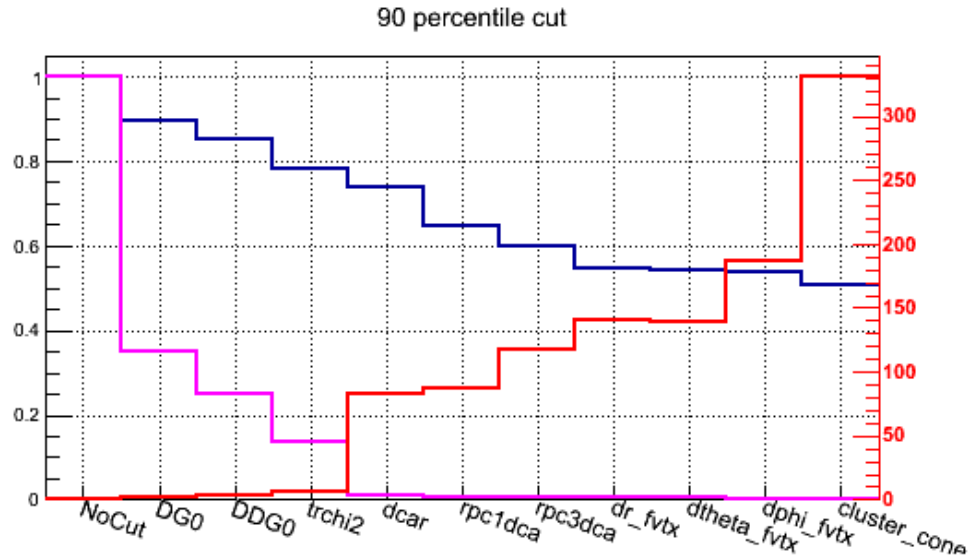



Figure 5.11: Successive cuts for negative charge and south arm case. The left vertical axis shows the fraction of signal (blue) and background (magenta) remaining at each stage of successive cuts. The vertical axis at the right side (red scale) shows the relative ratio of signal and background fractions.

cut method. However, it would give us some idea about the sensitivity of our variables to data and background events. It is also an alternative tool to cross check or compare with the likelihood method. In the successive cut method, we study $W$ simulation at lower transverse momentum ($16 < p_T < 17$ GeV/C) where there is much statistics. In this $p_T$ range, we determine the DG0 cut which keeps 90% of the entire signal. Similarly, we continue determining the cut points for DDG0, DCAr, Rpc1DCA, RPC3DCA, $\chi^2$, $FVTX_{d\phi}$, $FVTX_{dr}$, $FVTX_{d\theta}$ and $FVTX_{cone}$. Then we apply these cuts one after the other to the entire ($16 < p_T < 60$ GeV/C) data and also to the entire $W$ simulation. Good variable cuts should be able to cut away more background but fewer signal. The

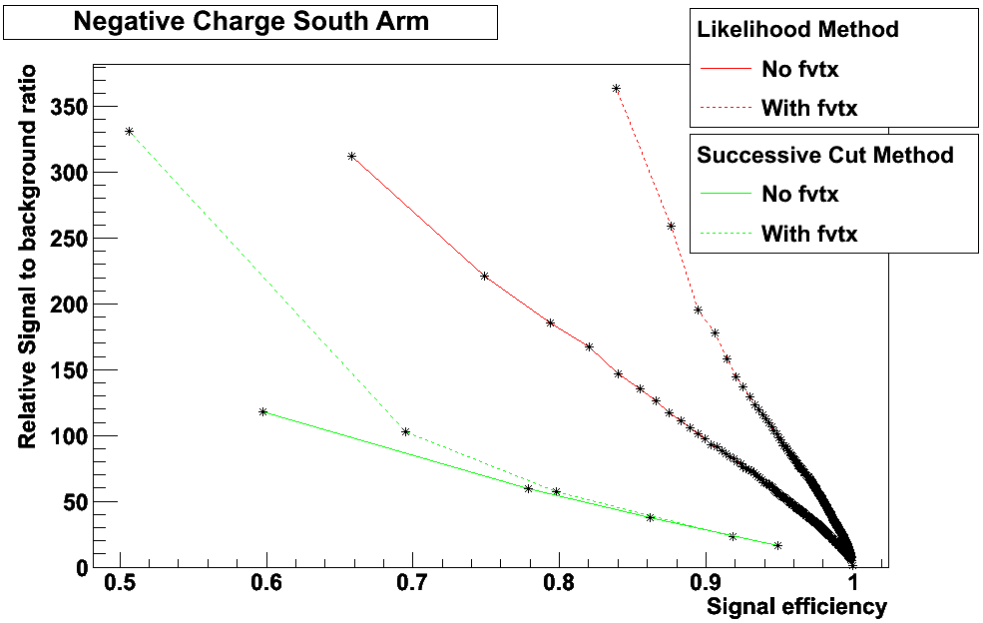



Figure 5.12: Relative background rejection versus signal efficiency for negative charge and south arm case. The red lines are from likelihood method, whereas the green lines are from successive cut method. In both cases, the solid line represents the result "without FVTX" and the dotted line represents "with FVTX".

left vertical axis of Figure 5.11 shows the fraction of signal (blue) and background (magenta) remaining at each stage of successive cuts. The vertical axis at the right side (red scale) shows the relative ratio of signal and background fractions. The cuts shown at the horizontal axis begin with No Cut, where we have the entire data and $W$ simulation events. The last four cuts are from FVTX. The successive cut plot shows us which variables have higher relative background rejection power with their corresponding capability of preserving signals. Even after we applied cuts from MuTr and RPC, the FVTX variables cuts are able to reject more background events and lose only few $W$ simulation events. Note that, the plot considers only FVTX valid events. And, as will be shown in Figure 5.12 the successive cut method is less efficient than the likelihood method.

To analyze the effect of FVTX variables in terms of improving signal efficiency and background rejection, Figure 5.12 Shows relative background rejection versus signal efficiency. The solid red line (ratio without FVTX) and the dotted red line (ratio with FVTX) are from likelihood methods used in this analysis. The relative background rejection is extracted from horizontal axis of the bottom plot of Figure 5.10 and the $W$ efficiency is extracted from the vertical axis of the top plot of Figure 5.10 which is shown in red. The solid green line is the ratio without FVTX and the dotted green line is the ratio with FVTX. Both are summarized from successive cut method for different $W$ efficiencies. In both methods, only those FVTX valid events are studied. At a given $W$ efficiency the FVTX variables

improved the relative signal to background ratio especially at lower $W$ efficiency region, which is equivalent to higher $Wness$. As we go to lower $W$ efficiency region the relative signal to background ratio increases. But we should be careful that this is so at the expense of signal efficiency. Another important observation from this plot is that, the likelihood (red) method is consistent and even more optimized way of using our variables than successive cut method (green).

Care should be taken that the events considered here are only FVTX valid events which is about 23% of entire data sample. The improvement in relative signal to background ratio shown above will be diluted when we use the entire data. Most of the improvements are contributed by $FVTX_{cone}$ cut. The possible reasons for relatively lower contribution from the matching variables could be the correlation between the FVTX variable with the MuTr DCA variable.

### 5.4 Signal to background ratio extraction

After applying the basic cuts and high $Wness$ requirements to select signal region, our data is now reduced to a sample with more fraction of signal. The primary challenge of this analysis is the relatively low abundance of $W \to \mu$ events. We count muons $W \to \mu$ for asymmetry calculation, however, there still are much more muons from background events which enter into our reckoning of the total number of $W \to \mu$ events which will dilute the asymmetry. Therefore we must try to reduce backgrounds as much as possible and determine the signal to background

ratio as a means of correcting for this dilution.

We use an Extended Unbinned Maximum Likelihood Fit (EUMLF) in order to estimate the ratio of $W \rightarrow \mu$ events to background events. The EUMLF is used with the number of data events, $N$, which is large, and the subset number of signal events, $n$, often fill only one bin. A detailed presentation of the method, why it works, and how goodness of any fit may be evaluated can be found in references [92].

For EUMLF, to gain more information about our data sets, we introduce new variables which are not correlated with those used in $Wness$ calculations. We also require these new variables not to be correlated to each other. The reduced azimuthal bending of a track trajectory as it crosses Station-2 and Station-3 of MuTr (also called $dw_{23}$) and pseudorapidity $\eta$ have been good candidate variables to the above criteria. Figure 5.13 shows a two dimensonal $\eta$ vs $dw_{23}$ distrbution (one can see they are not correlated) and 1D $\eta$ and $dw_{23}$ distrbutions separately.

The signal $\eta$ and $dw_{23}$ PDFs used in Figure 5.13 and later for EUMLF have been extracted from the simulations discussed in section 4.5. Similarly, the distribution for muonic background cocktails discussed in Table 9 of section 4.5 are added together, by weighting for luminosity, cross section and dimuon factor. We assume a total machine luminosity of $277pb^{-1}$ as obtained from the pile-up corrected BBC novtx rates discussed in section 4.2. Detailed discussion of determining those factors is also discussed in our analysis note[54]. Table 5.3 summarizes

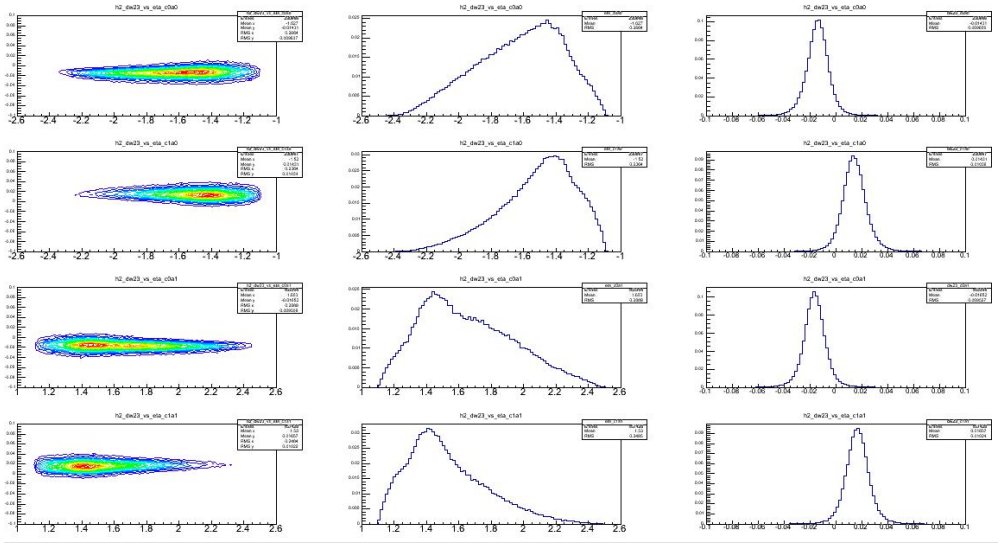


Figure 5.13: Distributions and PDFs for $W/Z \rightarrow \mu$ events extracted from simulation: $\eta$ versus $dw_{23}$ distributions (left column), $\eta$ PDF (middle column) and $dw_{23}$ PDF (right column). The first row represents negative muons in south arm, the second row for positive muons in south arm, the third row for negative muons in north arm and fourth row for positive muons in north arm.

the final yield of muonic background events after applying the correction factors.

The hadronic $\eta$ and $dw_{23}$ PDFs used in Figure 5.14 and later for EUMLF have been extracted from real data distribution by analysing its pattern at lower $Wness$ region (Wness $< 0.9$) as the data is largely dominated by hadron backgrounds. The hadronic $\eta$ distribution is similar for different $Wness$ ranges as shown in run 2011 analysis[89] and it is safe to represent the hadronic $\eta$ PDF by the real data $\eta$ PDF for $Wness < 0.9$. The $dw_{23}$ distribution however is very sensitive to Wness, in particular its width and mean value become smaller with the increase of $Wness$ as shown in the top two middle panels of Figure 5.15. The total PDF of $dw_{23}$, $p(f, dw_{23})$ which depends on $Wness$ distribution function $f$ and $dw_{23}$ is extracted

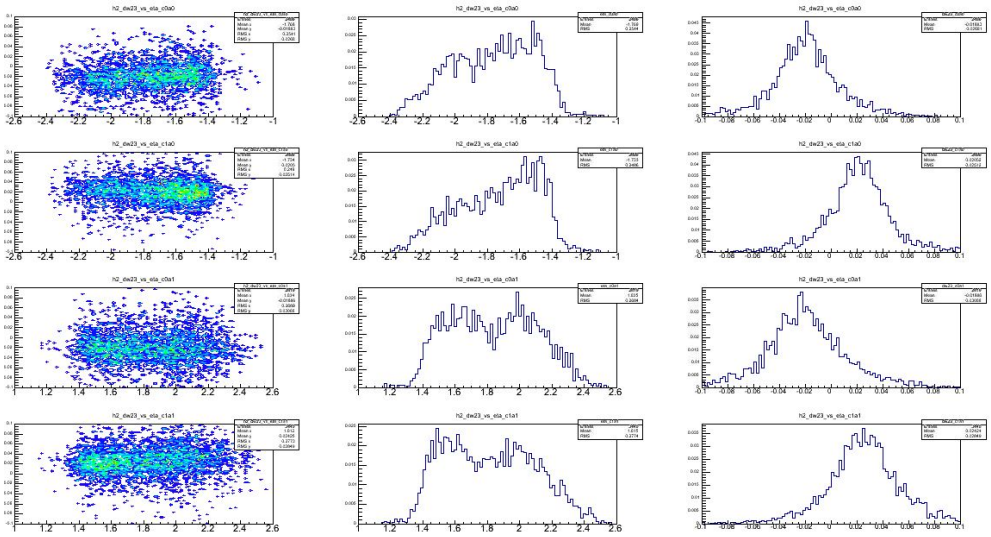


Figure 5.14: Distributions and PDF for hadron background events extracted from data: $\eta$ versus $dw_{23}$ distributions (left column), $\eta$ PDF (middle column) and $dw_{23}$ PDF (right column). The first row represents negative muons in south arm, the second row for positive muons in south arm, the third row for negative muons in north arm and fourth row for positive muons in north arm.

from the 2D $\eta$ vs $dw_{23}$ in four consequent steps as shown in the panels in the first column of Figure 5.15.

- First, the $f$ distribution, $p(f)$, is extracted fitting the 1D $f$ distribution with a $4th$-order polynomial (top-left panel in Figure 5.15);

- then, the conditional probability $p(dw_{23}, f)$ is extracted from the 1D $dw_{23}$ distributions at a given $f$, modeling the distribution with two coaxial gaussians (left columns in Figure 5.15). This conditional probability $p(dw_{23}, f)$ is extracted from data only in the region $f < 0.9$, where the background dominates, and then

Table 5.3: Muon background scaling factors used for weighting/scaling various muon backgrounds before adding to generate muon background distributions. This particular table shows values for the south arm, negative charge.

| | final yield | generatd events | luminosity correction | correction factor |
|---|---|---|---|---|
| Charm | 84.54 | 5.85e+11 | 2.23e-01 | 5.40e-01 |
| Onium | 89.16 | 1.50e+11 | 2.05e-01 | 1.90e-01 |
| direct $\gamma$ | 0.21 | 5.84e+10 | 2.08e-01 | 2.08e-01 |
| Bottom | 48.38 | 7.36e+09 | 2.26e-01 | 1.24e-01 |
| Z+DY | 87.8 | 2.93e+08 | 1.24e-02 | 1.94e-02 |
| $W \to \tau$ | 5.12 | 3.43e+08 | 1.10e-03 | 7.88e-04 |
| $W \to hadrons$ | 0.09 | 3.42e+08 | 1.11e-03 | 7.90e-04 |
| Z | 46.61 | 1.73e+08 | 4.44e-04 | 7.00e-04 |

- it is extrapolated in the region $f > 0.9$ assuming that the gaussian parameters change linearly with $f$.

- Finally, the extracted $p(f)$ and $p(dw_{23}, f)$ are combined to give the hadron background PDF $p$.

$$p = p(f) \cdot p(dw_{23}, f). \tag{5.2}$$

In our real data single muon sample, the events for the three processes (signal, muon and hadron background) are distributed according to the PDF we extracted

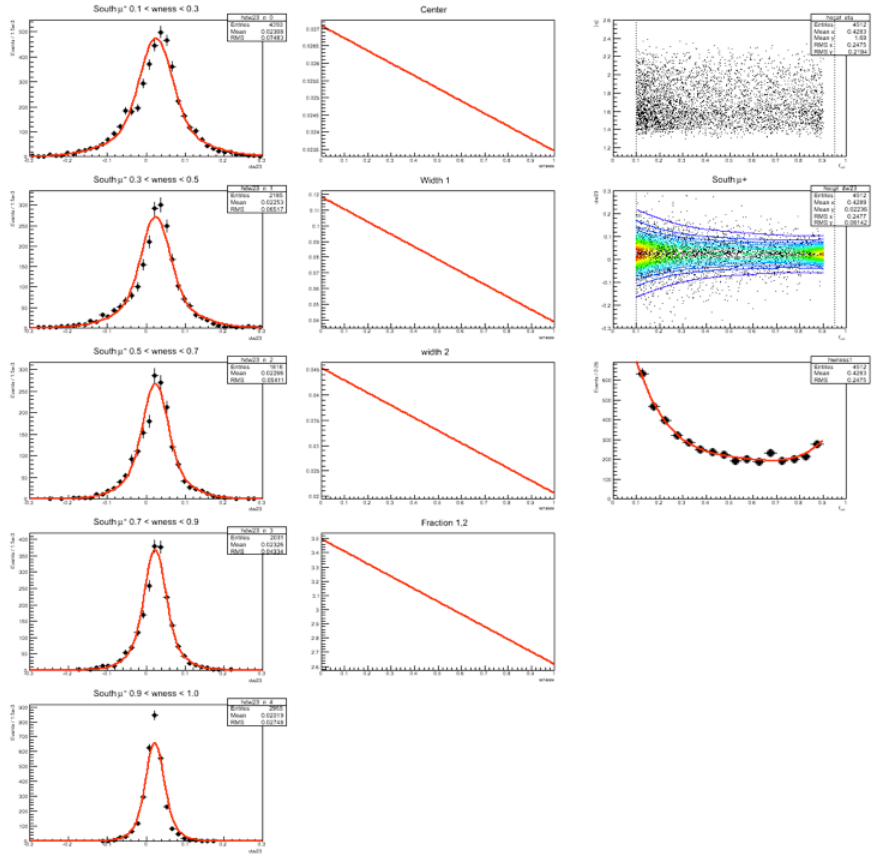



Figure 5.15: Left Column: The double gaussian $dw_{23}$ distribution from the lower $Wness$ region of data (the first four plots in red). The widths and means are extrapolated to high $Wness$ region to determine the hadronic $dw_{23}$ shape in the signal region (the fifth plot in red). Middle Column: Shown from top to bottom are Patterns of changes of the mean, Width of the first gaussian, width of the second gaussian and the coefficient factor of double gaussian $dw_{23}$ distribution as a function of Wness. Right column: Shown from top to bottom are $\eta$ vs $Wness$ distribution, $dw_{23}$ vs $Wness$ distribution and $Wness$ distribution below 0.9 fitted to fourth-order polynomial.

as described above, and that we call here:

$$p_{sig}(x_i|f_{cut}),\ p_{\mu}(x_i|f_{cut}),\ p_{had}(x_i|f_{cut}), \tag{5.3}$$

where $x_i$ is either $\eta_i$ or $dw_{23\,i}$ of the event $i$, and $f_{cut}$ specify the cut applied on the $f$ variable.

An unbinned maximum likelihood fit can then be performed to extract the number of events for each process: $n_{sig}$, $n_{\mu}$, $n_{had}$ corresponding to number of signals, number of muonic background and number of hadronic backgrounds respectively[54]. To reduce the number of parameters, we fixed the number of muon background events $n_{\mu}$ to the expected yield according to the cross section of muon background processes, and then we extracted the remaining parameters ($n_{sig}$, $n_{had}$).

Figures 5.16 to Figure 5.19 show the results of the fits of $\eta$ and $dw_{23}$ distributions for different charges and PHENIX arms, for muons with $p_T > 16$ GeV and a cut on $Wness > 0.99$. The $Wness$ cut being used in old fits for run 2012 and even for some time in Run 2013 analysis was $Wness > 0.92$. The $Wness > 0.99$ will be the new default cut for Run 2013 analysis, because we still have more statistics even for $Wness > 0.99$ (unlike to previous years' data), and we still have stable fit with lower background. In Run 2013 data we have enough statistics to divide the data sample into three $\eta$ region: $1.10 < \eta < 1.40$, $1.40 < \eta < 1.80$ and $1.80 < \eta < 2.60$.

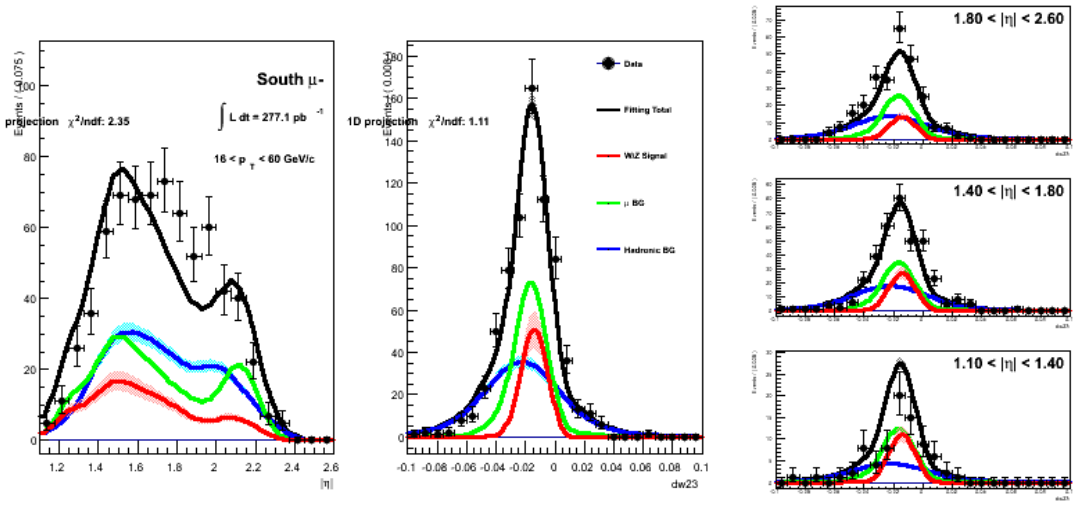



Figure 5.16: The fit results used for the signal to background ratio of negative charge muon in south arm. Each set of of plots shows the fit results for the $\eta$ distributions (left) and for the $dw_{23}$ in one-combined $\eta$ bin (middle) and the 3 $\eta$ bins mentioned in the text (right columns).

The signal and background results for $Wness$ cut of 0.99 are summarized in Table 5.4 for the above mentioned three $\eta$ bins. The tables also include the absolute uncertainties as directly obtained from the fit alone. Statistical uncertainities and other uncertainties which might need to be taken into account when assigning the systematic uncertainties of the final asymmetries are discussed in the next chapter.

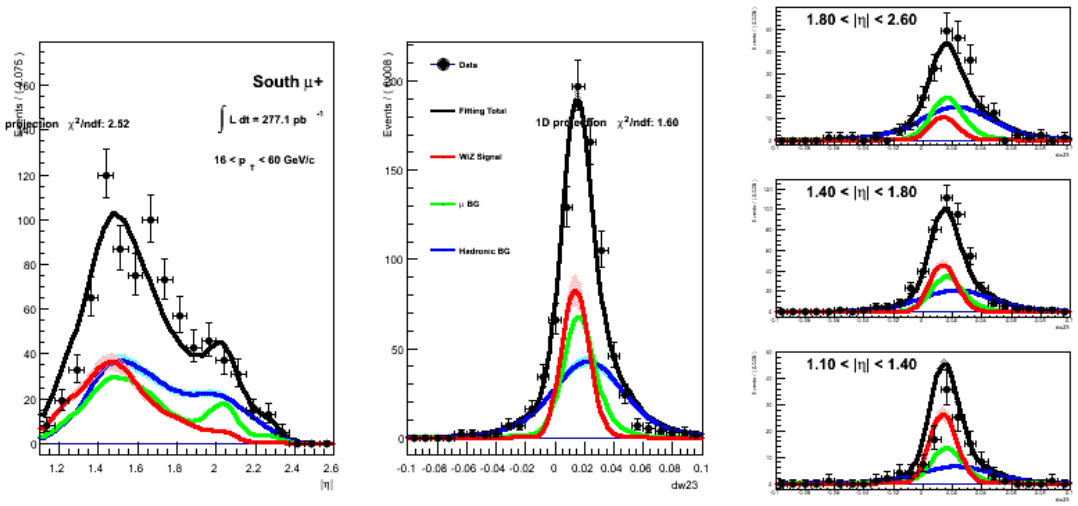



Figure 5.17: The fit results used for the signal to background ratio of positive charge muon in south arm. Each set of of plots shows the fit results for the $\eta$ distributions (left) and for the $dw_{23}$ in one-combined $\eta$ bin (middle) and the 3 $\eta$ bins mentioned in the text (right columns).

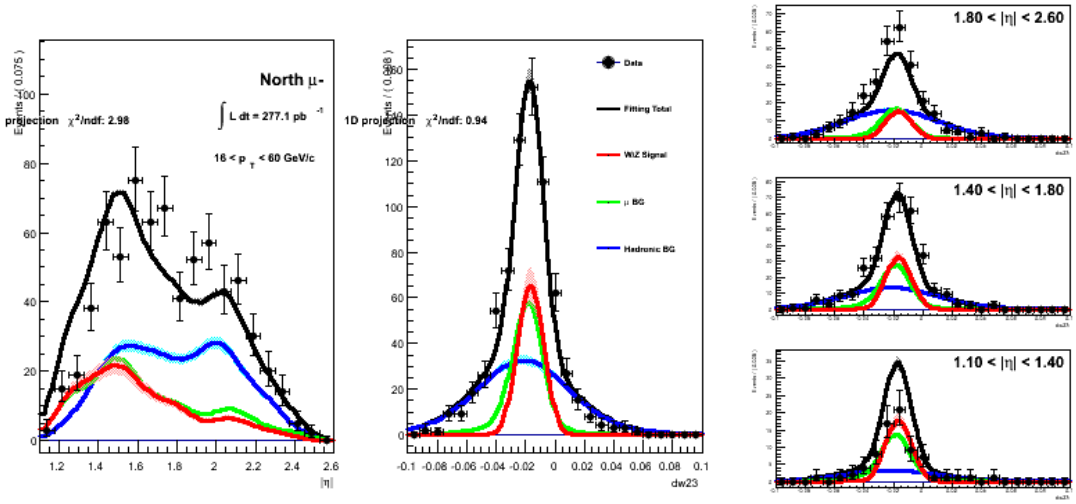



Figure 5.18: The fit results used for the signal to background ratio of negative charge muon in north arm. Each set of of plots shows the fit results for the $\eta$ distributions (left) and for the $dw_{23}$ in one-combined $\eta$ bin (middle) and the 3 $\eta$ bins mentioned in the text (right columns).

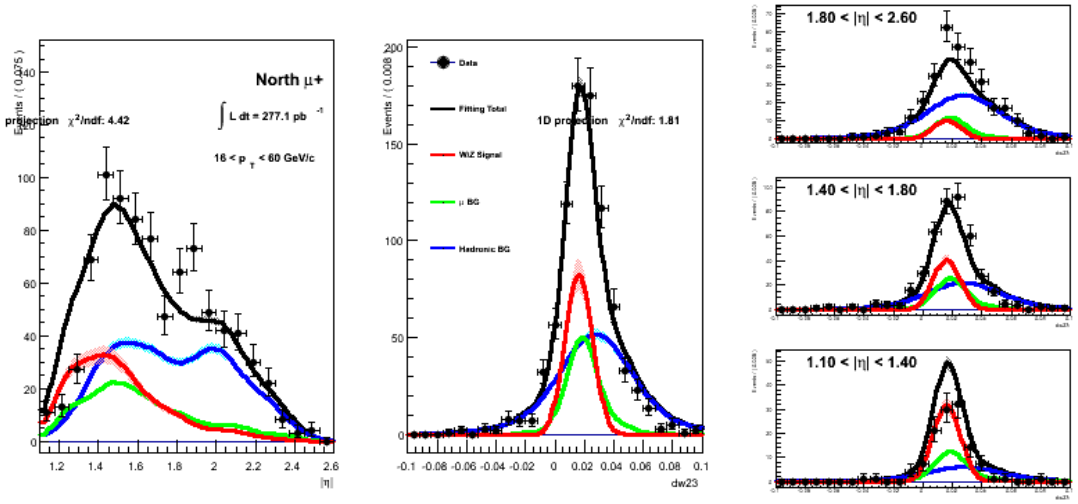



Figure 5.19: The fit results used for the signal to background ratio of positive charge muon in north arm. Each set of of plots shows the fit results for the $\eta$ distributions (left) and for the $dw_{23}$ in one-combined $\eta$ bin (middle) and the 3 $\eta$ bins mentioned in the text (right columns).

## 5.5 Fit consistency check

At each phase of the analysis, the Run 2013 analyzers Abraham Meles, Ralf Seidl, Francesca Giordano, Michael Beaumier and Daniel Jumper employed code cross check and data set cross check. The idea was that, given each analyzer's production of a tree containing data relevant to the analysis, we could determine where in the analysis chain differences enter, by comparing the extracted quantities from a given analyzer's code, including the signal to background ratio as well as the $Wness$ distributions against the same quantities generated from that analyzer's tree, but calculated with another analyzers code. One important technique employed in our analysis to test the our fitting technique is the so called PEPSI challenge (Polarized Electron Proton Simulator). It was used in the past at the HERMES experiment to check weather the analysis procedure was able to extract the already known inputs, helicities, correctly. More about PEPSI challenge can be found in EIC PEPSI page[93].

The idea of PEPSI challenge in our context is that a trial data sample will be created out of the Monte Carlo contributions (signal, muonic background and hadronic background) and therefore their actual magnitudes are known. The trial data sample is then treated identically to the procedure we followed in our analysis. The obtained fit results are then compared to the actual hadron Monte Carlo based distributions in the target $Wness$ region.

The main challenge in our analysis has been producing the hadronic $dw_{23}$ distribution in the signal region (high Wness). In our analysis chain this hadronic distribution was produced by extrapolating low $Wness$ $dw_{23}$ distribution to the signal region and finally we did the fitting to get the signal to background ratio. In the PEPSI challenge we have the freedom to apply two methods to produce hadronic $dw_{23}$ distribution to do the fitting:

- Method 1: True $dw_{23}$ distribution of Monte Carlo signal, muonic background and hadronic backgrounds in signal region are used.

- Method 2: Same as above, but the hadronic background $dw_{23}$ distribution in signal region is produced by extrapolating low $Wness$ $dw_{23}$ to high $Wness$ region. This is similar procedure to what we followed in our analysis chain.

Note that the hadronic $\eta$ distribution in the second method is produced in a similar method to our analysis chain. i.e. hadronic $\eta$ produced from $\eta$ of hadrons with $Wness < 0.9$.

Comparing these two methods, the resulted fitting is shown in Figure 5.20. In these plots, the true PEPSI distributions (method 1) are displayed by filled histograms and the extrapolating method distributions are displayed by solid lines. The overall extrapolation is reasonable and the fits generally converge well. But, the signal $dw_{23}$ distribution from method 2 seems to be over estimated.

In this analysis, this potential overestimation will be assigned as the lower

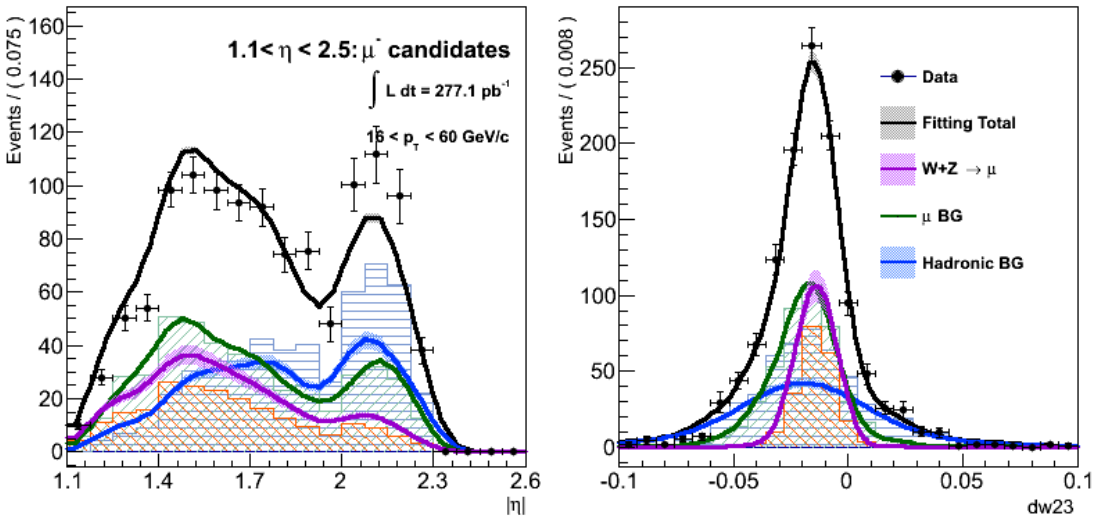



Figure 5.20: Fit results for the PEPSI challenge with a minimal $Wness$ selection of 0.85 for negative muons in south arm. The full lines are the results of the fit while the shaded, filled histograms display the contributions actually containted in this Monte Carlo set.

systematic error on the signal to background values by using the difference to the Monte Carlo signal based evaluation of signal to backgrounds. The upper systematic uncertainty of the signal to background ratio is taken directly taken from the upper uncertainty of the fit results[54].

## 5.6 Possible future improvements of the hadronic distribution in signal region

From the PEPSI challenge and other similar tests we made[54], the $dw_{23}$ of the data we used tends to narrow faster than linearly as a function of Wness, especially

at higher $Wness$ region. Currently this analysis is using linear dependence of the widths. The linear dependence is tested to be good in describing of the $Wness$ dependence within the fitting region of 0.1-0.9. Determining the expected nonlinear term, in the higher $Wness$ region will significantly improve the error. This may have little impact in improving the signal to background value.

Table 5.4: The fit results with $n_{sig}$, $n_{\mu}$, $n_{had}$, and the signal over background ratio in the three $\eta$ bins: $1.1-1.4$, $1.4-1.8, 1.8-2.6$.

| Species | $\eta$ range | $n_{sig}$ | $n_{had}$ | $n_{\mu}$ | Sig/BG |
|---|---|---|---|---|---|
| South $\mu^-$ | 1.10 - 1.40 | 30.90 | 26.30 | 44.10 | $0.44^{+0.06}_{-0.06}$ |
| | 1.40 - 1.80 | 74.70 | 106.00 | 121.50 | $0.33^{+0.06}_{-0.06}$ |
| | 1.80 - 2.60 | 36.70 | 81.80 | 90.30 | $0.21^{+0.06}_{-0.06}$ |
| South $\mu^+$ | 1.10 - 1.40 | 75.30 | 37.20 | 45.60 | $0.91^{+0.07}_{-0.07}$ |
| | 1.40 - 1.80 | 131.30 | 122.40 | 117.90 | $0.55^{+0.07}_{-0.07}$ |
| | 1.80 - 2.60 | 29.40 | 86.20 | 64.80 | $0.19^{+0.07}_{-0.07}$ |
| North $\mu^-$ | 1.10 - 1.40 | 48.90 | 20.90 | 44.50 | $0.75^{+0.07}_{-0.06}$ |
| | 1.40 - 1.80 | 88.80 | 86.60 | 89.60 | $0.50^{+0.07}_{-0.06}$ |
| | 1.80 - 2.60 | 41.80 | 102.70 | 54.60 | $0.27^{+0.07}_{-0.06}$ |
| North $\mu^+$ | 1.10 - 1.40 | 90.00 | 34.00 | 42.30 | $1.18^{+0.06}_{-0.06}$ |
| | 1.40 - 1.80 | 115.40 | 126.40 | 88.00 | $0.54^{+0.06}_{-0.06}$ |
| | 1.80 - 2.60 | 28.90 | 139.20 | 40.90 | $0.16^{+0.06}_{-0.06}$ |

# 6 Measurement of Longitudinal Single Spin Asymmetry of $W^{\pm}/Z \to \mu^{\pm}$

As discussed in the analysis strategy in the previous chapter, the last step of the analysis is to calculate the longitudinal spin asymmetry, $A_L$ of signal events. This calculation is done using the reduced dataset with basic cuts and $Wness$ cuts applied in the following steps.

1. Crossing and spin information must be obtained for each event.

2. Yields are counted for each spin pattern and a so-called raw asymmetry is calculated for each arm, charge and beam (yellow and blue) combination.

3. These asymmetries must then be corrected for background dilution and polarization factors and can then be combined to obtain final asymmetries for each charge and rapidity direction.

In this chapter, this process and the current status of its results are presented.

## 6.1 Asymmetry calculation

According to PHENIX coordinate system conventions shown in Figure 3.4, The clockwise beam coming from $-z$ (South) to $+z$ (North) is called Blue beam and the counterclockwise beam from $+z$ (North) to $-z$ (South) is called Yellow beam. In single spin asymmetry measurement we call the beam which the spin asymmetry is measured as "probe", and the other side beam as "target". For longitudinally-

polarized proton-proton collisions. The single spin asymmetry is defined as

$$A_L(\eta_\mu) = \left. \frac{d\sigma^{\Rightarrow} - d\sigma^{\Leftarrow}}{d\sigma^{\Rightarrow} + d\sigma^{\Leftarrow}} \right|_{\eta_\mu} \tag{6.1}$$

where the arrow denotes the helicity of the polarized proton ("$\Rightarrow$" denotes positive helicity and "$\Leftarrow$" denotes negative helicity), and pseudorapidity of muon $\eta_\mu$ is defined with taking the $z$-axis to the direction of the momentum of the probe-side beam. While considering the polarization of the Blue beam $\eta_\mu$ is taken as the same as the PHENIX coordinate system, but in case of the Yellow beam the sign of $\eta_\mu$ is opposite. We attempt to combine the measurement of the two Arms with assuming the biasing of the measurement in two Arms to the $\eta$-distribution of the signal does not differ largely. Let us denote the spin asymmetry in forward ($\eta_\mu > 0$) and backward ($\eta_\mu < 0$) pseudorapidity as $A_L^{\eta_\mu > 0}$, $A_L^{\eta_\mu < 0}$, respectively. We also define longitudinal double spin asymmetry $A_{LL}$ as

$$A_{LL}(\eta_\mu) = \left. \frac{d\sigma^{\Rightarrow\Rightarrow} - d\sigma^{\Leftarrow\Rightarrow}}{d\sigma^{\Rightarrow\Rightarrow} + d\sigma^{\Leftarrow\Rightarrow}} \right|_{\eta_\mu} \tag{6.2}$$

where the first arrow denotes the polarization of the probe-side beam and the second denotes that of the target-side beam. Again the rapidity $\eta_\mu$ is defined with respect to the probe-side beam, however due to the symmetry we have $A_{LL}(\eta_\mu) = A_{LL}(-\eta_\mu)$ and the sign of $\eta_\mu$ does not matter. Hereafter we alternatively use "+" as positive helicity state and "$-$" for negative.

## 6.2 Crossing information and spin patterns

For each crossing or possible collision the blue and the yellow beams could always have one of the are 4 possible pairs of helicity combinations. These pairs are

$$(s_B, s_Y) = \text{“}++\text{”}, \text{“}+-\text{”}, \text{“}-+\text{”}, \text{“}--\text{”}$$

where the first sign denotes the helicity of the Blue beam and the second denotes that of the Yellow beam. We denote the number of signal candidates after signal selection for each spin combination for each arm as

$$\left\{n^S_{(++)}, n^S_{(+-)}, n^S_{(-+)}, n^S_{(--)}\right\}, \quad \left\{n^N_{(++)}, n^N_{(+-)}, n^N_{(-+)}, n^N_{(--)}\right\}$$

where the index $S, N$ denotes the South and North Arm, respectively.

The crossing ID and helicity patterns of Run 2013 proton-proton (blue-yellow) beams are stored in the PHENIX official spin database for asymmetry evaluation. For the asymmetry calculation the yields for each pattern were summed up over all runs. The yields for each spin pattern are shown in Figure 6.1 and Figure 6.2 for the background dominated events and for the signal dominated events respectively. The background dominated events all give raw asymmetries consistent with zero as compared to the signal enhanced sample. This is consistent with the expectation of no parity violating asymmetries and therefore the signal asymmetries needs to be corrected only for dilution, but no additional asymmetry. The corresponding yields and raw asymmetries for the signal region shows that the

yields are not as evenly distributed between the different spin states indicating nonzero asymmetries.

We denote $L_{(\pm\pm)}$ as the integrated luminosity of the corresponding $\pm\pm$ pairs of spin combination and $L_0$ as the total integrated luminosity. Using these quantities, we define the ratio $r_{(\pm\pm)} \equiv L_{(\pm\pm)}/L_0$ as the *relative luminosity* which satisfies the condition:

$$\sum_{s_B=\pm}\sum_{s_Y=\pm} r_{(s_B s_Y)} = 1. \tag{6.3}$$

The observed or raw asymmetry ($\epsilon$) in terms of the luminosity corrected yield $\tilde{n}^{S,N}_{(\pm\pm)} \equiv n^{S,N}_{(\pm\pm)}/r_{(\pm\pm)}$ is calculated as follows. Note that, we measure Yellow beam's forward asymmetry (Yellow FW) and Blue beam's backward asymmetry (Blue BW) in the South arm. Similarly, we measure Blue beam's forward asymmetry (Blue FW) and Yellow beam's backward (Yellow BW) asymmetry in the North arm.

$$Yellow\ FW \qquad \epsilon^{\eta>0}_{L,S} \equiv \left[\frac{\tilde{n}^S_{(++)} - \tilde{n}^S_{(+-)} + \tilde{n}^S_{(-+)} - \tilde{n}^S_{(--)}}{\tilde{n}^S_{(++)} + \tilde{n}^S_{(+-)} + \tilde{n}^S_{(-+)} + \tilde{n}^S_{(--)}}\right] \tag{6.4}$$

$$Blue\ BW \qquad \epsilon^{\eta<0}_{L,S} \equiv \left[\frac{\tilde{n}^S_{(++)} + \tilde{n}^S_{(+-)} - \tilde{n}^S_{(-+)} - \tilde{n}^S_{(--)}}{\tilde{n}^S_{(++)} + \tilde{n}^S_{(+-)} + \tilde{n}^S_{(-+)} + \tilde{n}^S_{(--)}}\right] \tag{6.5}$$

$$\epsilon_{LL,S} \equiv \left[\frac{\tilde{n}^S_{(++)} - \tilde{n}^S_{(+-)} - \tilde{n}^S_{(-+)} + \tilde{n}^S_{(--)}}{\tilde{n}^S_{(++)} + \tilde{n}^S_{(+-)} + \tilde{n}^S_{(-+)} + \tilde{n}^S_{(--)}}\right] \tag{6.6}$$

$$Blue\ FW \qquad \epsilon_{L,N}^{\eta>0} \equiv \left[\frac{\tilde{n}_{(++)}^{N} + \tilde{n}_{(+-)}^{N} - \tilde{n}_{(-+)}^{N} - \tilde{n}_{(--)}^{N}}{\tilde{n}_{(++)}^{N} + \tilde{n}_{(+-)}^{N} + \tilde{n}_{(-+)}^{N} + \tilde{n}_{(--)}^{N}}\right] \tag{6.7}$$

$$Yellow\ BW \qquad \epsilon_{L,N}^{\eta<0} \equiv \left[\frac{\tilde{n}_{(++)}^{N} - \tilde{n}_{(+-)}^{N} + \tilde{n}_{(-+)}^{N} - \tilde{n}_{(--)}^{N}}{\tilde{n}_{(++)}^{N} + \tilde{n}_{(+-)}^{N} + \tilde{n}_{(-+)}^{N} + \tilde{n}_{(--)}^{N}}\right] \tag{6.8}$$

$$\epsilon_{LL,N} \equiv \left[\frac{\tilde{n}_{(++)}^{N} - \tilde{n}_{(+-)}^{N} - \tilde{n}_{(-+)}^{N} + \tilde{n}_{(--)}^{N}}{\tilde{n}_{(++)}^{N} + \tilde{n}_{(+-)}^{N} + \tilde{n}_{(-+)}^{N} + \tilde{n}_{(--)}^{N}}\right] \tag{6.9}$$

These raw spin asymmetries are related to the final single spin asymmetry ($A_L$) and double spin asymmetry ($A_{LL}$) as

$$FW Asymmetry \qquad A_L^{\eta>0} = \frac{D^N}{P_B}\epsilon_{L,N}^{\eta>0} = \frac{D^S}{P_Y}\epsilon_{L,S}^{\eta>0} \tag{6.10}$$

$$BW Asymmetry \qquad A_L^{\eta<0} = \frac{D^N}{P_B}\epsilon_{L,N}^{\eta<0} = \frac{D^S}{P_Y}\epsilon_{L,S}^{\eta<0} \tag{6.11}$$

$$A_{LL} = \frac{D^N}{P_B P_Y}\epsilon_{LL,N} = \frac{D^S}{P_B P_Y}\epsilon_{LL,S} \tag{6.12}$$

where

$$D^{S,N} \equiv \frac{n_{\rm sig}^{S,N} + n_{\rm BG}^{S,N}}{n_{\rm sig}^{S,N}} \tag{6.13}$$

is called *dilution factor* by means of diluting the *observed* or *raw* spin asymmetries.

## 6.3 Results and discussions

### 6.3.1 Signal to Background ratio results with uncertainity

The various contributions from the fit uncertainties, the smearing variation and the muon background variation have been added in quadrature. These systematic uncertainties are summarized in Table 6.1 for 3 diffrent $\eta$ bins and for the whole $\eta$ range:

- $\eta$ bin 0 represents $(1.1 < \eta < 1.4)$,
- $\eta$ bin 1 represents $(1.4 < \eta < 1.8)$,
- $\eta$ bin 2 represents $(1.8 < \eta < 2.6)$,
- $\eta$ bin 3 represents $(1.1 < \eta < 2.6)$, which is the whole $\eta$ range in an arm.

Since the $W$ signal simulation based signal to background evaluation gives values which are within these uncertainties, no further uncertainties are added for the PEPSI challenge discussed in Chapter 5. Comparing the uncertainties shown in Table 6.1, usually neither smearing nor the fitting uncertainties are the dominating numbers. Major contribution to the uncertainties are from muon background evaluation which originate from the uncertainties in the relative scaling factors of various real muon background processes for the dimuons. Also the uncertainties in the trigger efficiencies do account for some variation as they also affect the amount of muon background introduced.

### 6.3.2 Final longitudinal single spin asymmetry results

The final longitudinal single spin asymmetry of $\mu^{\pm}$ in $16 < p_T^{\rm reco} < 60$ GeV/$c$ from $W^{\pm}/Z$ bosons $A_L^{\mu^{\pm}}$ at forward and backward rapidity regions are summarized in Table 6.2. Both statistical and systematic uncertainties are taken into account.

The forward and backward asymmetries are determined by averaging over the asymmetries from each beam as follows:

Table 6.1: Signal to Background results including uncertainties from various contributions which will enter the final asymmetries based on a wness cut of 0.99.

| | $\eta$ bin | stat | smear | $\mu$BG | Trigeffi | SBG combined |
|---|---|---|---|---|---|---|
| $N^+$ | 1.1-1.4 | $1.18^{0.20}_{0.18}$ | $^{0.04}_{0.00}$ | $^{0.17}_{0.16}$ | $^{0.00}_{0.37}$ | $1.18^{0.26}_{0.44}$ |
| $N^-$ | 1.1-1.4 | $0.75^{0.15}_{0.14}$ | $^{0.19}_{0.00}$ | $^{0.17}_{0.16}$ | $^{0.00}_{0.33}$ | $0.75^{0.30}_{0.39}$ |
| $S^+$ | 1.1-1.4 | $0.91^{0.16}_{0.15}$ | $^{0.05}_{0.00}$ | $^{0.17}_{0.15}$ | $^{0.04}_{0.09}$ | $0.91^{0.24}_{0.23}$ |
| $S^-$ | 1.1-1.4 | $0.44^{0.11}_{0.10}$ | $^{0.04}_{0.00}$ | $^{0.14}_{0.12}$ | $^{0.01}_{0.28}$ | $0.44^{0.18}_{0.32}$ |
| $N^+$ | 1.4-1.8 | $0.54^{0.09}_{0.08}$ | $^{0.02}_{0.00}$ | $^{0.08}_{0.07}$ | $^{0.00}_{0.14}$ | $0.54^{0.12}_{0.18}$ |
| $N^-$ | 1.4-1.8 | $0.50^{0.10}_{0.09}$ | $^{0.12}_{0.00}$ | $^{0.12}_{0.10}$ | $^{0.00}_{0.19}$ | $0.50^{0.20}_{0.23}$ |
| $S^+$ | 1.4-1.8 | $0.55^{0.10}_{0.09}$ | $^{0.03}_{0.00}$ | $^{0.10}_{0.09}$ | $^{0.08}_{0.06}$ | $0.55^{0.16}_{0.14}$ |
| $S^-$ | 1.4-1.8 | $0.33^{0.08}_{0.07}$ | $^{0.03}_{0.00}$ | $^{0.10}_{0.09}$ | $^{0.01}_{0.20}$ | $0.33^{0.14}_{0.23}$ |
| $N^+$ | 1.8-2.6 | $0.16^{0.03}_{0.02}$ | $^{0.01}_{0.00}$ | $^{0.02}_{0.02}$ | $^{0.04}_{0.00}$ | $0.16^{0.05}_{0.03}$ |
| $N^-$ | 1.8-2.6 | $0.27^{0.05}_{0.05}$ | $^{0.07}_{0.00}$ | $^{0.06}_{0.06}$ | $^{0.03}_{0.05}$ | $0.27^{0.11}_{0.09}$ |
| $S^+$ | 1.8-2.6 | $0.19^{0.03}_{0.03}$ | $^{0.01}_{0.00}$ | $^{0.03}_{0.03}$ | $^{0.08}_{0.00}$ | $0.19^{0.09}_{0.04}$ |
| $S^-$ | 1.8-2.6 | $0.21^{0.05}_{0.05}$ | $^{0.02}_{0.00}$ | $^{0.07}_{0.06}$ | $^{0.05}_{0.11}$ | $0.21^{0.10}_{0.13}$ |
| $N^+$ | 1.1-2.6 | $0.50^{0.08}_{0.08}$ | $^{0.02}_{0.00}$ | $^{0.07}_{0.07}$ | $^{0.00}_{0.12}$ | $0.50^{0.11}_{0.16}$ |
| $N^-$ | 1.1-2.6 | $0.45^{0.09}_{0.08}$ | $^{0.11}_{0.00}$ | $^{0.10}_{0.09}$ | $^{0.00}_{0.16}$ | $0.45^{0.18}_{0.20}$ |
| $S^+$ | 1.1-2.6 | $0.50^{0.09}_{0.08}$ | $^{0.03}_{0.00}$ | $^{0.09}_{0.08}$ | $^{0.03}_{0.08}$ | $0.50^{0.13}_{0.14}$ |
| $S^-$ | 1.1-2.6 | $0.30^{0.07}_{0.07}$ | $^{0.03}_{0.00}$ | $^{0.09}_{0.08}$ | $^{0.02}_{0.18}$ | $0.30^{0.12}_{0.21}$ |

- The Blue beam asymmetry measured in the north arm and the Yellow beam asymmetry measured in the south arm are combined as Forward (FW) asymmetry.

- The Blue beam asymmetry measured in the south arm and the Yellow beam asymmetry measured in the north arm are combined as Backward (BW) asymmetry.

The final single spin asymmetry ($A_L$) for each of the 3 $\eta$ bins in each arm from both Blue and Yellow beams are summarized in Table 6.3, Table 6.4 and Table 6.5. The signal to background values were extracted from the MC based signal and data, the uncertainty on the S/BG value from the fit is given as a systematic uncertainty

Table 6.2: The final longitudinal single spin asymmetries $A_L$ for the whole $\eta$ range as a function of rapidity with minimum transverse momentum of $16\,\mathrm{GeV}/c$ with and without combining the two beams and using a minimum $W$ likelihood cut level of $f_{cut} > 0.99$. The signal to background values were extracted from the MC based signal and data, the uncertainty on the S/BG value from the fit is given as a systematic uncertainty.

| | beam | $\eta$ bin | S/BG | raw $A_L$ | corrected $A_L$ |
|---|---|---|---|---|---|
| $N^+$ | B | 1.10-2.60 | $0.50^{0.11}_{0.16}$ | $-0.057 \pm 0.037$ | $-0.327 \pm 0.21^{0.08}_{0.08}$ |
| $S^+$ | Y | 1.10-2.60 | $0.50^{0.13}_{0.14}$ | $-0.063 \pm 0.037$ | $-0.346 \pm 0.20^{0.20}_{0.20}$ |
| $FW^+$ | comb | 1.10-2.60 | | | $-0.337 \pm 0.15^{0.22}_{-0.22}$ |
| $S^+$ | B | 1.10-2.60 | $0.50^{0.13}_{0.14}$ | $0.015 \pm 0.037$ | $0.087 \pm 0.21^{0.08}_{0.08}$ |
| $N^+$ | Y | 1.10-2.60 | $0.50^{0.11}_{0.16}$ | $0.035 \pm 0.037$ | $0.194 \pm 0.20^{0.14}_{0.14}$ |
| $BW^+$ | comb | 1.10-2.60 | | | $0.141 \pm 0.15^{0.16}_{-0.16}$ |
| $N^-$ | B | 1.10-2.60 | $0.45^{0.18}_{0.20}$ | $0.039 \pm 0.041$ | $0.247 \pm 0.25^{0.16}_{0.16}$ |
| $S^-$ | Y | 1.10-2.60 | $0.30^{0.12}_{0.21}$ | $0.026 \pm 0.041$ | $0.214 \pm 0.32^{0.50}_{0.50}$ |
| $FW^-$ | comb | 1.10-2.60 | | | $0.233 \pm 0.20^{0.52}_{-0.52}$ |
| $S^-$ | B | 1.10-2.60 | $0.30^{0.12}_{0.21}$ | $-0.016 \pm 0.041$ | $-0.134 \pm 0.33^{0.30}_{0.30}$ |
| $N^-$ | Y | 1.10-2.60 | $0.45^{0.18}_{0.20}$ | $-0.012 \pm 0.041$ | $-0.076 \pm 0.24^{0.24}_{0.24}$ |
| $BW^-$ | comb | 1.10-2.60 | | | $-0.101 \pm 0.19^{0.38}_{-0.38}$ |

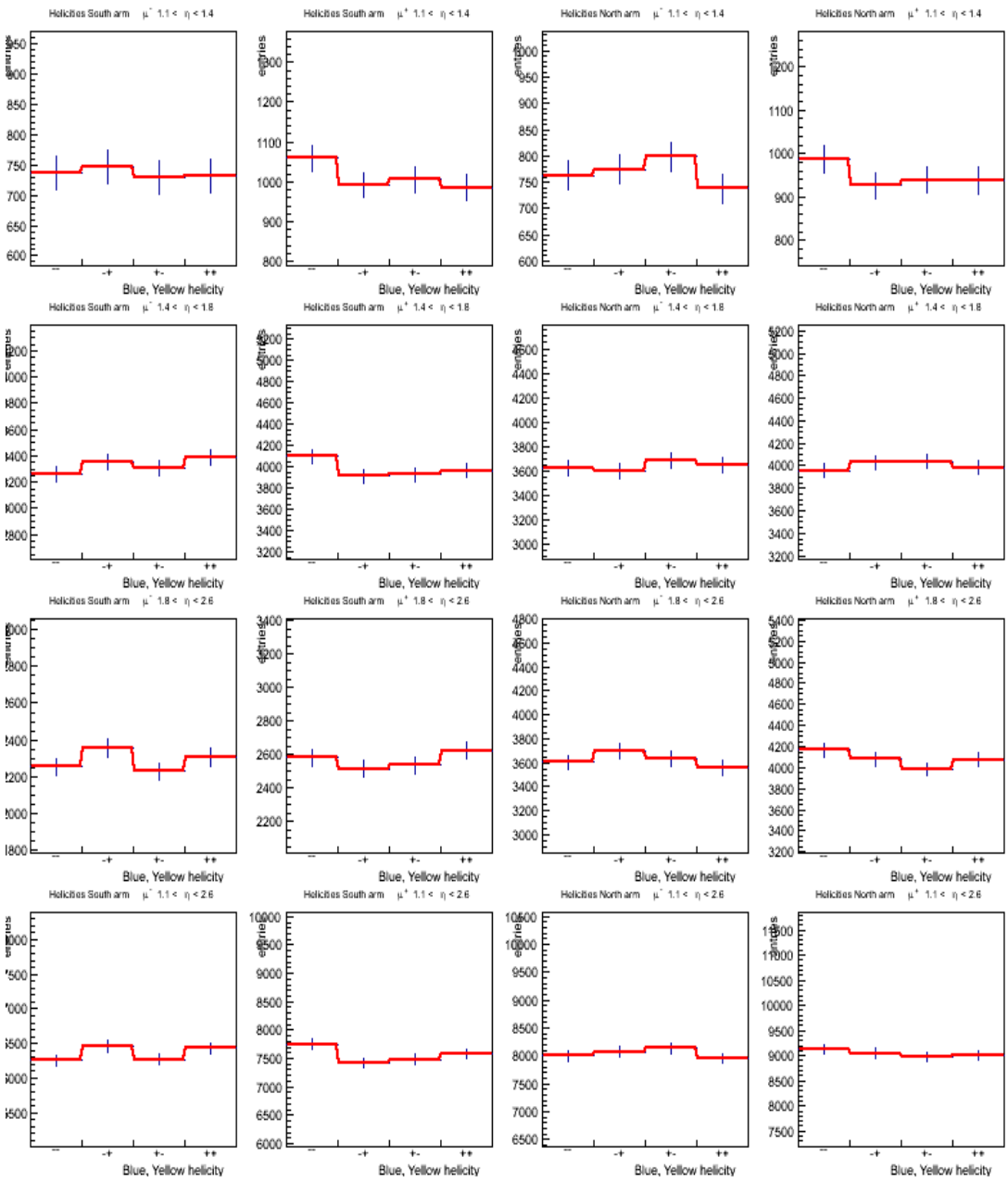



Figure 6.1: Yields for the four possible spin patterns shown in the horizontal axis: "++", "+−", "−+", "−−" respectively for the lowest (background-dominated) likelihood ratios $Wness > 0.0$ selection criterion.

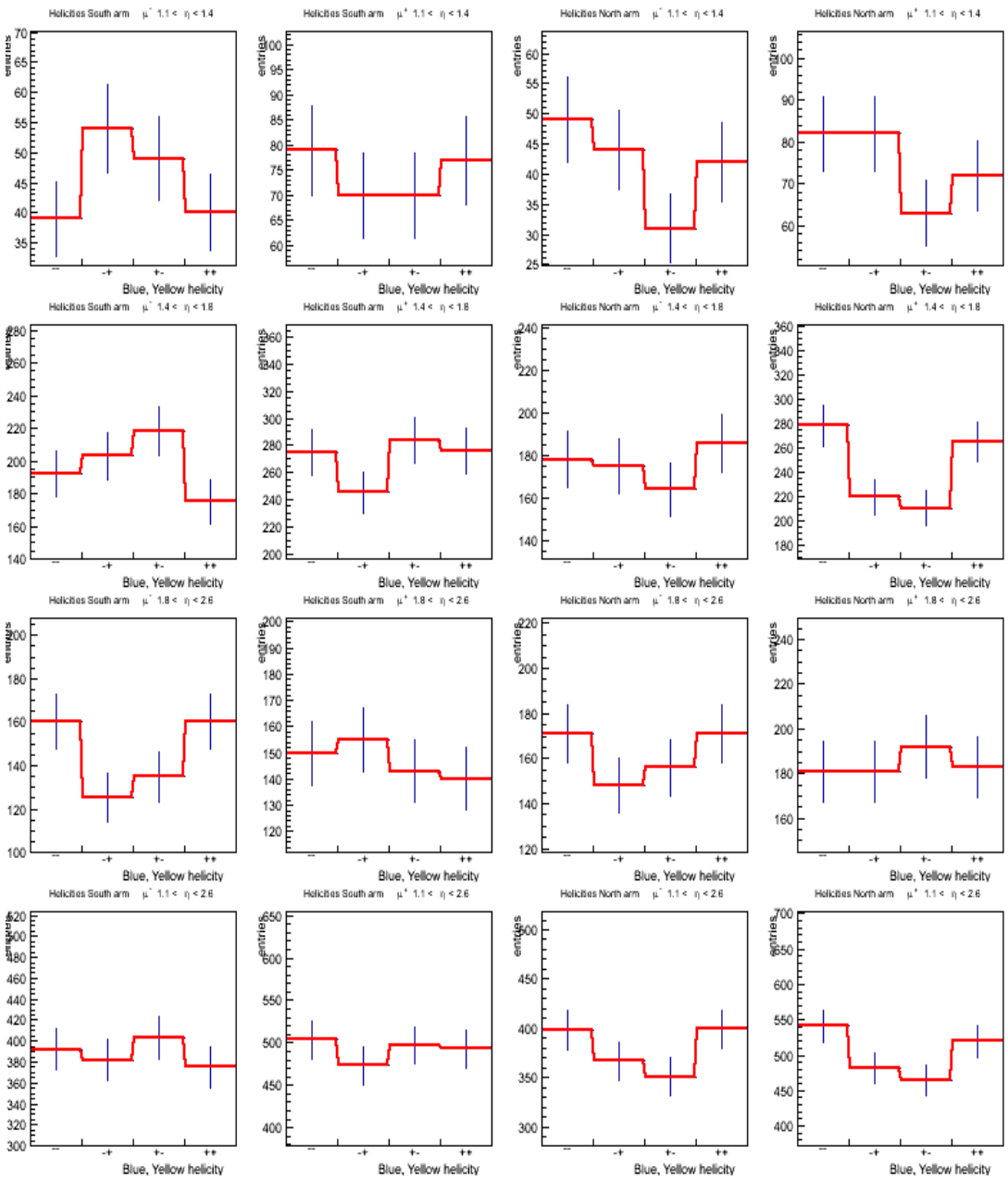



Figure 6.2: Yields for the four possible spin patterns shown in the horizontal axis: "++", "+−", "−+", "−−" respectively for signal-enhanced selection criterion $Wness > 0.92$.

Table 6.3: The final longitudinal single spin asymmetries $A_L$ in the $1.1 < \eta < 1.4$ range as a function of rapidity with minimum transverse momentum of $16\,\mathrm{GeV}/c$ with and without combining the two beams and using a minimum $W$ likelihood cut level of $f_{cut} > 0.99$.

| Arm/charge | beam | $\eta$ bin | $<\eta>$ | S/BG | corrected $A_L$ |
|---|---|---|---|---|---|
| $N^+$ | B | 1.10-1.40 | 1.31 | $1.18^{0.26}_{0.44}$ | $-0.366 \pm 0.32^{0.09}_{0.09}$ |
| $S^+$ | Y | 1.10-1.40 | 1.31 | $0.91^{0.24}_{0.23}$ | $0.227 \pm 0.38^{0.20}_{0.20}$ |
| $FW^+$ | comb | 1.10-1.40 | 1.31 | | $-0.094 \pm 0.24^{0.22}_{-0.22}$ |
| $S^+$ | B | 1.10-1.40 | -1.31 | $0.91^{0.24}_{0.23}$ | $-0.075 \pm 0.38^{0.13}_{0.13}$ |
| $N^+$ | Y | 1.10-1.40 | -1.31 | $1.18^{0.26}_{0.44}$ | $-0.181 \pm 0.31^{0.12}_{0.12}$ |
| $BW^+$ | comb | 1.10-1.40 | -1.31 | | $-0.133 \pm 0.24^{0.18}_{-0.18}$ |
| $N^-$ | B | 1.10-1.40 | 1.31 | $0.75^{0.30}_{0.39}$ | $-0.058 \pm 0.54^{0.37}_{0.37}$ |
| $S^-$ | Y | 1.10-1.40 | 1.31 | $0.44^{0.18}_{0.32}$ | $-0.003 \pm 0.72^{0.69}_{0.69}$ |
| $FW^-$ | comb | 1.10-1.40 | 1.31 | | $-0.035 \pm 0.43^{0.78}_{-0.78}$ |
| $S^-$ | B | 1.10-1.40 | -1.31 | $0.44^{0.18}_{0.32}$ | $-0.370 \pm 0.74^{0.70}_{0.70}$ |
| $N^-$ | Y | 1.10-1.40 | -1.31 | $0.75^{0.30}_{0.39}$ | $0.071 \pm 0.53^{0.45}_{0.45}$ |
| $BW^-$ | comb | 1.10-1.40 | -1.31 | | $-0.111 \pm 0.43^{0.83}_{-0.83}$ |

Table 6.4: The final longitudinal single spin asymmetries $A_L$ in the $1.4 < \eta < 1.8$ range as a function of rapidity with minimum transverse momentum of $16\,\mathrm{GeV}/c$ with and without combining the two beams and using a minimum $W$ likelihood cut level of $f_{cut} > 0.99$.

| Arm/charge | beam | $\eta$ bin | $< \eta >$ | S/BG | corrected $A_L$ |
|---|---|---|---|---|---|
| $N^+$ | B | 1.40-1.80 | 1.58 | $0.54^{0.12}_{0.18}$ | $-0.502 \pm 0.28^{0.12}_{0.12}$ |
| $S^+$ | Y | 1.40-1.80 | 1.58 | $0.55^{0.16}_{0.14}$ | $-0.366 \pm 0.25^{0.28}_{0.28}$ |
| $FW^+$ | comb | 1.40-1.80 | 1.58 | | $-0.431 \pm 0.19^{0.30}_{-0.30}$ |
| $S^+$ | B | 1.40-1.80 | -1.58 | $0.55^{0.16}_{0.14}$ | $0.297 \pm 0.26^{0.11}_{0.11}$ |
| $N^+$ | Y | 1.40-1.80 | -1.58 | $0.54^{0.12}_{0.18}$ | $0.394 \pm 0.27^{0.20}_{0.20}$ |
| $BW^+$ | comb | 1.40-1.80 | -1.58 | | $0.344 \pm 0.19^{0.22}_{-0.22}$ |
| $N^-$ | B | 1.40-1.80 | 1.59 | $0.50^{0.20}_{0.23}$ | $0.497 \pm 0.33^{0.22}_{0.22}$ |
| $S^-$ | Y | 1.40-1.80 | 1.61 | $0.33^{0.14}_{0.23}$ | $0.454 \pm 0.41^{0.71}_{0.71}$ |
| $FW^-$ | comb | 1.40-1.80 | 1.60 | | $0.478 \pm 0.26^{0.75}_{-0.75}$ |
| $S^-$ | B | 1.40-1.80 | -1.61 | $0.33^{0.14}_{0.23}$ | $-0.510 \pm 0.42^{0.43}_{0.43}$ |
| $N^-$ | Y | 1.40-1.80 | -1.59 | $0.50^{0.20}_{0.23}$ | $0.071 \pm 0.33^{0.33}_{0.33}$ |
| $BW^-$ | comb | 1.40-1.80 | -1.60 | | $-0.182 \pm 0.26^{0.54}_{-0.54}$ |

Table 6.5: The final longitudinal single spin asymmetries $A_L$ in the $1.8 < \eta < 2.6$ range as a function of rapidity with minimum transverse momentum of $16\,\mathrm{GeV}/c$ with and without combining the two beams and using a minimum $W$ likelihood cut level of $f_{cut} > 0.99$.

| Arm/charge | beam | $\eta$ bin | $< \eta >$ | S/BG | corrected $A_L$ |
|---|---|---|---|---|---|
| $N^+$ | B | 1.80-2.60 | 2.01 | $0.16^{0.05}_{0.03}$ | $0.223 \pm 0.86^{0.59}_{0.59}$ |
| $S^+$ | Y | 1.80-2.60 | 1.99 | $0.19^{0.09}_{0.04}$ | $-1.239 \pm 0.80^{1.11}_{1.11}$ |
| $FW^+$ | comb | 1.80-2.60 | 2.00 | | $-0.534 \pm 0.58^{1.25}_{-1.25}$ |
| $S^+$ | B | 1.80-2.60 | -1.99 | $0.19^{0.09}_{0.04}$ | $-0.581 \pm 0.81^{0.94}_{0.94}$ |
| $N^+$ | Y | 1.80-2.60 | -2.01 | $0.16^{0.05}_{0.03}$ | $0.232 \pm 0.84^{0.82}_{0.82}$ |
| $BW^+$ | comb | 1.80-2.60 | -2.00 | | $-0.182 \pm 0.58^{1.24}_{-1.24}$ |
| $N^-$ | B | 1.80-2.60 | 2.04 | $0.27^{0.11}_{0.09}$ | $-0.003 \pm 0.56^{0.50}_{0.50}$ |
| $S^-$ | Y | 1.80-2.60 | 1.99 | $0.21^{0.10}_{0.13}$ | $-0.128 \pm 0.69^{0.92}_{0.92}$ |
| $FW^-$ | comb | 1.80-2.60 | 2.02 | | $-0.059 \pm 0.44^{1.04}_{-1.04}$ |
| $S^-$ | B | 1.80-2.60 | -1.99 | $0.21^{0.10}_{0.13}$ | $0.711 \pm 0.70^{0.66}_{0.66}$ |
| $N^-$ | Y | 1.80-2.60 | -2.04 | $0.27^{0.11}_{0.09}$ | $-0.440 \pm 0.55^{0.57}_{0.57}$ |
| $BW^-$ | comb | 1.80-2.60 | -2.02 | | $0.065 \pm 0.43^{0.87}_{-0.87}$ |

The preliminary results of the $\eta$ combined asymmetry $A_L^{\mu\pm}$ are shown in Figure 6.3 together with predictions of $A_L^{\mu\pm}$ as a function of $\eta$ of various global analyses. The plots also show the preliminary results form previous years' forward and central W analysis results as well as the final STAR run 2012 results for reference. From the plots, one can see the asymmetries appear to be consistent with theoretical predictions in the forward arm. In the backward rapidities the asymmetries are positive or consistent with zero which is also in agreement with the asymmetry observed by an independent experiment at STAR in RHIC[94]. The important results of this study are the signal to background ratios and the the asymmetries at the forward and backward rapidities. The results are based on the largest data set ever collected for $W$ measurement and will give more information and reduce uncertainity in polarized parton distribution functions for anti-up and anti-down quarks.

The preliminary results for the 3 $\eta$ separated asymmetries $A_L^{\mu\pm}$ are shown in Figure 6.4.

## 6.4 Future prospects

This analysis used simulation based signal and muonic background events to model the $W^{\pm} \rightarrow \mu^{\pm}$ events and other muon producing events. However producing the required amount of simulation data that is enough to represent the actual huge amount of hadronic background is still in progress. Instead, the hadronic

background PDFs in this analysis are sampled from real data as it is largely dominated by hadronic background. And a chain of complex statistical tools are used to mimic the hadronc events. As dicussed in Section 5.6 the PEPSI challenge shows the $dw_{23}$ of the data we used tends to narrow faster than linearly as a function of Wness, especially at higher $Wness$ region. Determining the expected nonlinear term and its impact on the error is being studied[54]. Completing the ongoing hadronic simulations will provide confidence on the results. Even though, FVTX valid events are only 23% of entire data, reducing the correlation between FVTX matching variables and MuTr variables will have some positive impact on background reduction.

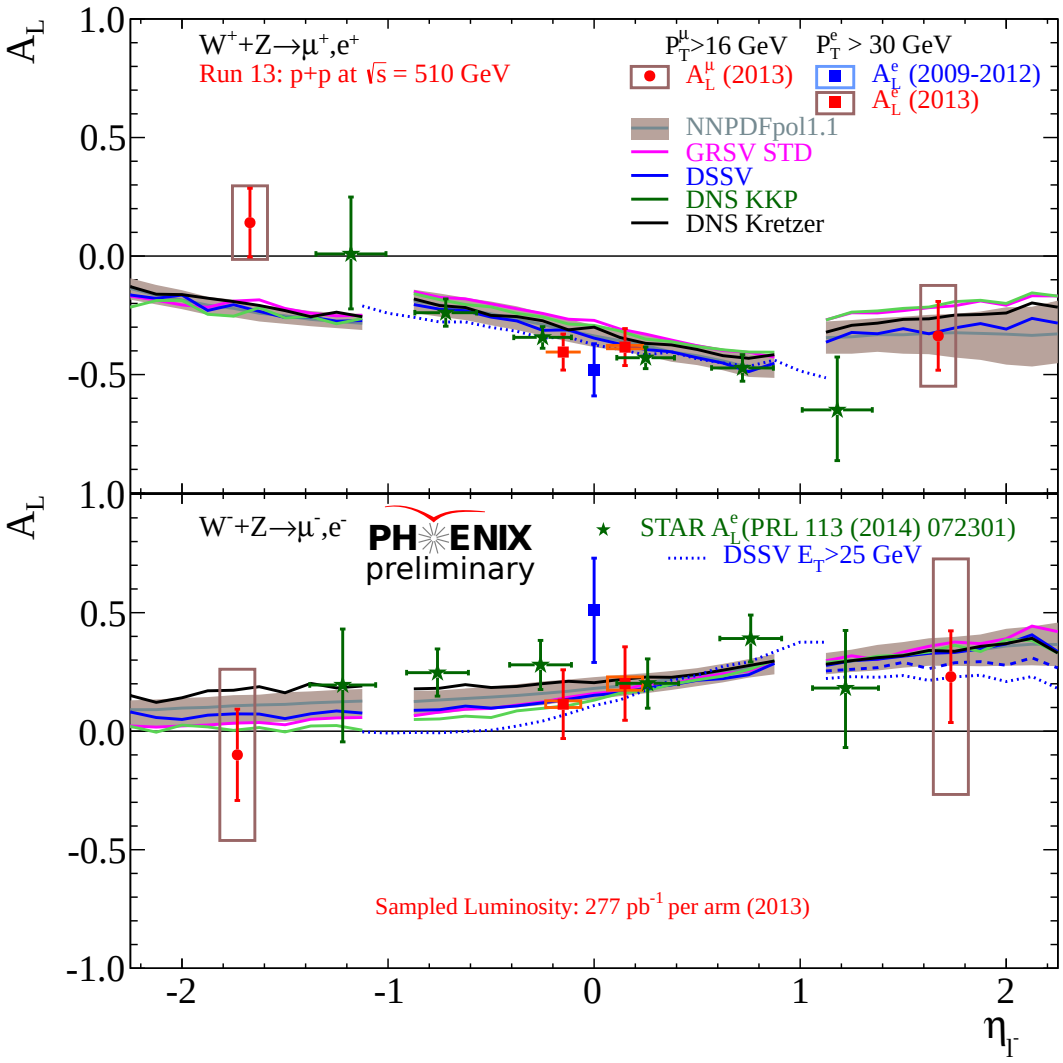



Figure 6.3: Preliminary single spin asymmetries for Run 2013 (red markers) using a $Wness > 0.99$ selection, and the published run 2012 STAR results (green). The top plot displays the $W^+/Z \to \mu^+$ asymmetries, the bottom plot displays the $W^-/Z \to \mu^-$ asymmetries.

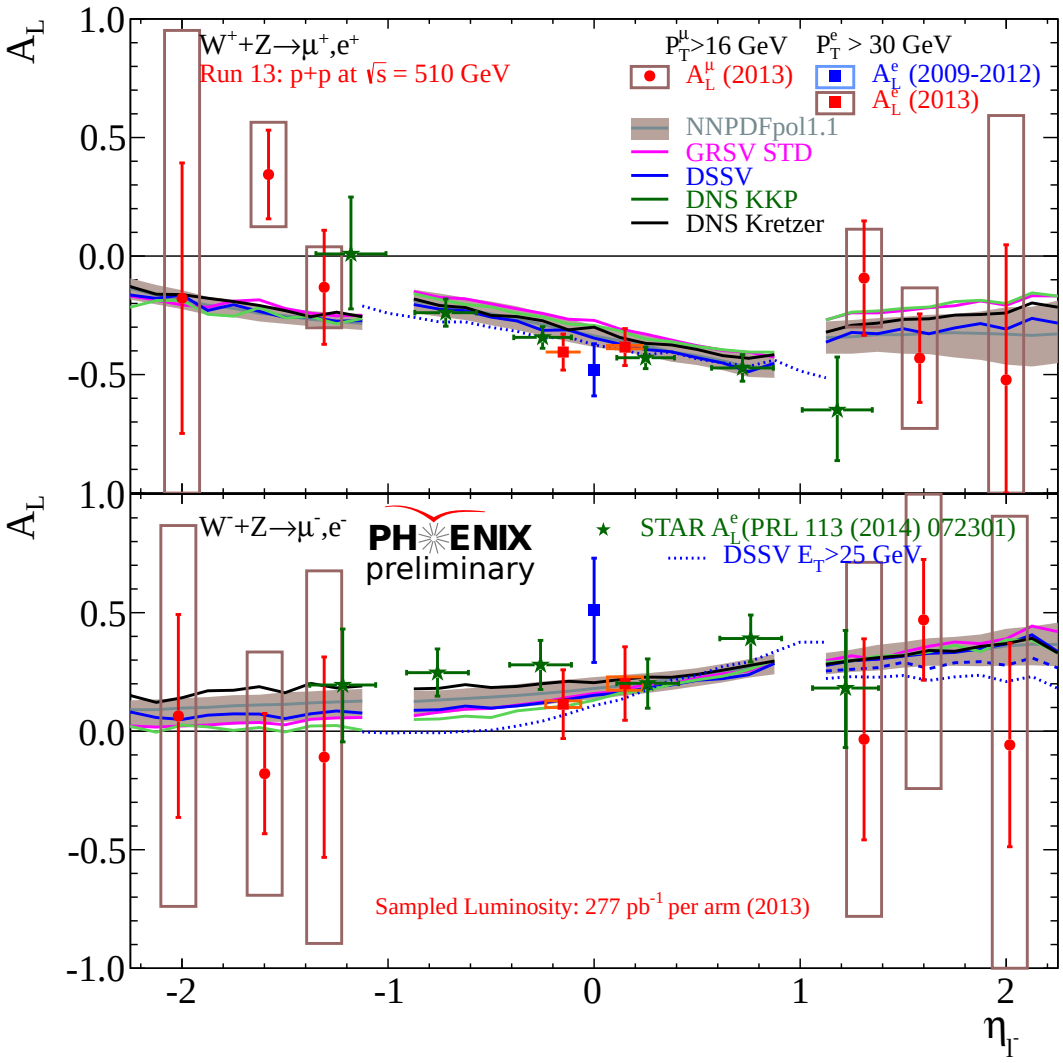



Figure 6.4: Preliminary single spin asymmetries for Run 2013 (red markers) using a $Wness > 0.99$ selection, and the published run 2012 STAR (green)results. The top plot displays the $W^+/Z \rightarrow \mu^+$ asymmetries, the bottom plot displays the $W^-/Z \rightarrow \mu^-$ asymmetries.

## REFERENCES


[1] X. Ji, A Modern Indroduction to Nuclear Physics, WWW Lecture Document, (http://www.physics.umd.edu/courses/Phys741/xji/chapter1.pdf).

[2] L.W. Alvarez, F.Bloch, Phys. Rev. 57, 111 ((1940))

[3] M. Gell-Mann, Phys. Lett. 8, 214 (1964)

[4] K. Nishijima, Prog. Theor. Phys. Vol. 13 No. 3 (1955) pp. 285-304

[5] J.D. Bjorken, Phys. Rev. 148, 1467 (1966)

[6] E155 Collaboration, Phys. Lett. B493, 19 (2000).

[7] HERMES Collaboration, Phys. Rev. D75, 012007 (2007).

[8] **(MRST02)** A.D. Martin, et al. (MRST02), Eur. Phys. J. C28:455-473,2003

[9] **(DSSV)** D. de Florian, et al. (DSSV), Phys.Rev.D80:034030,2009

[10] **(PDG2012)** J. Beringer et al., Phys. Rev. D86, 010001 (2012)

[11] **(DSSV)** D. de Florian and W. Vogelsang, Phys. Rev. D81, 094020 (2010), hep-ph/1003.4533

[12] M. J. Alguard et al., Phys. Rev. Lett. 37, 1261 (1976)

[13] M. J. Alguard et al., Phys. Rev. Lett. 41, 70 (1978)

[14] G. Baum et al., Phys. Rev. Lett. 45, 2000 (1980)

[15] G. Baum et al., Phys. Rev. Lett. 51, 1135 (1983).

[16] **(EMC)** J. Ashman et al., Phys. Lett. B 206 (2) 364 (1988)

[17] **(EMC)** J. Ashman et al., Nucl. Phy. B 328 (1989) 1-35

[18] **(E142)** P.L. Anthony et al., Phys. Rev. D54, 6620 (1996)

[19] **(E143)** K. Abe et al., Phys. Rev. D58, 112003 (1998)

[20] **(SMC)** B. Adeva et al., Phys. Rev. D58, 112001 (1998)

[21] **(SMC)** B. Adeva et al., Phys. Rev. D60, 072004 (1999) and Erratum-Phys. Rev. D62, 079902 (2000)

[22] **(HERMES)** A. Airapetian et al., Phys. Rev. D75, 012007 (2007)

[23] **(HERMES)** K. Ackerstaff et al., Phys. Lett. B404, 383 (1997)

[24] **(E154)** K. Abe et al., Phys. Rev. Lett. 79, 26 (1997)

[25] **(E154)** P.L. Anthony et al., Phys. Lett. B493, 19 (2000)

[26] **(E155)** P.L. Anthony et al., Phys. Lett. B463, 339 (1999)

[27] **(Jlab-E99-117)** X. Zheng et al., Phys. Rev. C70, 065207 (2004)

[28] **(COMPASS)** V.Yu. Alexakhin et al., Phys. Lett. B647, 8 (2007)

[29] **(COMPASS)** E.S. Ageev et al., Phys. Lett. B647, 330 (2007)

[30] **(COMPASS)** M.G. Alekseev et al., Phys. Lett. B690, 466 (2010)

[31] **(CLAS)** K.V. Dharmawardane et al., Phys. Lett. B641, 11 (2006)

[32] L. Wolfenstein, Phys. Rev. Lett. 51 1945 (1983)

[33] **(STAR)** G. Agakishiev et al., Phys. Rev. D 85 (2012) 92010, hep-ex/1112.2980v1

[34] **(UA1)** C. Albajar et al., Phys. Lett. B198, 271 (1987).

[35] **(UA1)** C. Albajar et al., Z. Phys. C44, 15 (1989).

[36] **(UA1)** J. Alitti et al., Z. Phys. C47, 11 (1990).

[37] **(UA1)** J. Alitti et al., Phys. Lett. B276, 365 (1992).

[38] **(CDF)** F. Abe et al., Phys. Rev. Lett. 76, 3070 arXiv:hep-ex/9509010

[39] **(CDF)** A. Abulencia et al., J. Phys. G34, 2457 arXiv:hep-ex/0508029

[40] **(D0)** S. Abachi et al., Phys. Rev. Lett. 75, 1456 arXiv:hep-ex/9505013

[41] **(D0)** B. Abbott et al., Phys. Rev. D61, 072001 arXiv:hep-ex/9906025

[42] **(ATLAS)** G. Aad et al., JHEP 12, 060 arXiv:1010.2130

[43] **(CMS)** V. Khachatryan et al., JHEP 01, 080 (2011), arXiv:1012.2466

[44] **(CMS)** S. Chatrchyan et al., JHEP 10, 132 (2011), arXiv:1107.4789

[45] **(PHENIX)** A. Adare et al. PHENIX Collaboration, Phys.Rev.Lett.106:062001,2011

[46] **(STAR)** M. Aggarwal et al., Phys. Rev. Lett. 106 (2011) 062002.

[47] A. Zelenski et al., Hyperfine Interactions 127, 475 (2000), 10.1023/A:1012682104479.

[48] **(PHENIX)** K. Adcox et al., NIM A499 469-479 (2003)

[49] **(STAR)** K. Adcox et al., NIM A499 624-632 (2003)

[50] **(PHOBOS)** B. Bak et al., NIM A499 437-468 (2003)

[51] **(BRAHMS)** K. Adcox et al., NIM A499 603-623 (2003)

[52] **(PHENIX)** S. Adler et al., NIM A499 560-592 (2003)

[53] **(PHENIX)** S. Adler et al., NIM A499 593-602 (2003)

[54] **(PHENIX)** M. Beaumier, F. Giordano,R. Hollis, D. Jumper, A. Meles, R. Seidl., "Run 13 W-¿Mu Analysis, Single Spin Asymmetry and cross section", the PHENIX collaboration analysis note No. 1195

[55] P. Sona, Energia Nucleare 14, 295 (1967)

[56] Y. S. Derbenev et al., Part. Accel. 8, 115 (1978)

[57] S.R. Mane, et al., J. Phys. G: Nucl. Part. Phys. 31 (2005) R151-R209

[58] I. Alekseev, et al., "RHIC Polarized Proton Manual" http://www.bnl.gov/cad/accelerator/docs/pdf/RHICPPCMan.pdf

[59] O. Jinnouchi et al., RHIC/CAD Accelerator Physics Note 171 (2004)

[60] H. Okada et al., Phys. Lett. B638, 450 (2006), nucl-ex/0502022

[61] A. Zelenski et al., Nucl. Instrum. Meth., vol. A536, pp. 248?254, 2005.

[62] A. Bazilevsky et al., Phys. Lett. B650, 325 (2007), hep-ex/0610030

[63] **(PHENIX)** K. Adcox et al., NIM A499 489-507 (2003)

[64] **(PHENIX)** M. Aizawa et al., NIM A499 508-520 (2003)

[65] **(PHENIX)** L. Aphecetche et al., NIM A499 521-536 (2003)

[66] **(PHENIX)** H. Akikawa et al., NIM A499 537-548 (2003)

[67] http://www.phenix.bnl.gov/WWW/muon/muid/muid/design-book2/muid-overview.html

[68] **(PHENIX)** Yoshinori Fukao., J. Phys: Conf. Ser. 295 012165 pp 2.

[69] C. Aidala, et. al., NIM A755 44-61 (2013)

[70] C. Aidala, et. al., NIM A755 60-61 (2013)

[71] T. Mibe, et al., "Technical Design Report on Amplifier-Discriminator board and Data Transfer board for the MuTr FEE upgrade ver.3.3" (2007)

[72] S. Adachi, et. al., Nuclear Inst. and Methods in Physics Research, A (2013), pp. 114-132

[73] A. Basye, et al., "Conceptual Design Report for a Fast Muon Trigger at PHENIX", 2007

[74] R. Towell, Nucl. Instr. Meth. A 602 (2009) 705-708

[75] **(PHENIX)** M. Allen et al., NIM A499 549-559 (2003)

[76] **(PHENIX)** C. Adler, et al., NIM A 470 (2001) 488-499

[77] E. Mathieson, "Cathode charge distributions in multiwire chambers", Nuclear Instruments and Methods in Physics Research A270 (1988) 602-603

[78] **(PHENIX)** S.S. Adler et al., NIM A499 560-592 (2003)

[79] **(PHENIX)** S.S. Adler et al., NIMA499 593-602 (2003)

[80] P. Chand et al., "A Primer Manual for the PHENIX Simulation Code PISA", http : //www.phenix.bnl.gov/phenix/WWW/simulation/primer4/seq_primer.html

[81] "RUN OVERVIEW OF THE RELATIVISTIC HEAVY ION COLLIDER", http://www.rhichome.bnl.gov/RHIC/Runs/

[82] **(PHENIX)** Bazilvsky, A. and Chiu, M. and Haggerty, J. and Karatus, K. and Kawall, D. and Kistenev, E. and Okada, K., "Central Arm W Analysis", the PHENIX collaboration analysis note No. 923,2011

[83] **(PHENIX)** Chiu, M. and Grosse-Perdekamp, M and Wolin, S., "New Ideas on Relative Luminosity Determination in Run09 500 GeV Polarized Proton Collisions", the PHENIX collaboration analysis note No. 1184,2014

[84] **(PHENIX)**Manion, A., "Method For Determining Relative Luminosity From Detection Probabilities (Run9 200 GeV)", the PHENIX collaboration analysis note No. 953,2013

[85] RHIC Spin Group, "Polarimetry-H-jet-Run13",
https : //wiki.bnl.gov/rhicspin/Polarimetry/H − jet/Run13

[86] **(PHENIX)**M. Beaumier, C. Gal, M. Kim, S. Park, R. Seidl, I. Yoon., "Run 13 Spin Database Quality Assurance", the PHENIX collaboration analysis note No. 1125,2014

[87] **(PYTHIA6)** Torbjörn Sjöstrand, et al., JHEP05 (2006) 026

[88] **(PHENIX)** Elke Aschenauer, John Lajoie, Richard Seto., "Pythia, Tune A", the PHENIX collaboration analysis note No. 862, 2009

[89] Oide, H., "Thesis",2012,
https : //www.phenix.bnl.gov/WWW/p/draft/oide/phdthesis/thesis.pdf

[90] **(PHENIX)** Kempel, T and Seidl, R and Meredith, B., "Run 9 evaluation of absorber effects on Hadrons, Muons, and $J/\psi$s in the PHENIX Muon Arms and its implications on the $W \to \mu$ analysis", the PHENIX collaboration analysis note No. 899, 69 (2010)

[91] **(PHENIX)** Seidl, R and Oide, H and Hollis, R and Sarsour, M and Seele, J and Leitgab, M and Imazu, Y and Choi, I., "Run 11 W Analysis Note", the PHENIX collaboration analysis note No. 1024, 295 (2012)

[92] M. Thomson., "Professor Mark Thomson Lecture Courses: Chi-squared and likelihood fitting"
http://www.hep.phy.cam.ac.uk/ thomson/lectures/lectures.html

[93] "PEPSI"

https://wiki.bnl.gov/eic/index.php/PEPSI

[94] L. Adamczyk, et al., Phys. Rev. Lett. 113, 072301 (2014)

[95] **(UA1)** UA1 Collaboration (C. Albajar et al.), CERN-EP-89-85, Jul 1989. 30pp., Nucl. Phys. B335:261,1990

[96] **(ISR)** Alper et al. Nucl. Phys. B100, 237 (1975)

[97] **(Garfield)** Rob Veenhof, Garfield - simulation of gaseous detectors, http://garfield.web.cern.ch/garfield/

[98] **(PHENIX)** K.Okada, et al., "Central Arm W Analysis", the PHENIX collaboration analysis note No. 923

[99] **(PHENIX)** A.Bazilevsky, "$\pi^0$ cross section analysis at mid-rapidity from pp Run9 $\sqrt{s} = 500$ GeV", the PHENIX collaboration analysis note No. 884

[100] **(CTEQ6.6)** P. M. Nadolsky, H.-L. Lai, Q.-H. Cao, J. Huston, J. Pumplin, D. Stump, W.-K. Tung, C.-P. Yuan, Phys.Rev.D78:013004,2008, hep-ph/0802.0007

[101] **(CTEQ6M)** J. Pumplin, D.R. Stump, J. Huston, H.L. Lai, P. Nadolsky, W.K. Tung, arXiv:hep-ph/0201195

[102] **(DSS)** D. de Florian, R. Sassot and M. Stratmann, Phys. Rev. D75 (2007) 114010 hep-ph/0703242; Phys. Rev. D76 (2007) 074033 0707.1506;

[103] W. Verkerke and D. Kirby, "The RooFit toolkit for data modeling", in proceedings of Statistical Problems in Particle Physics, Astrophysics and Cosmology

[104] MINUIT, Function Minimization and Error Analysis, http://lcgapp.cern.ch/ project/cls/work-packages/mathlibs/minuit/home.html/

[105] **(FEWZ)** K. Melnikov and F. Petriello, Phys. Rev. D74, 114017 (2006), hep-ph/0609070.

[106] P.M. Nadolsky and C.-P. Yuan, Nucl.Phys.B666:3-30,2003, hep-ph/0304001

[107] H. L. Lai et al., Eur.Phys.J.C12:375-392,2000

[108] M.Glück, E. Reya, M. Stratmann, and W. Vogelsang, Phys. Rev. D 63, 094005 (2001)

[109] D. de Florian, G. A. Navarro, and R. Sassot, Phys. Rev. D 71, 094018 (2005)

[110] **(MSTW08)** A.D. Martin, et al., Eur.Phys.J.C63:189-285,2009